2019

COMPOSITIONAL ANALYSIS OF CERIUM AND CESIUM IN RAPID SETTING CEMENT AS AN IMMOBILIZATION AGENT FOR NUCLEAR WASTE

RIYADH M. MOTNY
Virginia Commonwealth University

www.manaraa.com

COPYRIGHT PAGE

COMPOSITIONAL ANALYSIS OF CERIUM AND CESIUM IN RAPID SETTING CEMENT AS AN IMMOBILIZATION AGENT FOR NUCLEAR WASTE

A Dissertation Submitted in Partial Fulfillment of the Requirements for the Degree of Doctor of Philosophy at Virginia Commonwealth University

By

Riyadh Monowr Motny

M.Sc. Mechanical Engineering, University of Tikrit, Sallahaldin, Iraq, 2006

Major Professor: Supathorn Phongikaroon, Ph.D.

Virginia Commonwealth University

Richmond, Virginia

May, 2019

Acknowledgments

First of all and above, I would like to thank and praise my God (Allah) Almighty for providing me the power and knowledge to conduct and accomplish this research project satisfactorily. This dissertation would never have been possible without his blessings. I would like to express my very deep appreciation and sincere thanks to my advisor, Dr. Supathorn (Supy) Phongikaroon, for his valuable support, guidance, patience, and encouragement during these past five years. Without his valuable comments, his expertise, his insight and the effort and time he dedicated to helping me, this dissertation would not have reached its current form. He also supported me to attend various nuclear engineering programs and conferences. I would never forget his generosity and genuine care and kindness with me like a member of his family. No words can adequately express my sincere gratitude to my wonderful wife, Salma, for continuously and patiently supporting me through all my study and for my lovely children (Safa and Wisam) whom the Ph.D. study took me away from them. I would also like to acknowledge my committee members, Drs. Dmitry Pestov, Reza Mohammadi, Jessika V. Rojas, and Prof. Milos Manic for their insightful comments and invaluable encouragement to achieve this thesis. I would like to thank all my fellow graduate students Ammon Williams, Samaneh Rakhshan Pouri, Michael Woods, Hunter Andrews, and Dimitris Killinger for their friendship and support as well. Most importantly, I want to express the gratefulness to the Higher Committee of Educational Development (HCED) in Iraq for making this research possible through their financial support and cooperation that gave me the chance to study in the United States. Last but not least, I would like to send my gratefulness and love to my family: my wonderful dad and mom, brothers, and sisters.

Contents

iv

List of Figures

x

xi

List of Tables

List of Abbreviations and Symbols

Abbreviations and Acronyms

Name	Description
ANNs	Artificial neural net-works
ASW	Artificial seawater
BFS	Blast furnace slag
CFL	Cumulative fraction leach
DFA	Discriminant functional analysis
DIW	Deionized water
DM	Diffusion model
EDX	Energy-dispersive X-ray spectroscopy
EW	Exempt waste
FDNPP	Fukushima Daiichi nuclear power Plant
FRDM	First-order reaction/diffusion model
FRM	First-order reaction model
FST	Final setting times
HLW	High level waste
IAEA	International Atomic Energy Agency
ICP	Inductively-coupled plasma
ICP-MS	Inductively coupled plasma-mass spectrometry

ILR	Incremental leach rate
ILW	Intermediate level waste
INAA	Neutron activation analysis
LDA	Linear discriminant analysis
LIBS	Laser-induced breakdown spectroscopy
LILW	Low and intermediate level waste
LILW-LL	Low and intermediate level waste- long lived waste
LILW-SL	Low and intermediate level waste-short lived waste
LLW	Low-level waste
LOD	Limit of detection
LOOCV	Leave one out cross validation
LV	Latent variables
MVA	Multivariate analysis
Nd:YAG	Neodymium-doped yttrium aluminum garnet; $Nd:Y_3Al_5O_{12}$
Nd:YALO	Neodymium-doped yttrium orthoaluminate
NIST	National Institute of Standards and Technology
NRC	The U.S. Nuclear Regulatory Commission
OPC	Ordinary Portland cement
PCA	Principal component analysis
PFA	Pulverized fuel ash
PLS	Partial least squares
RI	Relative intensity

RMSE	Root mean squared error
RMSECV	Root mean square error cross validation
RSC	Rapid setting cement
S/B	Signal-to-background ratio
S/N	Signal-to-noise ratio
S/S	Stabilization/solidification
SCMs	Supplementary cementitious materials
SEM	Scanning electron microscopy
SVD	Singular value decomposition
W/C	Water/ cement ratio
XRD	X-ray diffraction
XRF	Fluorescence analysis

Symbols

Name	Description	Unit
A_o	Initial radioactivity present in the sample	μg
$\sum A_n$	Cumulative radioactivity leached during leaching interval n	μg
B	PLS regression coefficient matrix	
b_0	Y-intercept of the linear regression line	
b_1	Slope of the linear regression line	
C_1	Weight of the covariance with respect to Y	
D_e	Effective diffusivity coefficient	cm^2/s
d_s	Diameter of the cylinder sample	cm
E	Matrix of residual of X	
F	Matrix of residual of Y	
G	Dimensionless time factor	
J(t)	Flux of diffusing radionuclide	$mol\ cm^{-2}\ s^{-1}$
k	Rate constant	1/s
M	Initial amount of soluble radionuclides	mg/g
M_d	Dry mass of the sample	g
M_s	Submerged mass of the sample	g
M_w	Wet mass of the sample	g
m	Number of spectral data points (PLS)	

n	Number of samples	
n_r	Number of repetitions	
n_s	Number of cross validation points used	
P	Loading or weight of X (PLS)	
P_A	Apparent porosity of the sample	%
Q	loading matrices of X (PLS)	
R_1	PLS covariance	
S	Total surface area of the sample	cm^2
$S_{y/x}$	Standard deviation in the y-direction	
T	X latent variable matrix (PLS)	
T_m	Leaching time representing the mean time of the interval	s
t	Total elapsed time from leaching initiation	s
$t_{95\%}$	Students t value at 95%	
$\sum t_n$	Cumulative period of leaching	day
U	Y latent variable matrix (PLS)	
u_1	First pseudo latent variable	
V	Volume of the sample	cm^3
V_T	Total volume of the sample	cm^3
W_1	Weight of the covariance with respect to X	
X	Independent variables (spectra) in PLS	
x	Concentration	wt%
$x_{i, LIBS}$	Concentration of the data point that was independently predicted	wt%

$x_{i, XRF}$	Actual concentration for that point obtained from XRF	wt%
$\bar{x}$	Mean of the concentration values	wt%
Y	Predicted concentration (PLS)	
y	Spectral response	a.u.
y_{CI}	Regression confidence interval	
$\bar{y}$	Mean of spectral response	a.u.
$\hat{y}_i$	Predicted spectral response from regression	

Greek

Name	Description	Unit
β	Constant	$1\ cm^2/s$
Δ_1	Matrix of values corresponding to the covariance	
ρ_B	Bulk density of the sample	g/cm^3
ρ_w	Density of water	g/cm^3
σ_b	Standard deviation of the blank sample	

Abstract

COMPOSITIONAL ANALYSIS OF CERIUM AND CESIUM IN RAPID SETTING CEMENT AS AN IMMOBILIZATION AGENT FOR NUCLEAR WASTE

By Riyadh Monowr Motny, Ph.D.

A dissertation submitted in partial fulfillment of the requirements for the degree of Doctor of Philosophy at Virginia Commonwealth University.

Virginia Commonwealth University, 2019.

Major Professor: Supathorn Phongikaroon, Associate Professor of Mechanical and Nuclear Engineering Department.

A feasibility of rapid setting cement (RSC) as an agent of immobilization for certain elements such as fission products or radioactive materials was explored. Cerium (Ce) and cesium (Cs) have been selected as a surrogate for U and/or Pu and fission products, respectively, in this study in three phases. In Phase I, RSC was evaluated for physical properties (e.g., porosity, density, pH values, etc.) using two groups methods—the cement powder at different concentrations of Ce (2 – 10 wt%) with deionized water (DIW) and artificial seawater (ASW). The results showed that the final setting time and compressive strength of RSC in DIW and ASW solutions decreased as Ce content increased. The X-ray diffraction patterns revealed two newly identified phases, namely $CeAl_{11}O_{18}$ and $Ce_{4.667}(SiO_4)_3O$. The morphology of matrix samples showed that the existence of Ce distributed on the pore wall or clustered with Si, Al, Mg, K, P, Fe, and O.

In Phase II, laser-induced breakdown spectroscopy (LIBS) technique together with univariate and multivariate analyses of the principal component analysis (PCA) and partial least squares (PLS) were applied to detect the surrogate elements (Ce (0.5 – 8 wt%) and Cs (0.5 – 4 wt%)) for nuclear materials captured in ceramic materials. The best calibration curves for Ce and Cs in samples were created using the peak areas of the Ce 571.8 nm line and Cs 697.1 nm line, respectively. PCA method was applied to explain 85.5 % for Ce-cement samples in DIW and 91.4 % for those in ASW. Samples with Cs indicated similar PCA trends. The PLS calibration curves for Ce and Cs samples in DIW and those in ASW were made using seven and eight latent variables (LV).

In Phase III, the leaching behaviors of Ce and Cs mixture with DIW and ASW under both dynamic and static leach conditions were investigated according to the ANSI/ANS 16.1-2003 standard method. Elemental compositions were analyzed using an inductively coupled plasma-mass spectrometry (ICP-MS) for the leaching periods of 2, 7, and 24 hours and 2, 3, 4, 5, 14, 28, 43, and 90 days. Three mathematical models—first-order reaction model (FRM), diffusion model (DM), and first-order reaction/diffusion model (FRDM)—were fitted to assess the leaching parameters of immobilized radionuclides in the RSC matrix. Results showed that leaching of ^{140}Ce and ^{133}Cs from RSC matrices with (DIW and ASW) under both dynamic and static leach conditions was less than 20%. It was found that the leaching phenomena of ^{140}Ce and ^{133}Cs was dominantly controlled by FRM with a weak effect of DM, which was best fitted by FRDM. Here, the average leachability index (L) for ^{140}Ce and ^{133}Cs, are greater than the recommended minimum of 6 that allowed their acceptance for disposal. These studies indicated a good feasibility of using RSC with DIW and ASW for immobilizing non-radioactive Ce and Cs and RSC had a potential for applying to actual radioactive materials.

Chapter 1

Introduction

1.1 Motivation

Nuclear power is considered one of most important sources of electricity production in the United States because it can deliver clean and reliable energy. However, nuclear power plant program continues to encounter serious difficulties in its development due to the quantity of radioactive wastes produced, in which there is no satisfying solution to date [1]. Furthermore, the fission products and actinide by-products could be liberated into the environment from nuclear reactors cores due to nuclear accidents (e.g., the resulting concerns from Fukushima accident) [2]. However, these radioactive materials have to be handled in techniques that protect public health and prevent environmental pollution [3]. Stabilization/solidification (S/S) methods are the most common practice to minimize the possibility of migration or dispersion of contaminants including radionuclides. These S/S technologies include the mixing of a waste with a binder such as cementitious materials [4-6]. Several studies have been done on the ability of cementitious materials to immobilize, both physically and chemically, radioactive materials within their structures [4-7]. Of all the cementitious materials, Portland cement is the most widely used for immobilization radioactive materials due to its availability and low cost [6]. On the other hand, there are other types of cementitious materials that have received less attention into exploring their feasibility as agents of immobilization; this is known as a rapid setting cement (RSC). Compared with Portland cement, RSC has the following valuable properties: faster setting time, having a broad range of ambient temperature for curing, potable and non-potable water can be used for

1

preparing mixtures, good encapsulation characteristics, high early compressive strength, low permeability, and good acid resistance [8-12]. In addition, RSC can be utilized as an emergency immobilization technique on the field, owing to its rapid setting nature, to reduce release of radioactive materials into the environment even for potential nuclear accidents. Despite successful studies on RSC, there is limited information on its application towards nuclear power industries. This concern becomes the main motivation of this dissertation.

1.2   Purpose

The main goal of this dissertation is to perform a technical assessment of RSC, as an alternative agent for immobilization of certain elements such as fission products or radioactive materials, by (1) evaluating the setting time and mechanical properties, (2) developing a detection technique for radioactive elements captured in ceramic materials, and (3) determining leachability of these elements from the cement. To develop a fundamental understanding of this alternative immobilizing system, we have explored the effect of low to high cerium (2 – 10 wt%) concentrations as a surrogate material for uranium and plutonium in cement mixtures with deionized water (DIW) and artificial seawater (ASW). It should be noted that typical concentrations of uranium chloride (UCl_3) used in the electrochemical process could be ranging up to 10 wt% [13]; and the concentration range of cerium was being studied using this general knowledge as a basis. Following this testing, a matrix of cerium (0.5 – 8 wt%) and cesium (0.5 – 4 wt%) with deionized water (DIW) and artificial seawater (ASW) in cement mixtures was analyzed to detect the surrogate elements for nuclear materials captured in ceramic materials using laser-induced breakdown spectroscopy (LIBS) technique, including univariate and multivariate analyses, such as principal component analysis (PCA) and partial least square (PLS). Finally, the leaching behaviors of Ce and Cs from the mixture of RSC with DIW and ASW under both dynamic

2

and static leach conditions were investigated. Additionally, mathematical models were applied to assess the leaching parameters of immobilized radionuclides in the RSC matrix.

1.3 Approach

Based on the aforementioned objectives, this research study was divided into three phases. In Phase I, extensive literature review on cement systems used for stabilization/solidification of nuclear waste materials reported by other researchers has been conducted to provide a summary of the information and knowledge relevant to this research. In addition, RSC properties and methods of cement testing as well as microstructure, phase composition of hardened cement paste were done for the purpose of obtaining reliable and confident results describe RSC before and after adding cerium chloride ($CeCl_3$) as a surrogate for uranium chloride (UCl_3) in this phase. To accomplish this, several tests (W/C ratio, compressive strength, and porosity) were done including X-ray fluorescence (XRF), X-ray diffraction (XRD), and scanning electron microscopy (SEM) including energy-dispersive X-ray spectroscopy (EDX) techniques to determine the crystalline phases, elemental composition, and microstructure of RSC in fresh and saline environments.

In Phase II, experiments were focused on an additional fission product (cesium chloride (CsCl)) effect on the existing experimental matrix from Phase I. Two different mediums were done at different concentrations of $CeCl_3$ (0.5 - 8 wt% Ce) and CsCl (0.5 – 4 wt% Cs) with DIW and ASW, respectively. Thus, these two groups will serve to provide a comparative analysis between the samples to determine distributions and behaviors of Ce and Cs in the cement matrix. LIBS and XRF were performed to detect Ce and Cs in the cement mixture. Univariate calibration curves and partial least squares (PLS) were conducted to develop a calibration model. Principal component analysis (PCA) and LIBS were used, in combination, as another method to detect the Ce and Cs in the cement mixture and identify unknown cement samples.

3

In Phase III, leaching experiments will be utilized to measure the cumulative fraction leach (CFL) that describes the leaching rate of radionuclides that transfer from immobilized waste matrix to the surrounding water. Leaching experiments were carried out using the method suggested by ANSI/ANS 16.1-2003. Then, measured concentrations of Ce and Cs in the leachates were analyzed using inductively coupled plasma mass spectrometry (ICP-MS). The results of these tests are used to assess the leaching parameters by fitting the experimental data to mathematical models that characterize various leaching mechanisms. Three mathematical models were considered; these are (1) first-order reaction model (FRM), (2) diffusion model (DM), and (3) first-order reaction/diffusion model (FRDM). These phases were used to explore the feasibility RSC as alternative immobilizing system for nuclear materials. Table 1.1 displays the time line to fulfill this work.

Table 1. 1 Research plan for this dissertation.

Phase	Year 1 (2015)				Year 2 (2016)				Year 3 (2017)				Year 4 (2018)				Year 5 (2019)			
	1	2	3	4	1	2	3	4	1	2	3	4	1	2	3	4	1	2	3	4
I	■	■	■	■	■	■														
II				■	■	■	■	■	■	■										
III									■	■	■	■	■	■	■	■	■			

1.4 Organization of the Dissertation

This thesis contains six chapters. Chapter 1 offers the motivation, purpose, and approach of this study. Chapter 2 contains a literature review of basic nuclear waste and the relevant cement systems that have been used for stabilization/ solidification of nuclear materials, as well as,

4

included a review of some of LIBS and Leachability studies that have been done in cementitiaa materials, together with short description of RSC used as alternative for immobilization radioactive materials. Chapter 3 presents experiments and preliminary results of Ce as a surrogate material for U in the cement mixture with DIW and ASW. Various tests and analytical techniques were applied to characterize the $CeCl_3$-RSC system, including the setting time, apparent porosity, bulk density, pH value, conductivity, compressive strength test, phase identification, and microstructure. Chapter 4 focuses on the measure of radioactive elements in the cement mixture using LIBS and XRF techniques, in which different Ce and Cs concentrations as surrogate materials were used to build numerous cement matrices with two type of water (DIW and ASW). Also, this chapter includes calculating univariate calibration curves, PCA, and PLS. In Chapter 5, the leachability of Ce and Cs immobilized in RSC has been evaluated using the ANSI/ANS 16.1 leach test method under both dynamic and static conditions. Cumulative fraction leached for Ce and Cs were determined and then fit to three mathematical models; first-order reaction model (FRM), diffusion model (DM), and first-order reaction/diffusion model (FRDM). Chapter 6 summarizes the findings of the present study. The final chapter (Chapter 7) offers the possible suggestions for the future work. Appendices contain additional materials that would support the whole body of this study.

5

Chapter 2

Literature Review

2.1 Introduction

This chapter provides a literature review related to the current studies in three phases. The first section includes background on nuclear waste. Then features of immobilization of the radioactive materials by using cementitious systems, the composition analysis and the major phases present in ordinary Portland cement (OPC), and the popular supplementary cementitious materials applied to improver properties of OPC are being introduced. The next section describes LIBS studies that have been carried out in solid mediums such as cement and glass matrix with different elements such as Cl, Ce, Pu, U, Eu, Cs, and Sr. These studies show a strong potential for utilizing LIBS in the solid matrix. Finally, the background on leaching behavior of the radioactive elements within cementitious matrices studies was given including information on how to evaluate these materials.

2.2 Background on Nuclear Waste

A nuclear (radioactive) waste can be presented from three different aspects: (1) in general, it is the radioactive waste that is generated throughout nuclear fuel production and consumption stages to produce the nuclear power, from extraction and mining to reprocessing of the used fuel and disposal, (2) from regulatory purposes viewpoint, it is a material that comprises or is contaminated with radionuclides at concentrations or activities greater than clearance levels as defined by the regulatory authority, and (3) from a physical viewpoint, it is considered radioactive even if it is with activity concentrations equal to or less than clearance levels – in spite of the fact

6

that the associated radiological hazards are seen as insignificant [5, 14, 15]. The 'clearance level' of waste is that level which poses a negligible risk to human health and the environment, thereby it can be liberated into the environment without any conditions [16].

The diversity of techniques and methods—used in the nuclear industry—leads to producing different kinds of radioactive material or radioactive waste in various physical and chemical compositions, causing various levels of risks. These materials and wastes can pose a potential hazard to the human health and the environment; so, it is important to be appropriately classified to manage them in a way that is safe for handling, storage, transportation, and disposal. There are different views considered in the classification systems such as safety perspective, the physical/chemical properties of the waste, process engineering needs or regulatory issues; however, the present globally accepted classification system is based on the activity level and half-life [17-19]. According to the International Atomic Energy Agency (IAEA), the radioactive waste is classified, depending on the radiological characteristics of wastes, into five categories which are summarized in Table 2.1.

Due to the natural disasters, such as an earthquake being accompanied by tsunami sometimes, power plants close to the ocean may be at risk from damage or destruction (for example, the Fukushima Daiichi nuclear power Plant (FDNPP) disaster) [20, 21]. This disaster as shown in Figure 2.1 has led to melt down of the reactor cores in the first days due to the fact that FDNPP eventually failed to cool the nuclear fuel. Therefore, radioactive materials were released into the environment due to hydrogen blasts. [21]. The amount of pollution caused by the spread of fission products and their decay products into the environment poses a major threat to human health and living organisms. These also have led to contamination of many different varieties of materials including soil, plants, roads, buildings, vehicles, and cleaning wastes. [22].

7

Table 2. 1 Radioactive waste classification [23].

Waste classes	Typical characteristics	Disposal Options
Exempt waste (EW)	Activity levels at or below clearance levels, which are based on an annual dose to members of the public of less than 0.01 mSv (1 mrem)	No radiological restrictions
Low and intermediate level waste (LILW)	Activity levels above clearance levels and thermal power below about 2 kW/m^3;	
Short lived waste (LILW-SL)	Restricted long lived radionuclide concentrations (limitation of long lived alpha emitting radionuclides to 4,000 Bq/g in individual waste packages and to an overall average of 400 Bq/g per waste package)	Near surface or deep underground disposal facility
Long lived waste (LILW-LL)	Long lived radionuclide concentrations exceeding limitations for short lived waste	Deep underground disposal facility
High level waste (HLW)	Thermal power above 2 kW/m^3 and long lived radionuclide concentrations exceeding limitations for short lived waste	Deep underground disposal facility
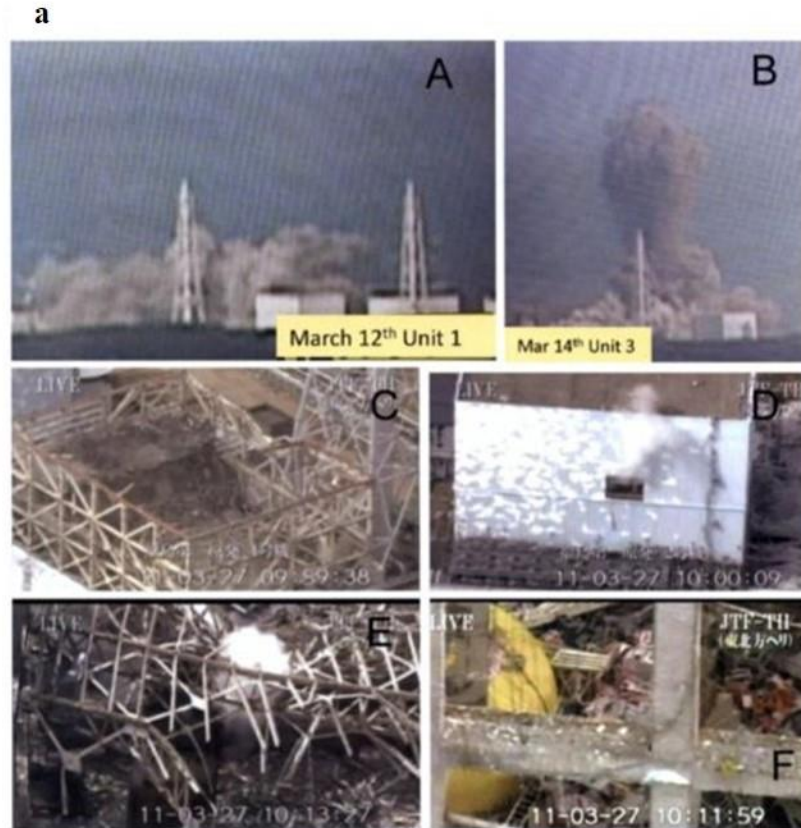
Figure 2. 1 (a) Hydrogen explosions and destruction of reactor buildings, panels (A and C) unit 1, panel D unit 2, panels (B and E) unit 3, and panel F unit 4 (b) Units 1, 2, 3, and 4 after the explosions [24].

Waste immobilization techniques have been used to prevent a release of radionuclides into the environment, in which the radioactivity will be confined and retained in the waste [25]. Immobilization is defined according to IAEA as the conversion of a waste into a waste form, by solidification, embedding, or encapsulation. These wastes will become physically and chemically stable, thereby offering safe handle, transport, and disposal of waste [14]. Various matrices have been utilized in nuclear waste immobilization such as cement, cement-based materials, bitumen, glass, ceramics and metals. Cementitious materials are one of the most desirable materials used in waste management systems on a massive scale as an immobilization matrix. This is due to their favorable physical and chemical properties which make them suitable for the encapsulation of radioactive and toxic wastes [1, 26]. Figure 2.2 shows the embedment of used nuclear fuel and scrap material in cement [15, 27].
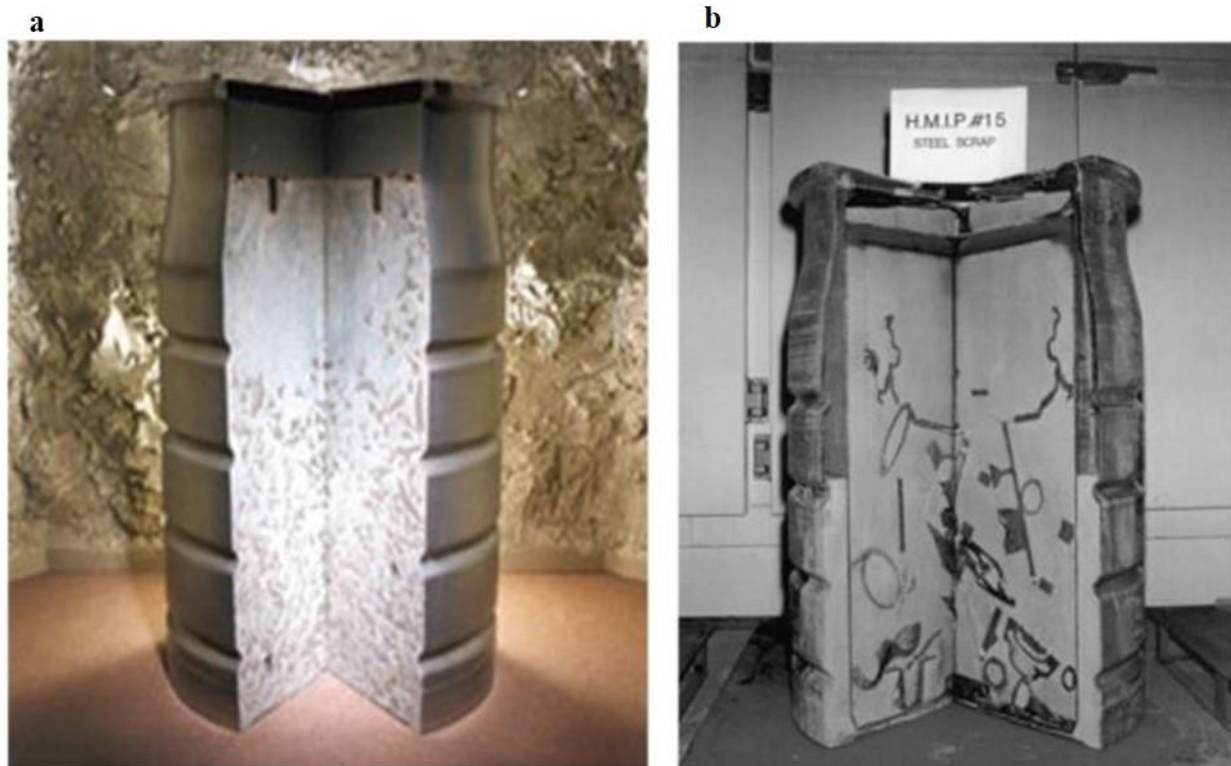
Figure 2. 2 (a) Cementation of used nuclear fuel cladding in 500L stainless steel drum [15], (b) Metallic scrap material embedded in cement (UK) [27].

2.3 Hydraulic Cement Systems for Stabilization/ Solidification

Basically, a cement is a powdery substance, one of the world's most familiar and popular building materials, which converts into a stone-like state after mixing with water at ambient temperature as a consequence of physicochemical processes. Cementitious materials are one of the most widely used material for stabilization/ solidification (S/S) of hazardous waste, low-level radioactive waste (LLW), intermediate level waste (ILW), and mixed wastes, as well as remediation of contaminated sites duo to their advantages [6]. There are several features of immobilization of the radioactive materials by using cementitious systems, including [4, 28]:

- Cementitious materials are low cost and widely available.
- Cement matrix supports the immobilization of the radionuclides duo to:
    (a) It is acting as a diffusion barrier and providing sorption and reaction sites.
    (b) The high pH of the cement leads to low the solubility of the radionuclides.
- The waste form is relatively non-toxic, non-combustible, reasonable compressive strength, flexible (can be modified), and having good thermal, chemical and physical stability.
- It is appropriate for most of the different forms of radioactive waste such as sludge, liquors, emulsified organic liquids, and dry solids.
- The resulting solid products are sufficiently radiation resistant.

There are many types of cement used for immobilization of the radioactive materials for safe storage and disposal. The most commonly used cement types are conventional cementitious materials such as OPC and the conventional cement systems based on partial replacements of OPC with pulverized fuel ash (PFA), iron blast furnace slag, silica fume, and natural pozzolans.

11

Nowadays, the cement systems used are such as high alumina, geopolymers, calcium sulfoaluminate, and MgO based or phosphate (acidic) cements [26].

2.3.1 Ordinary Portland cement (OPC)

OPC is the most commonly applied cement for construction use and immobilizing both liquid and solid radioactive wastes due to its commercial availability at a low cost. OPC is basically a mixture of pulverizing clinker with the addition of 3–5% calcium sulfate (gypsum — $CaSO_4.2H_2O$). The most traditional raw materials used for cement clinker production are limestone and clay where they will be burned at high temperatures up to about 1450 °C. The chemical composition of cement clinker is comprised of four main minerals, as listed in Table 2.2 [29].

Table 2. 2 Major phases present in cement clinker [29].

Name	Abbreviation	Compound
Alite	C_3S	Tricalcium silicate (Ca_3SiO_5)
Belite	C_2S	Dicalcium silicate (Ca_2SiO_4)
Aluminate phase	C_3A	Tricalcium aluminate ($Ca_3Al_2O_6$)
Ferrite phase	C_4AF	Tetracalcium aluminoferrite ($Ca_4Al_2Fe_2O_{10}$)

Generally, there are five common types of Portland cement, designated in the ASTM C-150 standard, manufactured by varying the ratio of their minerals and finenesses. The reason for this modification is to meet different physical and chemical requirements for particular applications. The five basic types of OPC with their different advantages are listed in Table 2.3.

Table 2. 3 Types of OPC and their Characteristics and uses [30].

Type of Portland Cement	Characteristics and Uses	Mineral Composition (wt %)			
		C_3S	C_2S	C_3A	C_4AF
I (Normal)	This type is normal and used for a general purpose and also often in S/S systems.	50	24	11	8
II (Moderate Sulfate Resistance)	Type II is utilized where it is necessary to protect against moderate sulfate attack such as when concrete is in direct contact with soils or water containing sulfate ions. Also, it is used in S/S applications where volatile organics are involved because this cement generates heat at a slower rate than Type I and thus may minimize the liberation of volatile organic species.	42	33	5	13
III (High Early Strength)	The early strength of Type III is higher than Type I or II. It has the similar chemical and physical properties to Type I except that it is ground finer. This cement is used in a case that high strength concrete is required in a short time generally one week or less.	60	13	9	8
IV (Low Heat of Hydration)	This cement is used in cases that need to minimize the heat generated as in large concrete structures such as dams and large foundations where an exaggerated heat rise could cause cracking because of volume change.	26	50	5	12
V (High Sulfate Resistance)	This cement has a higher resistant to sulfate attack than Type II because it has lower tricalcium aluminate content (5% maximum) than former. It is used in S/S systems that contain or be in direct contact with soils, waste, or groundwater that have a high sulfate content.	40	40	4	9

The knowledge of the mechanism of cement hydration is quite important, especially for work relating to radioactive waste immobilization. However, it is still not sufficiently understood, because of its complex physical and chemical reactions [31-33]. The hydration of cement is a series of chemical reactions that take place when water is added to the anhydrous cement or one of its phases. Therefore, the reaction between the two phases (C_3S and C_2S) in the cement with water

13

produces two new compounds – calcium silicate hydrate gel (C-S-H gel) and calcium hydroxide $Ca(OH)_2$. While the hydration of the phase (C_3A) in the presence of calcium sulfate forms calcium trisulfoaluminate hydrate ($3CaO \cdot Al_2O_3 \cdot 3CaSO_4 \cdot 32H_2O$ - AFt or ettringite) within 3 minutes and then turns partially or completely into calcium monosulfoaluminate hydrate ($3CaO \cdot Al_2O_3 \cdot CaSO_4 \cdot 12H_2O$ — AFm or monosulfate) depending on the ratio of calcium sulfate to C_3A [34]. However, in the absence of calcium sulfate, the reaction between C_3A with water and calcium hydroxide produces tetracalcium aluminate hydrate ($3CaO \cdot Al_2O_3 \cdot Ca(OH)_2 \cdot 12H_2O$). Eventually, C₄AF phase hydrates to produce calcium aluminoferrite hydrates ($6CaO \cdot Al_2O_3 \cdot Fe_2O_3 \cdot 12H_2O$). The cement hydration reactions are can be written as follows [6]:

$$2(3CaO \cdot SiO_2) + 6H_2O \rightarrow 3CaO \cdot 2SiO_2 \cdot 3H_2O + 3Ca(OH)_2 \tag{2.1}$$

$$2(2CaO \cdot SiO_2) + 4H_2O \rightarrow 3CaO \cdot 2SiO_2 \cdot 3H_2O + Ca(OH)_2 \tag{2.2}$$

$$3CaO \cdot Al_2O_3 + 26H_2O + 3(CaSO_4 \cdot 2H_2O) \rightarrow 3CaO \cdot Al_2O_3 \cdot 3CaSO_4 \cdot 32H_2O \tag{2.3}$$

$$2(3CaO \cdot Al_2O_3) + 4H_2O + 3CaO \cdot Al_2O_3 \cdot 3CaSO_4 \cdot 32H_2O \rightarrow \tag{2.4}$$

$$3(3CaO \cdot Al_2O_3 \cdot CaSO_4 \cdot 12H_2O)$$

$$3CaO \cdot Al_2O_3 + 12H_2O + Ca(OH)_2 \rightarrow 3CaO \cdot Al_2O_3 \cdot Ca(OH)_2 \cdot 12H_2O \tag{2.5}$$

$$4CaO \cdot Al_2O_3 \cdot Fe_2O_3 + 10H_2O + 2Ca(OH)_2 \rightarrow 6CaO \cdot Al_2O_3 \cdot Fe_2O_3 \cdot 12H_2O \tag{2.6}$$
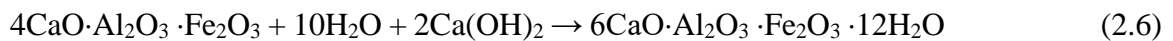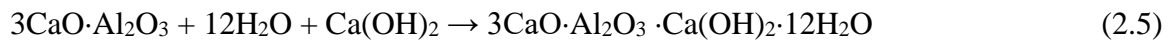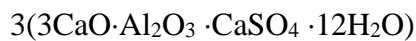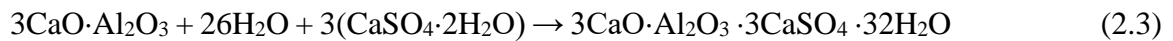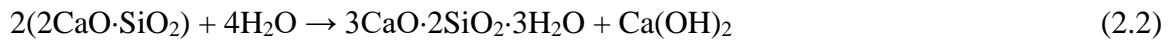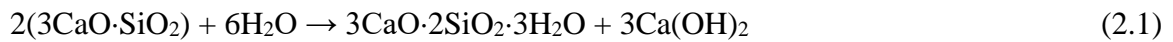
2.3.2 Blast Furnace Slag (BFS)

There exists an opportunity to improve the mechanical and durability properties of cements by mixing with other inorganic materials, namely supplementary cementitious materials (SCMs). These materials such as fly ash, slag and silica fume are overall byproducts from other processes or natural materials [35]. Blast furnace slag (BFS) is most important supplementary cementitious materials. BFS is a nonmetallic byproduct that produced from a blast furnace which is used to produce iron. It is produced from the fusion of iron ore, coke, and a flux of either limestone or

14

dolomite, together in the blast furnace [36]. It is then quickly quenched in water to form a glassy, granular product that is then dried and grounded into a fine powder. The slag consists mainly of lime, silica, and alumina that are same oxides that is present in the Portland cement but in varying proportions [37]. The fine granulated of BFS is used with partial replacement range between 20% – 40% by weight of the ordinary Portland cement to form blast furnace slag cement [38]; however, a coarser BFS is also used in the waste immobilization to decrease reactivity and lower the heat content [36]. This cement will provide a necessary performance in terms of much lower heat of hydration, high mechanical strength at later ages, high resistance to sulfate and chloride ion penetration, controllable setting rate, and chemical (including redox) binding of key radionuclides [36,39, 40]. These materials could be favorable to use in cases that the internal cracking resistance is necessary (for example, when toxic or radioactive materials are immobilized by containment within the larger cement structures). The chemical reaction between BFS is slow at room temperature. However, the rate of reaction could be enhanced by adding calcium hydroxide, gypsum ($CaSO_4$) and alkali activators such as $Ca(OH)_2$ or $NaOH$ [41].

2.3.3 Pulverized fuel ash (PFA)

Pulverized flue ash (PFA) or commonly known as 'fly ash' is a very fine dark grey ash produced from the burning pulverized coal used as fuel in electricity power stations. It is a heterogeneous fine powder with spherical glassy particles comprising mainly of SiO_2, Al_2O_3, Fe_2O_3, and CaO [42]. According to ASTM C618 [43], there are two classes of PFA; both classes F and C are based on the proportion of the ($SiO_2+Al_2O_3+Fe_2O_3$). Therefore, PFA is Type F if the ($SiO_2+Al_2O_3+Fe_2O_3$) greater than 70% while it is Type C if the total of these compounds is more than 50% or less than 70%. PFA contains of 5% - 50% of crystalline compounds and include

15

quartz, mullite, hematite, spinel, magnetite, melilite, gehlenite, kalsilite, calcium sulphate, and alkali sulfate [6]. The chemical analysis [44] for PFA is shown in Table 2.4. To enhance physical properties, reduce costs, and save energy, PFA can be used as a partial replacement material of the ordinary Portland cement. This cement have been used extensively for waste stabilization because the reaction between PFA and a cement mixture significantly reduces the permeability of the concrete by filling of the pore volume during the hydration reaction [4]. Charles McIsaac [45] investigated leach tests at the Idaho National Engineering Laboratory (currently known as Idaho National Laboratory) for both Portland Type I cement and Portland PFA cement that used to immobilize the ion-exchange resin wastes loaded with radionuclides, transition metals, and organic chelating agents. The measurement of the leachability of solidified waste matrices were carried out based on the ANSI/ANS-16.1-2003 standard using deionized water at 23°C. The results showed that Portland PFA waste forms presented lower leachability than Portland cement waste forms. Results from McIsaac's study showed that there was a reduction in permeability of waste forms as PFA contents being added into Portland Type I cement.

Table 2. 4 Typical content of Pulverized Fuel Ash [44].

Component	SiO_2	Al_2O_3	Fe_2O_3	CaO	MgO	K_2O	SO_3	C
Percentage	51.0	25.6	9.6	1.7	1.6	3.8	0.7	2.8

2.4 Laser Induced Breakdown Spectroscopy (LIBS) for Elemental Analysis

LIBS is an emission spectroscopic technique in which a laser is used to create a plasma on the desired sample. The plasma will emit light at characteristic wavelengths of the elements within the sample, in addition to background light emission. This light is directed towards a spectrometer which will determine the intensities of the light at each wavelength, and will output a spectrum. The peaks from this spectrum can be used to determine the composition of the sample [46]. LIBS

16

has been widely used determining elemental compositions of different samples such as solids, liquids, and gases [47]. LIBS has significant advantages compared with other elemental composition techniques. LIBS can provide a rapid analysis with minimal sample preparation, almost near real-time measurements, an environmentally friendly technique, and significantly reduces the risk of direct personnel exposure and liquid waste generation [48, 49]. LIBS has been widely applied across several areas such as the steel industry, the analysis of radioactive materials, elemental identification, pharmaceutical and some other fields [50].

Labutin et al. [51] made a systematic study for determining chloride (Cl) in concrete under an air medium by using double-pulse LIBS with an overlapping synthesis of second harmonics of radiation from Nd:YAG[1] and Nd:YALO[2] lasers (532 nm + 540 nm). A total of 6 samples of Portland cement M500 with GOST 10178 were prepared by mixing with the two solutions of $SrCl_2$ and DIW (10.3346 and 29.0659 g/L). The analysis was achieved on Cl I 837.60 nm which is the strong Cl line in the spectra and Mg 279.08 nm as an internal standard. The study concluded that the optimal temporal conditions of double-pulse LIBS for measure of Cl contents in cement samples were 4.0 and 0.5 μs, respectively. The results showed that the detection limit of Cl in the concrete samples was 50 ppm which is less than the threshold of 250–400 ppm.

Another study by Gondal et al. [52] has been done to determine the elemental composition and the Cl content in three different types of cements (type I, type V, and type SF) using LIBS. The LIBS results were cross-validated by the standard inductively-coupled plasma (ICP) technique. Their LIBS system was composed of a Nd:YAG Laser, an Ocean Optics 2000[+] spectrometer, a sample chamber, and OOILIBS software, as shown in Figure 2.3. The LIBS system parameters were optimized to accomplish a high-sensitivity LIBS system essential to identify trace

---

[1] Nd:YAG (neodymium-doped ytrrium aluminum garnet; Nd:$Y_3Al_5O_{12}$)
[2] Nd:YALO (neodymium-doped yttrium orthoaluminate)

quantities of elements in cement samples and to obtain the lower limit of detection. The optimal laser pulse energy and time delay of LIBS analysis used in this study were 40 mJ and 5.0 μs, respectively. The results of both LIBS and ICP were in good agreement. Additionally, the detection limit for the Cl content in the cement samples were 12 ppm. The team suggested that this work could be further developed into a mobile monitoring system of cement and building materials.
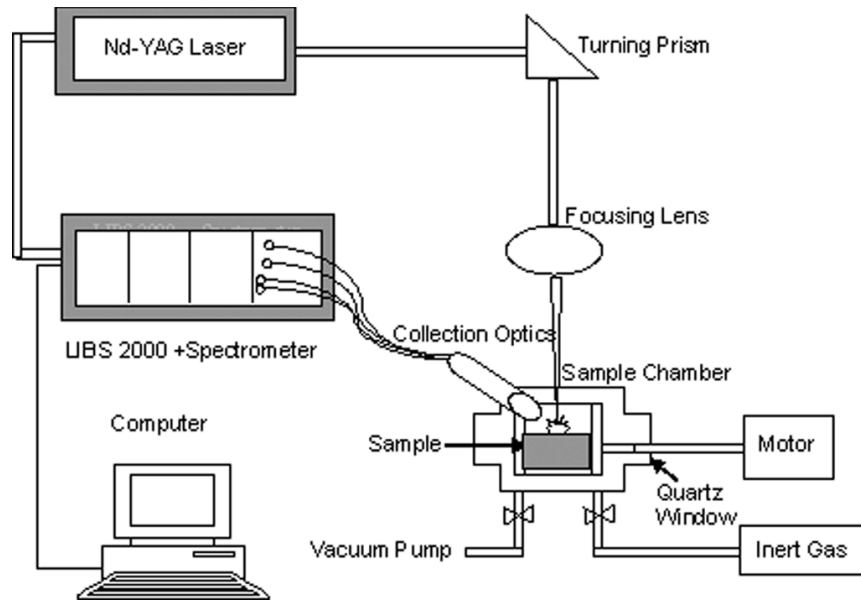
Figure 2. 3 Schematic diagram of the experimental setup applied for the analysis of cement samples [52].

Zheng et al. [53] used LIBS to measure the composition of plutonium (Pu) immobilized in the glass frit. Cerium oxide (CeO_2) was used as a surrogate material for Pu. Two different batches were utilized to prepare 5 samples with different CeO_2 concentrations from 40% to 60%. These samples were provided for analysis in both pellet and powder forms. Results indicated the detection limit of Ce in the batch pellet and powder were 0.048 wt% and 0.102 wt%, respectively.

Jung and co-workers [54] reported quantitative analysis of U and Eu—as a surrogate for fission products embedded into a glass matrix—to elucidate the feasibility of LIBS in the detection of these elements. Two sets of tests were carried out to build the calibration curves. In the first set,

18

U at the concentration of 500–50,000 ppm was mixed with glass samples. The spectrum was obtained using LIBS at laser energy 8.3 mJ, gate delay of 1 μs, and the gate width of 5 μs. While, in the second set, Eu at the concentration of 10–600 ppm with U at a constant concentration of 10,000 ppm were mixed with glass samples. The spectrum was provided at same LIBS conditions except the gate delay was 3 μs. The result indicates that LOD for U was 150 ppm using U (I) 358.488 nm line, while for Eu was 4.2 ppm using Eu (I) 459.403 nm line.

Tripathi and colleagues [55] have used LIBS for analysis of Ce oxide as a surrogate for Pu oxide in different glass batch mixtures. Both univariate calibration and multivariate analysis were applied to analyze LIBS data. Partial least square (PLS) and principal component regression (PCR) results have compared to the univariate calibration method. LIBS spectra were collected from a total of 18 different glass samples with various CeO_2 concentrations were prepared and pressed into a pellet. The optimal conditions for LIBS were laser energy at 50 mJ, gate delay of 3 μs, and the gate width of 5 μs. This research found that the coefficient of determination was improved from 0.87 to 0.97 for Ce compared to univariate calibration method.

A different kind of study was carried out by Martin et al. [49] to determine the limit of detection (LOD) of fission products (Cs and Sr), as well as Ce as a surrogate for Pu using LIBS analysis. Herein, two matrices ($CaCO_3$ and graphite material) mixed with different concentration of (Sr, Ce, and Cs) have been used to prepare pellet samples. LIBS spectra were collected under optimal LIBS conditions, laser pulse energy of 50 mJ, the temporal laser beam width is 3~5 n secs, and repetition rates from 1 to 10 Hz. Univariate calibration method and chemometric methods PCA and PLS were employed for analysis. This study concluded that the type of matrix has no effect on Sr detection. On the other hand, Ce LOD in graphite was lower than in $CaCO_3$ matrix. For Cs,

its LOD in graphite matrix was from 10,000 to 600 ppm. LIBS spectra for Ce in graphite matrix with PCA and PLS analysis were shown in Figure 2.4.
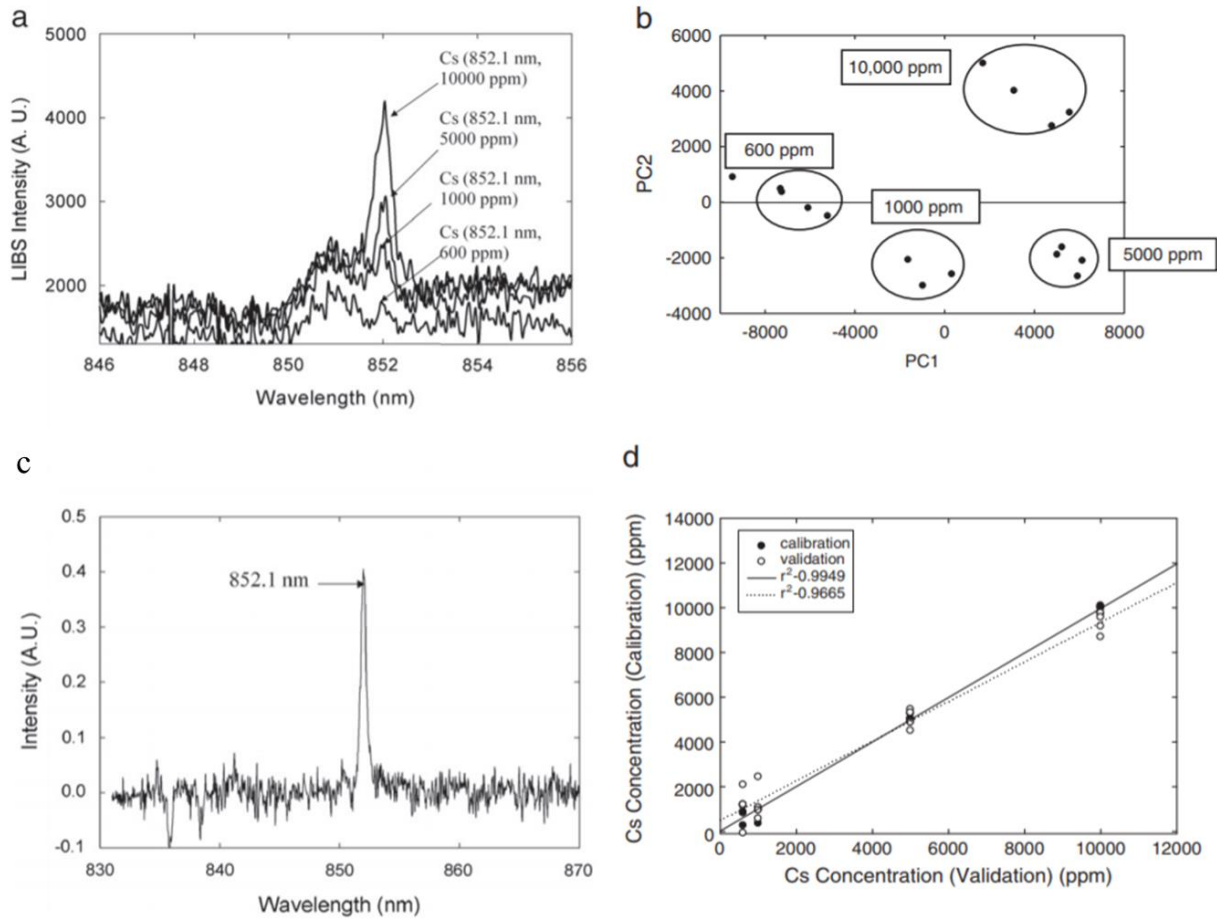
Figure 2. 4 (a) LIBS spectra for Ce 852.1 nm line; (b) PCA result; (c) Regression coefficients for projection to latent structures models predicting Cs content in graphite matrix; and (d) PLS results show the correlation between measured and predicted Cs content [49].

2.5 Leachability of Radioactive Materials from Cement Matrices

Radioactive wastes have been incorporated into different solidifying agents in order to prevent or minimize a release or the migration of radionuclides into the environment during transport and disposal, thus protecting mankind and living organisms from the risk of pollution. However, radioactive waste matrices would be in contact with groundwater when buried in repositories and that would lead to release these materials by the leaching mechanism. Therefore,

20

leach tests have been used in order to evaluate radioactive waste forms selected if they have complied with the regulatory requirements.

Laili and co-workers [56] have studied the leaching behavior of ^{134}Cs from cement mixed with different biochar concentrations (5, 11, and 18 wt%). The leach experiment has been done according to the ANSI/ANS 16.1-2003 method. The leachate solution was replaced after the leaching periods of 2 hours, 7 hours, 24 hours, 14 days, 28 days, 43 days and 90 days. Then, all Cs contents in leachate solution were measured using gamma spectrometry. This study found that an addition of biochar to the cement matrix would result in an increase in compressive strength and a decrease in the leachability of Cs. In addition, the leachability index of Cs from each cement sample was higher than the recommended minimum value of 6 by the U.S. Nuclear Regulatory Commission (NRC) Standard.

Another research by I. Plecas [57] has evaluated the leaching behavior of ^{60}Co from Portland cement. Here, a method recommended by the IAEA has been used for the leach test. A total of four samples of waste cement composition was prepared. Three factors were calculated retardation factors (K_F), coefficients of distribution (k_d), and leach coefficients D_e using mathematical model for analyzing the release of radionuclides. The result indicates that K_F, k_d, and D_e for ^{60}Co were in range of 51.2 – 95.4 ml/g, 1 – 16.5 ml/g, and 5.22×10^{-5} – 3.24×10^{-6} cm^2/d, respectively (after 60 days). The author noted that this study would contribute to strengthening the engineered trench system for radioactive waste disposal.

Plecas and colleagues [58] also studied the leaching rate of ^{60}Co and ^{137}Cs from a mixture consists of Portland cement mixed with saturated wet cation exchange and bentonite clay. Eight cylindrical samples were prepared for dynamic leach test. IAEA method has been used for the leach experiment, in which leachate solution was replaced after the leaching periods of every day

21

for 7 days, and then every week for 1 month and every month, until 125th day. EG&G–ORTEC spectrometry system and software were utilized to measure the Co and Cs concentration in each the leachate solution. This research found that incremental leach rate (R_n) and apparent diffusivity (D_e) for of ^{60}Co after 125 days were in range between $7 \times 10^{-5} - 4.2 \times 10^{-5}$ cm^2/d and $4 \times 10^{-6} - 1.1 \times 10^{-6}$ cm^2/d, respectively, while for ^{137}Cs were in range of $6.6 \times 10^{-5} - 3.2 \times 10^{-4}$ cm^2/d and $26 \times 10^{-6} - 1.5 \times 10^{-5}$ cm^2/d, respectively. Also, the compressive strengths of these samples were between 23.4 – 29.5 MPa.

A same kind of study was carried by Dessouky et al. [59] to evaluate the leaching behavior of ^{60}Co and ^{137}Cs from two matrices Portland cement and PFA-zeolite cement. Cement samples were prepared of Portland cement with water/cement ratio of 0.5 and other with PFA-zeolite cement at water/cement ratio of 0.35. Static leach test was carried out to evaluate the leaching rate of ^{60}Co and ^{137}Cs radionuclides from these matrices. IAEA standard method was applied and distilled water was used as leachate solution. Here, under the static condition, the leachate solution would not be replaced. A gamma spectrometer with 4"x 4" NaI crystal activated with Thallium was then used to measure the ^{60}Co and ^{137}Cs contents in each leachate solution. Results from this study revealed that the leaching rates of the ^{60}Co and ^{137}Cs were reduced with using PFA-zeolite cement. Additionally, leachability indices (L) for the ^{60}Co and ^{137}Cs radionuclides were exceeded the required value of 6 (the minimum value for acceptance for both waste forms).

Rahman and Zaki [60] have determined the leachability of ^{60}Co and ^{137}Cs and leachability from different immobilized waste forms. Cement-ash samples were prepared using Portland cement mixed with various ashes contents (12 wt%, 20 wt%, and 30 wt%) at different water/cement ratios. Static leach experiment with IAEA standard method was used to evaluate the leaching rate of ^{60}Co and ^{137}Cs radionuclides from these matrices. Distilled water was used as the

22

leachate solution, and analyzed using gamma spectrometer to calculate ^{60}Co and ^{137}Cs radionuclides in it after each leaching period. Different mathematical models were applied to evaluate the leaching parameters. The results indicated that the cumulative fraction leached (CFL) values of ^{60}Co and ^{137}Cs from cement matrices decreased with increasing ash contents—authors suspected that this was due to the low porosity of the ash. However, the leaching phenomena of the waste forms could not be represented by a single mechanism according to the experimental data that were compared to the mathematical models.

Raouf and co-workers [61] conducted a mechanical and leaching assessment for sulfur polymer cement that was used to immobilize the simulated radioactive wastes of Cs, Sr, Ce, Cr, and Pb. The IAEA standard method with static leach tests was performed. Here, the upper surface of the sample was only exposure to the leachate solution while other sides of the sample was covered with wax. The result indicated that the water absorption and open porosity for all matrices were too low (not exceed 2.5%). The compressive strength was in a range of 7 - 14 KN/m^2. Additionally, the leachability index for these elements was higher than the minimum value of 6.0 for acceptance criteria and ranges between about 9-11; and the released ion was ordered as the followings: Sr > Cr > Cs > Ce > Pb.

Chapter 3

Experimental Development with Ce as a Surrogate Material for U (Preliminary studies)

3.1 Introduction

The main goal of this chapter is to explore the feasibility RSC, as agents of immobilization for a non-radioactive material, which can be applied toward fission products and radioactive materials. The results from this study reveals several practical applications worthy of future study. One important implication emerging from this study is that the use of actual radioactive materials, such as uranium and plutonium, is essential for treatability studies and demonstrations prior to implementation; however, there are considerable restrictions and challenges involved with handling, processing, and disposal issues, as well as, the health risks and the excessive cost of associated with conducting demonstrations with these materials. Therefore, for these and other considerations, it is important to identify suitable surrogate nuclear materials to minimize waste generated during the demonstration, gain a better understanding of cementitious waste form properties, estimate behavior of the radiological constituents. For non-radiological work, cerium is the most conservative surrogate for U and Pu, due to similar ionic size, crystal structure, specific heat, thermodynamic stability, and multiple valence states of both Ce and Pu [62, 63]. Therefore, cerium (Ce) was selected as a surrogate material for U and Pu, in cement mixtures with deionized water (DIW) and artificial seawater (ASW) for achievement this work. In addition, it is important to point out that ASW is being explored due to an injection of seawater in the spent fuel pools of Fukushima Daiichi Nuclear Power Station to cool off the reactors; therefore, an understanding of

24

ASW effect on RSC will provide significant insight into physicochemical properties and characteristics. The setting time and mechanical properties of RSC matrix have been evaluated. The microstructure and composition of the waste form were characterized by using techniques such as X-ray fluorescence (XRF), X-ray diffraction (XRD), and scanning electron microscopy (SEM) including energy-dispersive X-ray spectroscopy (EDX).[3]

3.2 Experimental program

3.2.1 Materials

The RSC used for this work was Pavemend 15.0, which is a cementitious, rapid setting, self-leveling structural repair mortar. It is a commercial product obtained from CeraTech, Inc. which consists of magnesium oxide, monopotassium phosphate, and coal ash [64]. The salts (99.9% $CeCl_3$, 99.95% KCl, 99% NaCl, 99.9% $MgCl_2$, and 99.0% Na_2SO_4) used were purchased from Alfa Aesar. DIW with pH of 7 has been obtained by using Millipore Direct-Q® 3 UV Water Purification System (see Figure 3.1). ASW has been prepared based on the revised formula of Lyman and Fleming formulation to make simulated seawater [65]. The reasons of using ASW rather than natural seawater is to produce a solution of known compositions and reduce biological effect [66]. The composition of 1 kg of artificial seawater (35.00% of salinity) consists of (24.88 g/kg) NaCl, (4.157 g/kg) Na_2SO_4, and (0.7237 g/kg) KCl as anhydrous salts, and 52.8 ml of 1 mole $MgCl_2$, which is added to the mixture as a solution.

---

[3] This chapter has been taken from a publication - R. Motny and S. Phongikaroon, "*Effects of Cerium Concentration and Solvent on Physical and Chemical Characterization of Rapid Setting Cement," Nuclear Technology, (2018).* Published online October 2018: *https://doi.org/10.1080/00295450.2018.1510698.*

25

3.2.2 Sample preparation

The experiment focused on the use of this RSC as an emergency agent for a nuclear power accident near an ocean. As such, ASW and $CeCl_3$ were selected as two possible materials that would be found in such an event. The ASW, as an alternative to seawater would be from the injection of the ocean water to cool the reactor cores whereas Ce, as surrogate materials for uranium and plutonium, would come from the nuclear power plant. Based on this, a total of two different sample groups were generated. The first group was a mixture of the cement powder with DIW with different concentrations of Ce (0, 2, 5, 7.5, and 10 wt%) while the second group included the cement powder, ASW, and the same set of Ce concentrations.

The calibration of XRF machine (PANalytical Epsilon 3XLE), as shown in Figure 3.2, is conducted by using the following Standard Reference Material from National Institute of Standards and Technology (NIST): 1880a, 1881a, 1882, 1882a, 1883a, 1884, 1886, 1888, and 1889. The oxide composition of RSC used in the research was measured by XRF and summarized in Table 3.1. All samples were made using the same procedure to maintain consistency. Before any mixing was done, the cement powder was well-mixed by tumbling in a gallon container. Then, the samples were mixed using a 1.27 cm mixing impeller rotated by a hand drill, which was held pointed down by a three-pronged clamp as shown Figure 3.3. A total of 5 g of the cement powder and 1.0 mL of solution was used to make each sample. The powder and solution, in that order, were poured into a clear plastic vial with a 1.905 cm base diameter and 4.826 cm in height. Immediately after this step, they were mixed for a total of six minutes at a maximum speed of 450 rpm to assure that the powder and water were well-combined. After six minutes, the sample temperature was taken using a thermocouple wire to assure that it reached critical mixing temperature of 35°C. These samples were left for setting at least 24 hours before extraction. Using

26

this method, five samples per group were made, for a total of 10 samples, as listed in Table 3.2. Once the samples finished solidifying, they were extracted from the plastic vials.

Figure 3. 1 Millipore Direct-Q® 3 UV Water Purification System used for obtaining DIW.
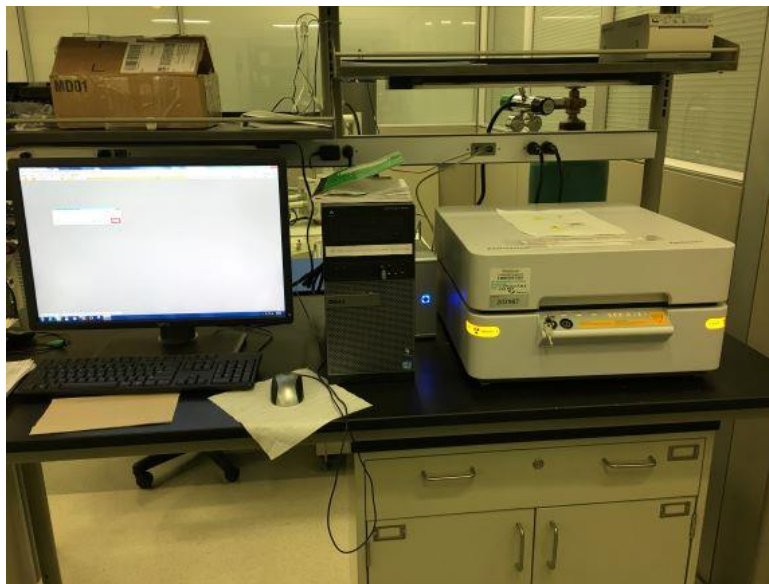
Figure 3. 2 XRF machine (PANalytical Epsilon 3XLE) used for compositional analysis.

Table 3. 1 Chemical compositions of the RSC used.

Compound	Weight (%)	Compound	Weight (%)
SiO_2	28.70 ± 0.01	P_2O_5	24.57 ± 0.03
MgO	8.31 ± 0.04	TiO_2	0.23 ± 0.00
K_2O	22.10 ± 0.02	SO_3	0.60 ± 0.01
Al_2O_3	6.80 ± 0.03	SrO	0.07 ± 0.00
Fe_2O_3	3.61 ± 0.01	MnO	0.01 ± 0.00
CaO	5.10 ± 0.02	Na_2O	0.03 ± 0.01
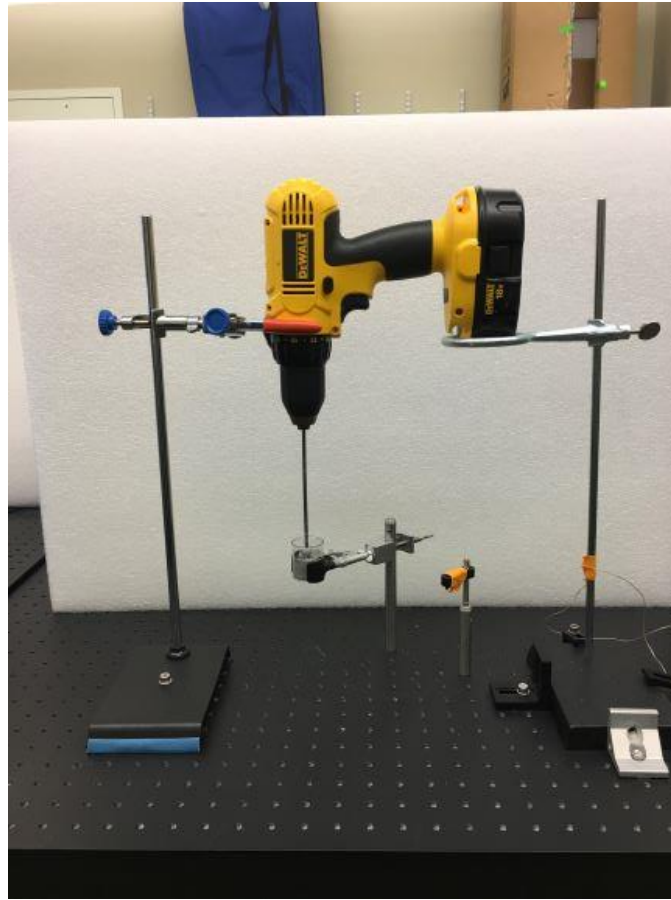
Figure 3. 3 Mixing impeller rotated by a hand drill used for preparing samples.

Table 3. 2 Mixture proportion of RSC and Ce.

Sample	Cement + CeCl₃ (g)	Solution (ml DIW, wt% Ce (wt% CeCl₃)	Sample	Cement + CeCl₃ (g)	Solution (ml ASW, wt% Ce (wt% CeCl₃)
1	5	1, 0 (0)	6	5	1, 0 (0)
2	5	1, 2 (3.5)	7	5	1, 2 (3.5)
3	5	1, 5 (8.8)	8	5	1, 5 (8.8)
4	5	1, 7.5 (13.2)	9	5	1, 7.5 (13.2)
5	5	1, 10 (17.6)	10	5	1, 10 (17.6)

3.2.3 Analytical methods

Setting time tests were carried out by using the Vicat apparatus from Qualitest (63-L0028/1 model), shown in Figure 3.4, which consists of a frame, movable plunger, graduated scale, final needle with size of 40 mm height and 1.13 mm diameter, ASTM method mold, and glass plate. The final setting time was taken when needle failed to make a mark on the surface of the hardened concrete. The compressive strength of the cylindrical samples (Φ 16.5 × 16.5 mm) was determined by using MTS Model Insight 30 Capacity (569329-05 model), shown in Figure 3.5, with the loading speed 0.42 mm/sec.

The test of apparent porosity and bulk density was carried out by applying the method based on the Archimedes principle [67, 68]. First, the total volume (V_T) of the samples was measured by determining the average height and average diameter of the samples. It is important to mention that all samples were dried in an oven (located inside a controlled argon gas environment glovebox) at temperature of 105 ± 5 °C for 24 h $\pm$ 1 hour. Each dried sample was then measured on a balance and being recorded as a dry mass (M_d). Each sample was continually

29

returned to the oven for an additional hour and its mass was being recorded again after each return until reaching a constant mass. After obtaining the final dried mass, this sample was completely submerged in a water container (density ρ_w) for 30 minutes. This submerged mass was suspended with a wire mesh basket to be measured underwater. The result was being recorded as a submerged mass (M_s). That is, the value of M_s is equal to the weight of the sample (out of the water) subtracting by the buoyancy force. Finally, the submerged mass was taken out of the water container and weighed as a wet mass (M_w). Hence, the apparent porosity (P_A) and the bulk density (ρ_B) were determined based on Eqs. (1) and (2), respectively [67, 68].

$$P_A\% = 1 - \frac{(M_d - M_s)}{\rho_w \times V_T} \times 100 \qquad (3.1)$$

$$\rho_B = \frac{\rho_w \times M_d}{M_w - M_s} \qquad (3.2)$$
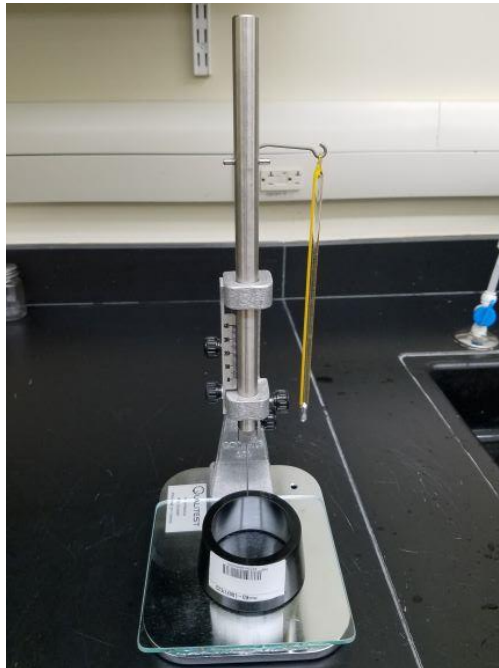
Figure 3. 4 Vicat apparatus from Qualitest (63-L0028/1 model) used for setting time test.

Figure 3. 5 MTS Model Insight 30 Capacity used for the compressive strength test.

Samples were prepared for the phase composition by crushing and then grinding using an agate mortar and pestle shown in Figure 3.6. The powder samples were examined using XRD [PANalytical MPD X'Pert Pro], shown in Figure 3.7, with the high-power ceramic tube PW3373/10 Cu LFF, and a voltage of 45 kV, a current of 20 mA. A diffraction spectrum was collected from 10° to 70° 2θ, with a scanning rate of 2°/min. X'Pert HighScore Plus software was used for an identification of all phases in the samples. Specimens were prepared for the microstructure test by using small amount of previous powder samples and deposited onto aluminium stubs covered with carbon tape and carbon paint. Hence, the aluminium stub surfaces were blown off by using a stream of compressed air to remove any loosened particles. Since the samples were not electrically conductive, the sputter coating technique was employed to obtain surface conductivity by coating the samples with a thin gold layer suing 108 Auto Sputter Coater

31

from Ted Pella Inc. (see Figure 3.8). After that, SEM [Phenom ProX] (see Figure 3.9) at a 15-kV accelerating voltage and a working distance of 15 mm was used to visualize the microstructure of samples. The EDX analysis was carried out using a Phenom ProX to collect elemental maps. These samples were further altered into three discs. Then, sample discs were crushed and grinded into fine powder to analyze chemical composition of the specimen using the XRF.

The pH and conductivity of RSC with different concentrations of Ce in DIW and ASW were determined by using a method developed by Grubb et al. [69]. Here, 5 g of each sample was crushed and mixed for five minutes by using a laboratory stirrer with 10 ml of DIW at a temperature of 23 ± 1 °C. Then, the mixture was filtered through a filter paper P5 from fisher scientific. The mixture was tested with a pH/conductivity meter (Seven Compact™ Duo S213, made by Mettler Toledo) shown in Figure 3.10, to determine the pH and conductivity for each sample with three measurements.

Figure 3. 6 The mortar and pestle used for grinding samples for XRD.

Figure 3. 7 XRD instrument used for an identification of phases in the samples.
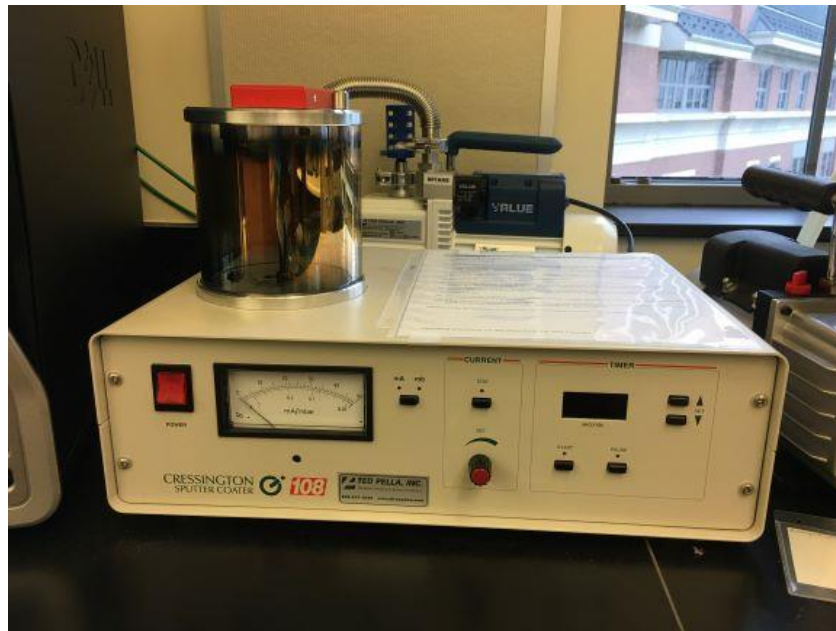
Figure 3. 8 108 Auto Sputter Coater using for coating the samples with a gold layer.

33

Figure 3. 9 The Phenom ProX desktop SEM with EDX.

Figure 3. 10 The pH/conductivity meter.

3.3 Results and Discussion

3.3.1 The setting time

Figure 3.11a shows the final setting times (FST) of RSC with the different water/cement (w/c) ratios. Here, (w/c) ratio was changed by increasing water content; however, all other batch amounts are maintained constant. The results show that FST increase as (w/c) ratio increases. In addition, the results reveal that the RSC exhibits the best and lower FST (12.5 mins ± 2) at 0.2 w/c ratio. So, RSC binder with such a good FST could be used in the field for emergency cases. In contrary, the setting time of cement is influenced by the amount of Ce added (see Figure 3.11b). Here, the FST of RSC binder at 0.2 w/c ratio with different ratios of Ce (2, 5, 7.5, and 10 wt%) with DIW and ASW, respectively, were decreased with increasing Ce content.

Technically, the setting time plays an important role in the immobilization of radioactive waste, as it is an indication of compatibility between the waste and cement. Therefore, it is important to ensure that the solidification does not occur before the mixture is totally homogenized and then becomes solid for secured handling, storage, and transportation. The measured setting times showed that the addition of cerium to RSC matrix has accelerated the hardening reaction. This behavior is due to parallel reactions between ions present in the solutions and the cement (e.g., the potassium with chloride [70]), which in turn increases the temperature and the setting time of the mixture. This behavior becomes more prominent with the increased amount of cerium chloride and also with other salts added to make the artificial seawater. In comparison with a conventional cement [71], an addition of cerium shows a complete opposite behavior (see Table 3.3), indicating that RSC can be a good alternative material for immobilizing rare earth elements and possibly U/Pu.

Furthermore, the most important factor that affects the setting time of concrete is water-cement (w/c) ratio, which also has a wide range based on a type of each working application. For example, the w/c values required to chemically hydrate the Portland cement at ambient temperature are between 0.18 and 0.23, while a higher waste loading for liquid radioactive wastes is desired (assuming a higher w/c ratio is used) [14]. Therefore, for each specific case, there is an optimum w/c ratio yielding different final setting times. By comparing the final setting times at different w/c ratios for RSC with three types of Portland cement (type A, B, and C) [72], it can be seen that RSC will take longer time to solidify after w/c ≥ 0.3. Therefore, the resulting w/c ratio is in a narrow range as shown in Table 3.4. The results here suggest that RSC can be used effectively for an emergency purpose and immobilization of possible radionuclides to minimize exposer times of workers.
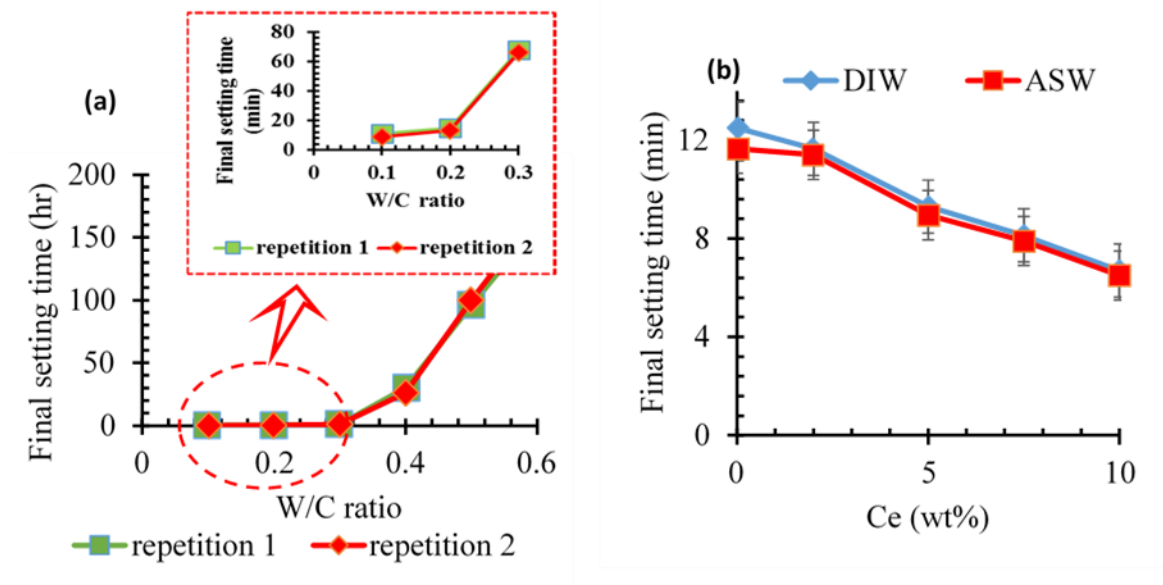
Figure 3. 11 (a) FST of cement with water to cement ratio (W/C) and (b) FST of cement at 0.2 W/C ratio at different Ce contents (± 2.41 min for DIW and ± 1.99 min for ASW).

Table 3. 3 Effect adding $CeCl_3$ on FST from other study, comparing with FST in this study.

$CeCl_3$ (wt%)	Final setting time (minutes)		
	RSC + DIW	RSC + ASW	Epoxy modified cement Ref. [71]
0.5	---	---	235
1	---	---	250
3	---	---	270
3.5	11.65	11.4	---
8.8	9.3	8.95	---
13.2	8.125	7.9	---
17.6	6.7	6.5	---

Table 3. 4 Comparing FST from other studies with FST in this study.

w/c ratio	Final setting time (minutes)			
	RSC	Cement A Ref. [72]	Cement B Ref. [72]	Cement C Ref. [72]
0.1	11	---	---	---
0.2	12.5	---	---	---
0.3	66	---	---	---
0.35	---	180	286.8	309
0.4	1560	234	345	373.8
0.5	6000	361.2	425.4	405.6
0.6	9840	368.4	480.6	475.2

3.3.2 Visual observation

Figures 3.12a and 3.12b show samples images of RSC with different ratios of Ce (2, 5, 7.5, and 10 wt%) with DIW and ASW, respectively. After the casting of the concrete samples, it was noticed that the samples with increasing concentration of cerium had gray surfaces, while the

37

reference samples without cerium had dark surfaces. In addition, salt deposits were formed on the surface of some samples mixed with DIW and ASW.
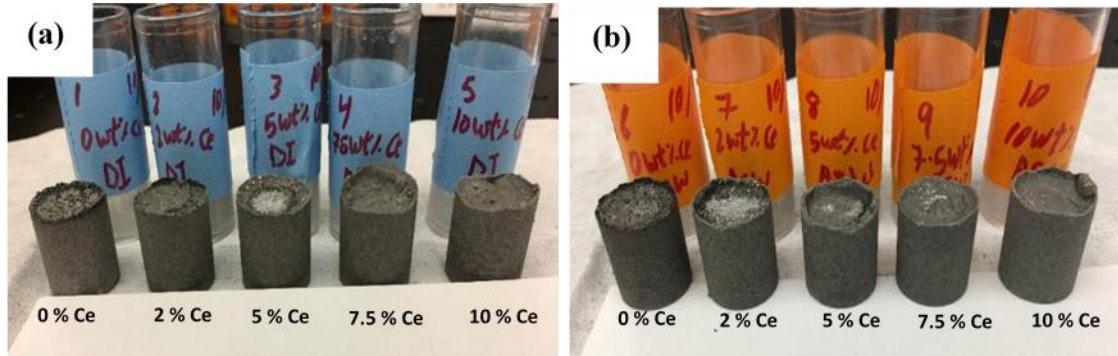
Figure 3. 12 Pictures of samples of RSC with different ratios of Ce and (a) DIW and (b) ASW.

3.3.3 Apparent porosity and bulk density

The reason behind the decrease in strength of ceramic materials on bearing the high loads is due to the area reduction of the transversal section, in which axial loads are applied, resulting from porosity [70]. The apparent porosity of samples of cement and different Ce concentrations with DIW and that with ASW are shown in Figure 3.13a. The porosity of the final waste forms has increased with the increase of $CeCl_3$ for both solutions (DIW and ASW) because an addition of these salts has reduced the amount of free water joined in the reaction—thus the remaining amount will decompose and produce either H_2 or O_2. This will form a capillary system which can result from turning the place occupied by free water into void after the solidification of the mixture. These properties are important because they are related to durability and leachability, which can be helpful in interpreting other test results such as hydraulic conductivity. Although the increase of the porosity of the final waste forms can reduce the compressive strength, it is still less than the porosity of the conventional cement, such as OPC which has a porosity of 31.18% before adding any waste products [6, 73, 74]. This outcome proves the general observation reported in Table 3

www.manaraa.com

in Ref. 11, that RSC could be prepared with potable and non-potable water. The density of RSC with DIW and ASW is increased progressively with the addition of Ce, as shown in Figure 3.13b. The densities of RSC are about 1.69 ± 0.01 g/cm^3 and 1.72 ± 0.02 g/cm^3 with DIW and ASW, respectively, when the Ce concentration was 0 wt%. At 10 wt% Ce concentration, both densities increased to 1.84 ± 0.02 g/cm^3 and 1.905 ± 0.03 g/cm^3 with DIW and ASW, respectively.
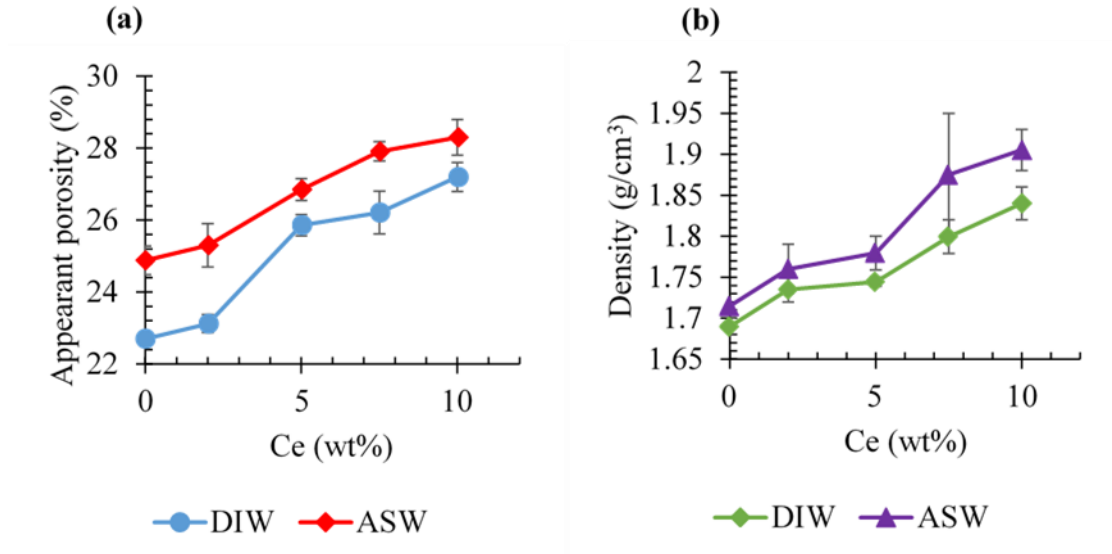
Figure 3. 13 (a) Apparent porosity of RSC with DIW and ASW at different Ce concentrations (b) Bulk density of RSC with DIW and ASW at different Ce concentrations (measurements are expressed as mean ± standard deviation).

3.3.4 Compressive strength

The effects of different ratios of Ce (2, 5, 7.5, and 10 wt%) on compressive strength of RSC samples with DIW and ASW are presented in Figure 3.14. It can be seen that the compressive strength values reduce remarkably with an increase of Ce content in both DIW and ASW. The compressive strengths of RSC are about 11.2 ± 0.9 MPa and 13.25 ± 0.6 MPa with DIW and ASW, respectively, when there is no present Ce concentration. However, these values are reduced by half, about 4.1 ± 0.3 MPa and 5.1 ± 0.7 MPa, with DIW and ASW, respectively, at 10 wt% Ce concentration. The recommended compressive strength for the final solid waste form is required

39

to be at least 3.4 MPa according to the Nuclear Regulatory Commission (NRC) [14, 62]. It should be noted that the lowest compressive strength values of the mixture with both DIW and ASW were higher than the recommended condition.
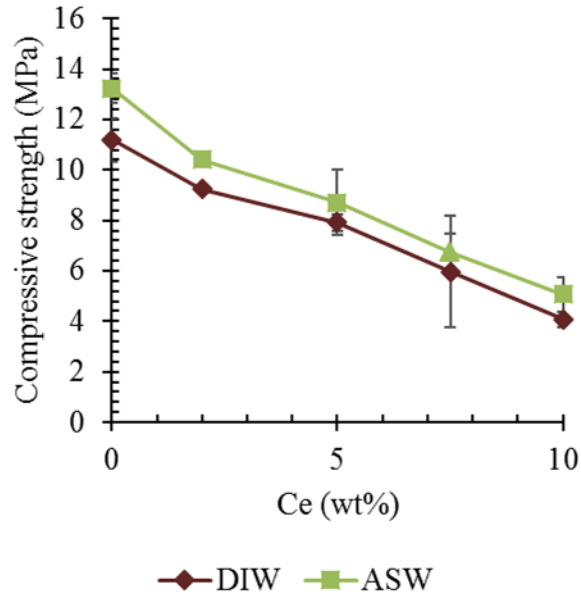
Figure 3. 14 Compressive strength of RSC with different Ce contents in DIW and ASW (measurements are expressed as mean ± standard deviation).

3.3.5 XRD analysis

The diffraction patterns of the 5 samples obtained by RSC and various Ce contents with DIW and those with ASW, respectively, are all shown in Figure 3.15a and 3.15b. The main oxides phases identified at the composites with DIW and ASW are struvite-K ($KMgPO_4.6H_2O$), quartz (SiO_2), and periclase (MgO). The intensity of the characteristic peaks considerably reduces when Ce concentration increases; in addition, there is a new peak showing around ($2\theta = 28.207°$) for $Ce_{4.667}(SiO_4)_3O$ phase growing up as Ce concentration increases. Another new small peak showing around ($2\theta = 58.601°$) for $CeAl_{11}O_{18}$ phase is indicated in Figure 3.15a and 3.15c. There are some differences in the characteristic peak intensity and a slight displacement of the diffractograms between the samples with DIW and those with ASW. Due to the high chloride ion (Cl^-) content

40

in ASW, a quantity of Cl⁻ bonded with K⁺ to form KCl crystals distributed in the matrix, which in

turn reduced the struvite-K phase and weakened the bond between hydration product crystals.
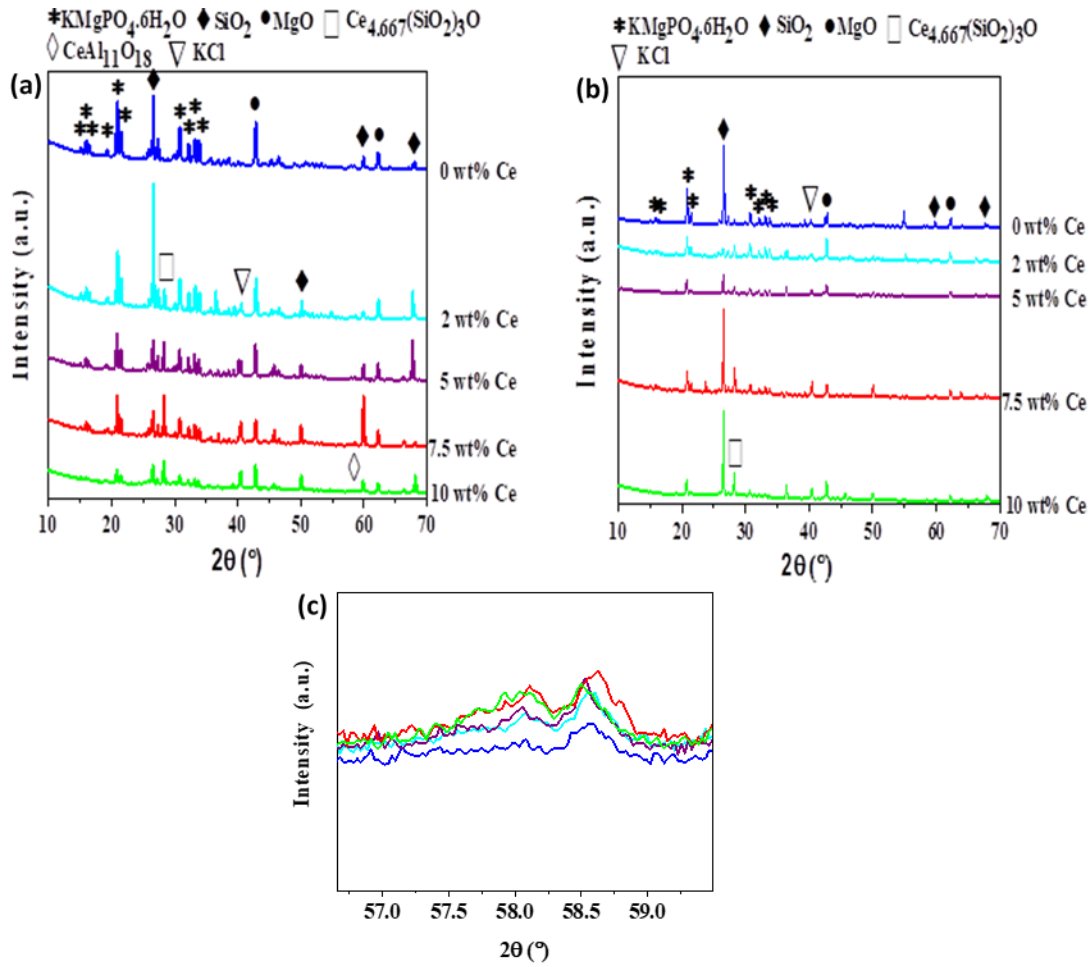
Figure 3. 15 XRD patterns of the cement samples with (a) DIW and (b) ASW at different Ce concentrations (c) the peak around ($2\theta = 58.601°$) for $CeAl_{11}O_{18}$ phase—region from Figure 3.15a.

3.3.6 XRF analysis

The distribution of Ce measured by using XRF on samples of RSC and different Ce concentrations with DIW and that with ASW are shown in Figure 3.16a and 3.16b. The results of XRF analysis (in wt% Ce) are presented as bars with a depth resolution of 5 mm. The distribution of Ce content in the samples was approximately uniform with the depth, despite some contents of cement and Ce were sticking to the impeller during mixing (considered as lost contents).
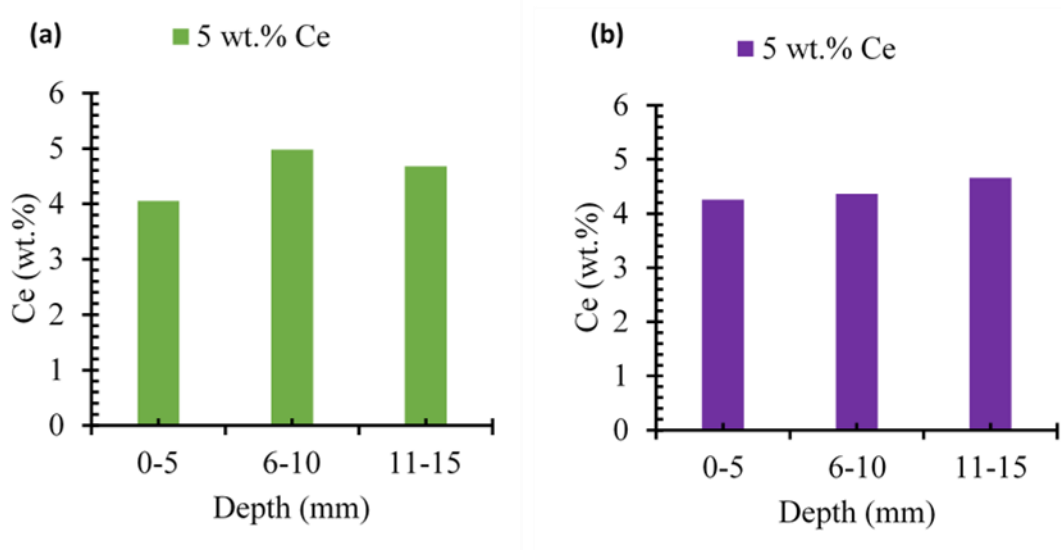
Figure 3. 16 Depth profile of RSC with (a) DIW with 5 wt% Ce (b) ASW with 5 wt% Ce.

3.3.7 pH value and Conductivity

The pH values of RSC and various Ce contents with DIW and those with ASW, respectively, were measured. The results are shown in Figure 3.17a indicating a significant reduction of pH values with the increase of Ce content in both DIW and ASW. Furthermore, the pH values for RSC with ASW are less than that with DIW; however, the pH values of RSC are

still within the basicity range. Since most salts had pH values that range from neutral to mildly acidic, thus the addition of salts would have lowered the pH in the RSC. This result is a good indicator because, for example, used Magnox fuel after storage under water contains metallic uranium or other waste metals such as aluminum, which is not compatible with the conventional cementing systems that have a high alkaline environment. This would corrode the waste metals—thus, cracking of the waste form and releasing of hydrogen gas. It should be further noted that aluminum is passive in the region of pH 4 to 8.5 [75, 76].

The electrical conductivity is also another important physical property of the concrete. It can be used to relate certain concrete characteristics such as the electrical resistivity, which is the inverse of electrical conductivity and associated to corrosion process [77]. Figure 3.17b displays the electrical conductivity values of RSC and various Ce contents with DIW and those with ASW, respectively. These values were increased considerably with an increase of Ce content in both DIW and ASW. The reason for an increase in conductivity is due to the fact that an addition of salts leads to increase in ions concentration of (Na^+ and Cl^-), which in turn, can lead to enhance the electrical current flow.
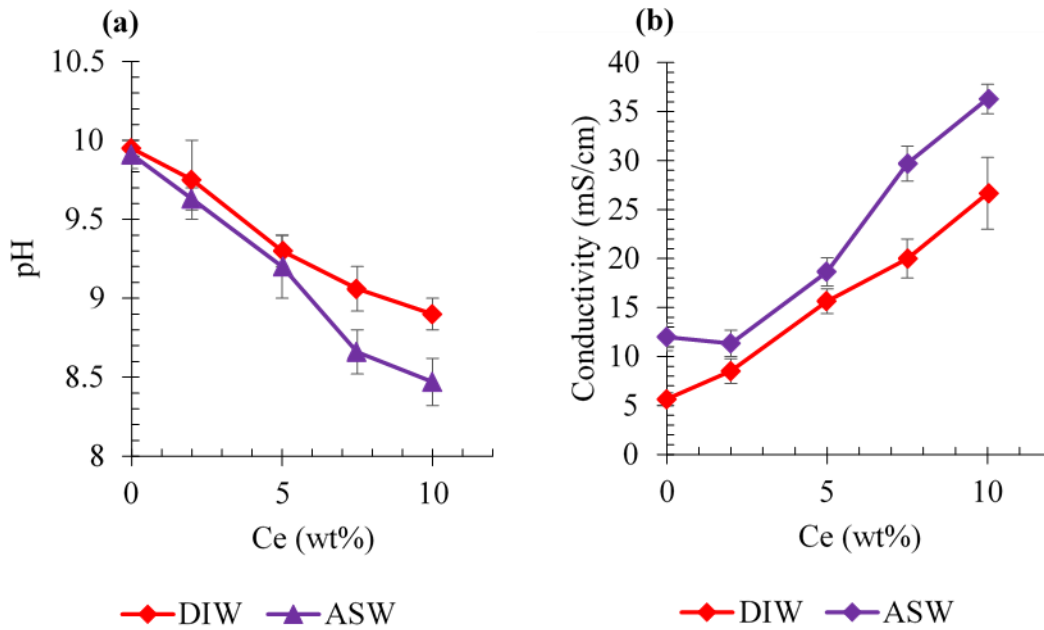
Figure 3. 17 (a) pH and (b) conductivity of RSC with DIW and ASW at different Ce concentrations (measurements are expressed as mean ± standard deviation).

3.3.8 Microstructure and elemental mapping analysis

A SEM micrograph along with three EDX spectrums taken from various locations of the RSC sample with 0 wt% Ce and DIW are presented in Figure 3.18. It can be seen that there is no continuous structure and the microstructure; in general, it seems to be porous. The shape of the particles is entirely different, where struvite-K particles are in the form of laminar flat plates, while different sizes of spherical particles correspond to fly ash particles. The results from the EDX spectrums (Figure 3.18a) show the compositions at these locations as follows: (1) majority of Si and Al minerals, (2) struvite-K crystals, and (3) unreacted MgO and trace amounts of P and K. The EDX spectra also revealed the presence of the gold (Au) peaks because of the gold sputter coating applied on samples to be electrically conductive. The EDX maps (Figure 3.18b) of the RSC sample with 0 wt% Ce and DIW exhibited a homogeneous distribution of K, Mg, and P

44

throughout the sample which indicates that struvite-K phase is the dominant binding phase of the system. Also, it can be seen that MgO particles were remained unreacted and randomly distributed within the structure. Al and Si were incorporated together to form spherical particles with different sizes which represented the unreacted fly ash particles while the iron (Fe) element was scattering in the matrix.

Figure 3.19 shows the SEM-EDX of the RSC sample with 10 wt% Ce and DIW. The results show that the struvite-K particles appeared with a completely different shape than of that without Ce. It can be seen that the struvite-K particles are joined together to form a large undefined shape or an approximately cubic. The EDX analysis of locations (1 and 2) for the undefined shape and an approximately cubic crystal showed that the major elements were P, K, Mg, and O. Also, the microstructure shows that there are still some fly ash particles in the system with chemical elements (Si, Al, and Fe) of location (3), while unreacted MgO is not shown in the figure. Furthermore, EDX result of location (4) displays the existence of Ce spread on the pore wall with the following elements: Si, Al, Mg, K, P, Fe and O.

The microstructure and EDX of the RSC sample with 10 wt% Ce and ASW is shown in Figure 3.20. The results present a clear difference that can be identified between this sample and the previous samples. The microstructure of this sample is more porous than those with DIW. In addition, it can be seen that the unreacted MgO crystals are significantly increased comparing with the previous ones. EDX result of location (1) shows that the dominant element is Mg. Whereas the EDX analysis of point (2) indicates that Ce is being clustered with the following elements: Si, Al, Mg, K, P, Fe and O. FA particles have same spherical shape with the main chemical elements (Si and Al) as shown in location (3). EDX result of location (4) reveals that there is a big quartz particle with the main element Si and trace amounts of Al, Mg, K, P, and O.

45
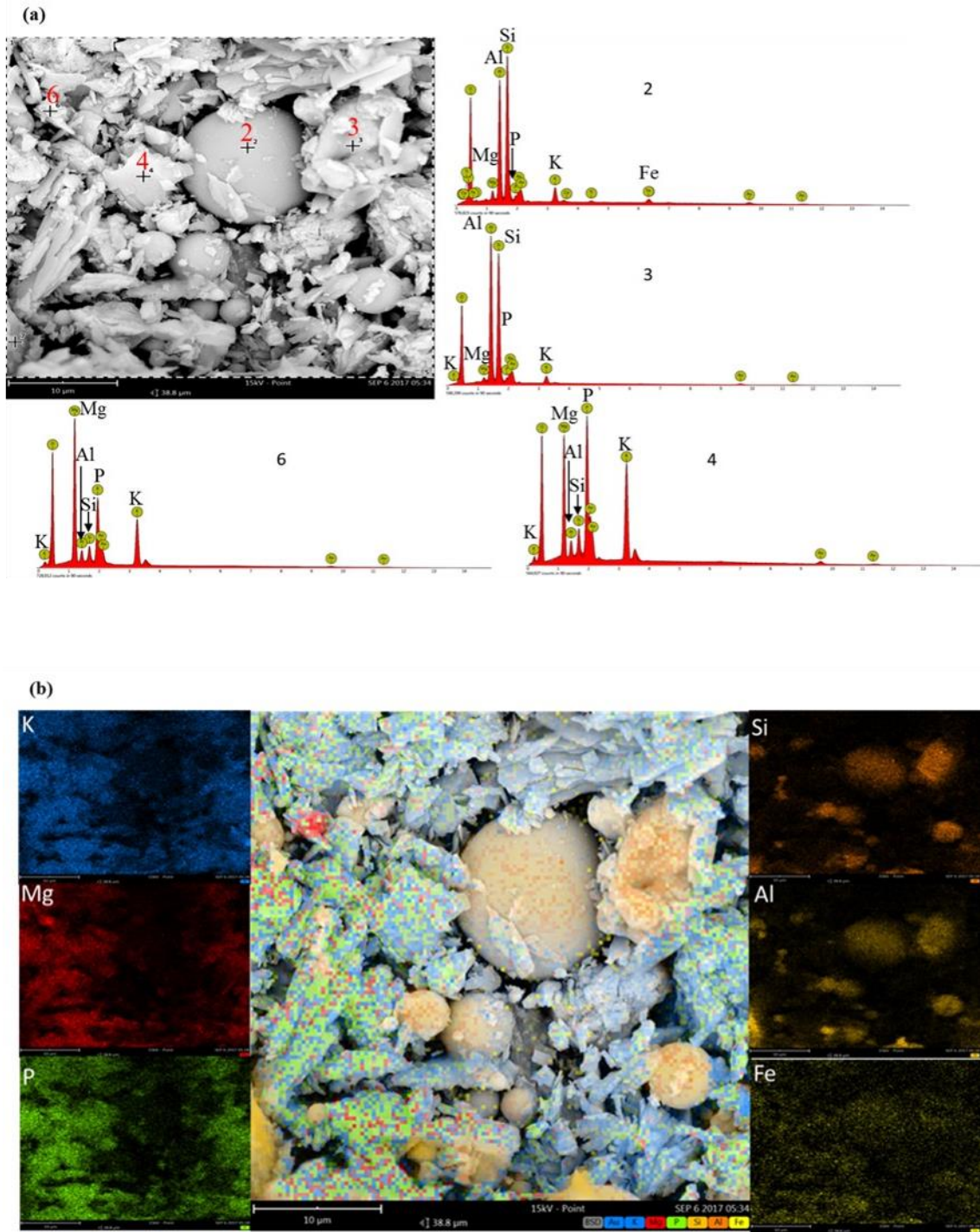
Figure 3. 18 (a) SEM micrographs of RSC with DIW and 0 wt% Ce, with (b) EDX patterns.
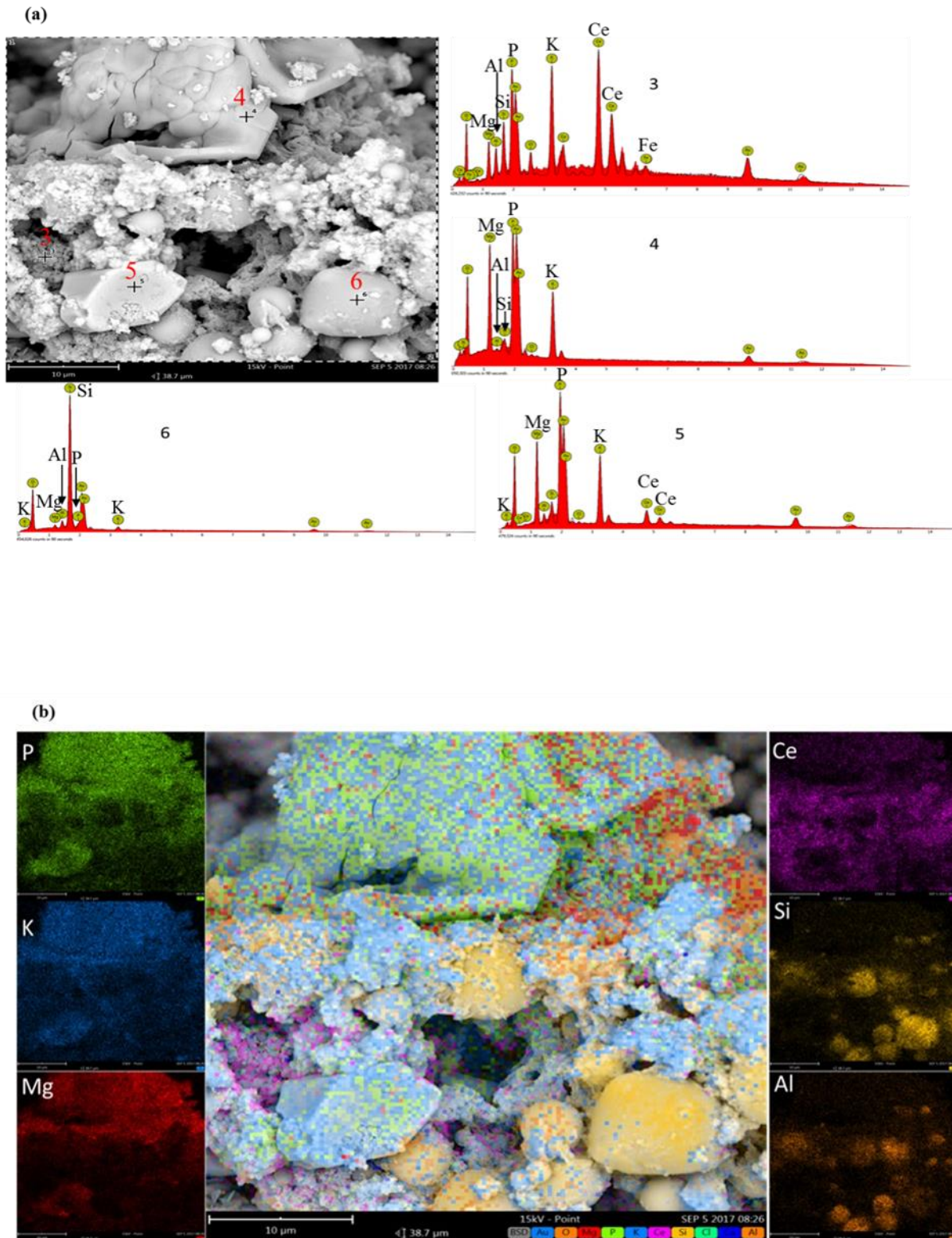
Figure 3. 19 (a) SEM micrographs of RSC with DIW and 10 wt% Ce, with (b) EDX patterns.
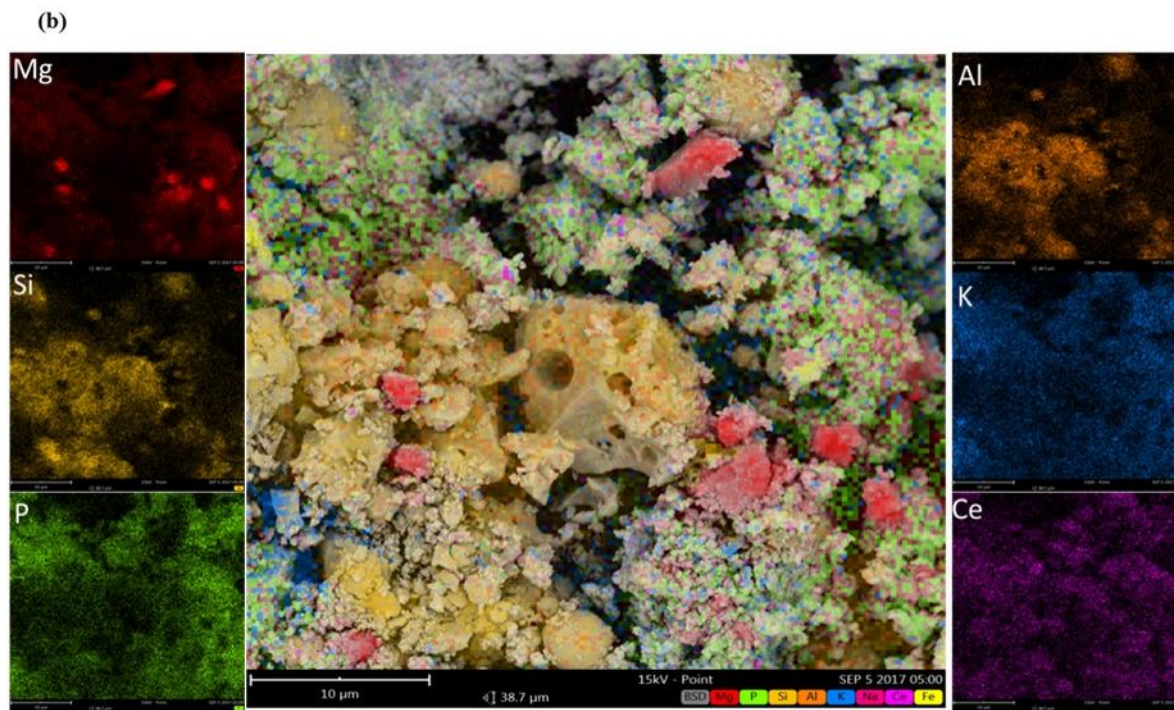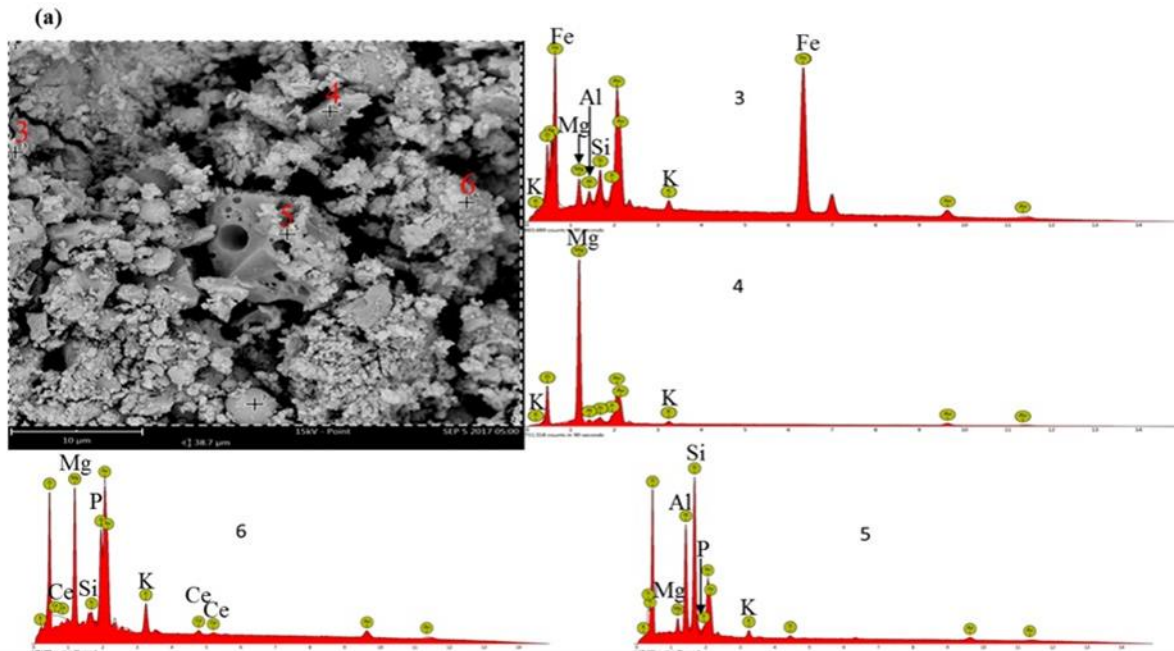
Figure 3. 20 (a) SEM micrographs of RSC with ASW and 10 wt% Ce, with (b) EDX patterns.

3.4 Conclusion

This study presented results of immobilization of Ce at 0, 2, 5, 7.5, 10 wt% concentrations in RSC with DIW and ASW. It was found that the final setting time and compressive strength of RSC with both solutions (DIW and ASW) were decreased with increase of Ce contents while the apparent porosity and bulk density of RSC were increased with increase of Ce concentration. The XRD patterns revealed that the intensity of the characteristic peaks considerably reduced with the increase of the Ce concentration, as well as, there was a new peak showing around ($2\theta = 28.207^\circ$) for $Ce_{4.667}(SiO_4)_3O$ phase growing up as Ce concentration increased. A new small peak showing around ($2\theta = 58.601^\circ$) for $CeAl_{11}O_{18}$ phase was discovered in the sample. The XRF results showed an even distribution of Ce concentrations within RSC with both solutions (DIW and ASW). The addition of salts was led to lowering of the pH value and increasing the conductivity. There were considerable differences in the morphology of struvite-K crystals and MgO crystals among RSC samples with different Ce contents and solvents (DIW and ASW). It can be seen the struvite-K was in the form of laminar flat plates and MgO was spread and/or unreacted in the matrix with DIW. In contrary, the struvite-K particles were undefined shape and there was much unreacted MgO spread in the matrix with ASW. In addition, there was the existence of Ce distributing onto the pore wall or clustering with the following elements: Si, Al, Mg, K, P, Fe and O. The results from this study reveal several practical applications. By comparing to other cements used in waste immobilization, the results here suggest that RSC can be a viable option for an emergency purpose and immobilization of possible radionuclides to minimize exposure times for workers.

49

Chapter 4

Measurement of a Surrogate Material (Ce and Cs) in Cement Matrix

4.1 Introduction

There are several analytical techniques that can be used for obtaining compositional analysis. These common-used techniques are destructive and time-consuming. In addition, their processes often generate radioactive waste, a feature that is critical when dealing with nuclear material; several examples are inductively coupled plasma mass spectrometry (ICP-MS) and X-ray fluorescence (XRF) [78-82]. Definitely, an inappropriate for field application can be the use of neutron activation analysis (INAA) [78-82]. Also, the probability of human diseases or even death resulting from contamination and radiation exposure would be increased for people who are in situ with hand detectors close to the radioactive materials [83].

Therefore, laser induced breakdown spectroscopy (LIBS) has been proposed as a promising technique for compositional analysis to fulfill above requirements because it is nearly non-destructive for any material phase (solid, liquid, and gas), noncontact, high accuracy, high remote sensing capability with fast analysis, and capability to measure all elements from the periodic table. Also, LIBS offers a real-time and in-situ elemental analysis with very little sample preparation (< 1 μg) [84-87]. LIBS can be used to obtain compositional analysis in harsh environments such as hot cells and radioactive glove boxes [88]. Finally, the number of environmental sampling for safeguards could be minimized using LIBS as a prior examination tool to detect material deposits on environmental swipe samples. [89].

The main purpose of this chapter is to explore LIBS technique on non-radioactive materials in the rapid setting cement (RSC), which can be applied toward fission products such as (^{137}Cs and ^{90}Sr) and unrecovered uranium and plutonium. Cerium chloride (CeCl$_3$) and cesium chloride (CsCl) were selected as surrogate materials for (UCl$_3$ and/or PuCl$_3$) and fission products, respectively. Univariate calibration curves, principal component analysis (PCA), and partial least squares (PLS) were investigated and discussed.

4.2 Experimental program

4.2.1 Apparatus

The LIBS system used in this study consists of Nd:YAG laser (Q-smart 450) from Quantel USA coupled with the Aurora LIBS Spectrometer from Applied Spectra Inc, as shown in Figures 4.1 and 4.2, respectively. This laser can deliver maximum pulse energy of 450 mJ (FL-Q-Switch = 6 μs) at 1064 nm and operate at a pulse repetition rate of 10 Hz (Q-Switch divider = 1). The lasing frequency can be controlled by adjusting the Q-switch divider, while the laser energy can be changed by adjusting the FL-Q-Switch delay in which by increasing the Q-switch delay, the energy decreases. The laser energy was measured with a laser power and energy monitor (MAESTRO) from Gentec EO as shown in Figure 4.3. This device is fully touch screen controls based on a 5.6 inch color LCD screen with (640 × 480 resolution and 18 bit color) and energy range from 30 fJ to 30 kJ. Aurora LIBS spectrometer used in this study has the following features:

- Six channel high-resolution,
- Broadband CCD spectrometers with spectral coverage from UV to NIR (190 to 1040 nm),
- High transmission fiber optics bundle with fiber split ends up to 6 channels.

51

- Spectral resolution is < 0.1 nm for UV to VIS and < 0.12 nm for VIS to NIR.

- Adjustable gate delay from 50 ns to 1 ms with 25 ns step resolution.

Figure 4. 1 Picture of the Q-smart 450 Nd:YAG laser used in this work.

Figure 4. 2 Picture of Aurora LIBS spectrometer used in this work.
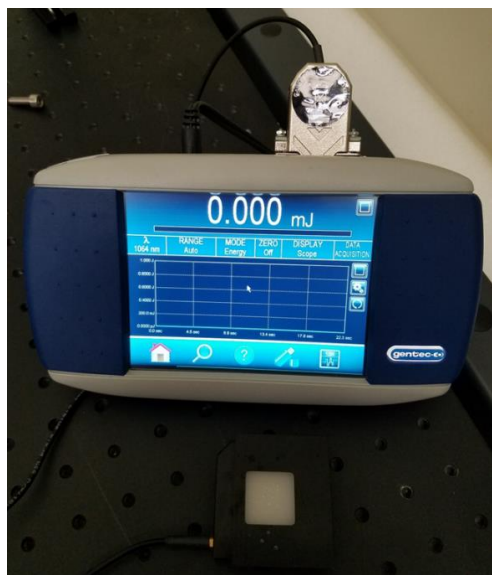
Figure 4. 3 Picture of the laser power meter used to determine the laser energy.

4.2.2 Sample preparation for LIBS analysis

All sample preparations were discussed in details in Chapter 3. The experimental program was summarized in Tables 4.1 and 4.2. Once the samples finished solidifying, they were extracted from the plastic vials. All samples maintained their cylindrical shape of the vial with the top surface drying with a meniscus shape. This shape was not ideal for LIBS analysis; thus, all samples were modified to better fit the LIBS setup. The meniscus area was very brittle; it was easily removed by using a metal file. These filed surfaces will be considered the bottom of the samples as they are curved and would not be the best choice for LIBS. To maintain consistency in dimensions, all samples were filed down to a height of 12.5 mm. In order to better understand where, if any, of the desired elements had been immobilized in the cement, these samples were further altered into three discs. Each disc was cut to be 3 mm in thickness with the exception of the bottom disc that contained the filed surface. So, the first surface to be analyzed was the top of the first disc. The second surface to be analyzed was on the second disc representing a depth of 3 mm from the top surface. The third surface was on the third disc representing a depth of 6 mm from the top surface.

Buehler IsoMet low speed cutting machine with a cubic boron nitride blade, as shown in Figure 4.4, was used to cut the samples into discs, which removed about 0.1 mm of material per cut. In addition, since the samples were small, some discs cracked at the edges or did not have parallel surfaces. So, to eliminate these differences in dimensions, the discs were further modified for LIBS. To provide a constant sample height for each laser shot, the discs were placed on top of modeling clay inside a cylindrical mold. This plastic mold had the same diameter as the discs and a height of about 10 mm. The discs were gently pushed down into the clay up to a height of 10 mm. Once they were extracted from the mold, all discs would be flat and the modeling clay would support them at the same height. The filed sample, its discs, and LIBS preparation are shown in Figure. 4.5. This method solved the problem of unequal disc thicknesses but not the fact that some discs had cracked and chipped at the edges. To solve these differences in surface area, the laser shot locations were made to be 3 mm from the center of the discs. This location was about half the radius of the discs and ensured all shot locations had enough surface area to analyze.

Table 4. 1 The experimental program showing a list of 20 samples made at various $CeCl_3$ and CsCl concentrations in RSC with DIW.

Sample no.	Cs wt%	Ce wt%	Sample no.	Cs wt%	Ce wt%	Sample no.	Cs wt%	Ce wt%
1	0.5	0.5	8	1.0	2.0	15	2.0	8.0
2	0.5	1.0	9	1.0	4.0	16	4.0	0.5
3	0.5	2.0	10	1.0	8.0	17	4.0	1.0
4	0.5	4.0	11	2.0	0.5	18	4.0	2.0
5	0.5	8.0	12	2.0	1.0	19	4.0	4.0
6	1.0	0.5	13	2.0	2.0	20	4.0	8.0
7	1.0	1.0	14	2.0	4.0			

Table 4. 2 The experimental program showing a list of 20 samples made at various $CeCl_3$ and CsCl concentrations in RSC with ASW.

Sample no.	Cs wt%	Ce wt%	Sample no.	Cs wt%	Ce wt%	Sample no.	Cs wt%	Ce wt%
1	0.5	0.5	8	1.0	2.0	15	2.0	8.0
2	0.5	1.0	9	1.0	4.0	16	4.0	0.5
3	0.5	2.0	10	1.0	8.0	17	4.0	1.0
4	0.5	4.0	11	2.0	0.5	18	4.0	2.0
5	0.5	8.0	12	2.0	1.0	19	4.0	4.0
6	1.0	0.5	13	2.0	2.0	20	4.0	8.0
7	1.0	1.0	14	2.0	4.0			

Figure 4. 4 IsoMet™ low speed precision cutter.
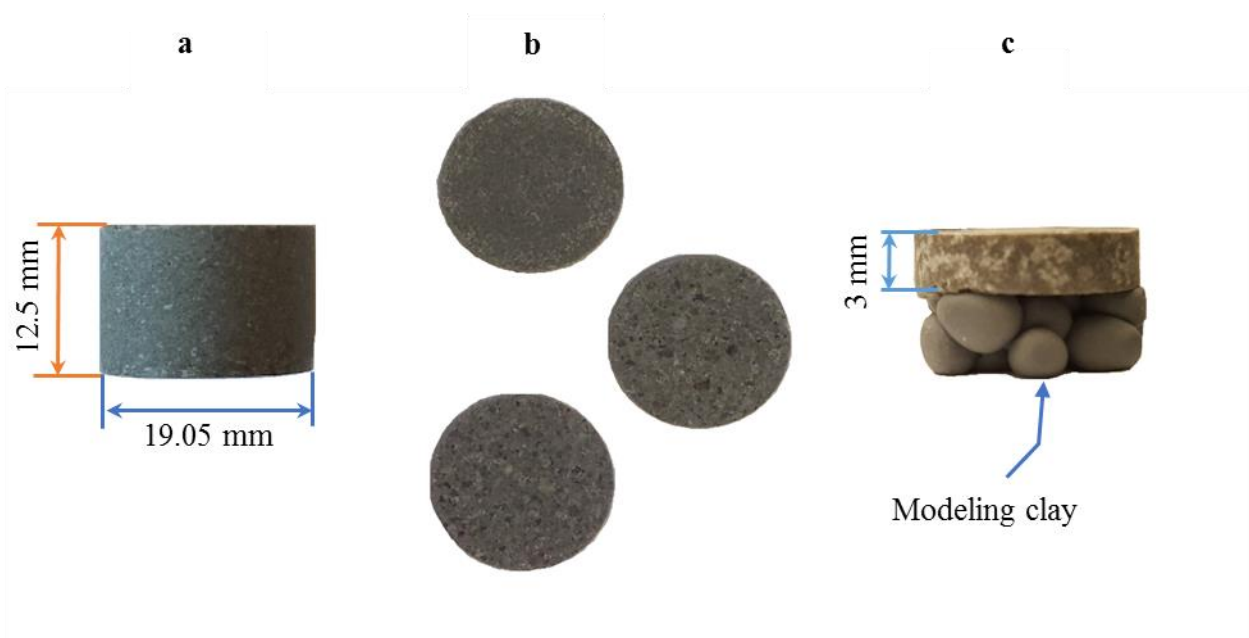
Figure 4. 5 A method of sample preparation for LIBS: (a) The filed sample; (b) sample was cut into three discs; and (c) each disc was placed on top of modeling clay.

4.2.3 LIBS setup and optimal conditions

LIBS experimental setup used in the analysis of cement with nonradioactive elements (Ce and Cs) samples is shown in Figure 4.6. The laser was targeted towards the sample discs using three mirrors and a biconvex focusing lens with a focusing length of 125.0 mm. The plasma light was collected by a biconvex lens with focusing length of 50.0 mm and focused by another biconvex lens with a focusing length of 100.0 mm. The light was focused into a fiber optics cable and collected by a multichannel Aurora LIBS spectrometer. The laser was coarsely aligned using the Z-fold alignment pattern. Back-reflection into the laser was prevented by misaligning the laser out of the biconvex lens by two millimeters from the centerline. Further optimization of the system was done by adjusting the position of the biconvex lenses and monitoring acquired intensities. The cement samples could not be used at this stage as they did not seem to be homogeneous and

56

behaved erratically for optimization purposes. Instead, a Li peak at 670.776 nm from the modeling clay was used. After minor adjustments to the focusing lenses to reach the maximum intensity of the Li peak, the system was ready to perform the analysis. The disc samples were placed on top of a rotating platform that would allow for a full rotation. The focused laser came down to the disc surface at a location 3 mm from the center of the disc. Six locations were shot per disc by rotating the platform 60 degrees per new location. Each location will have a total of 100 laser shots.
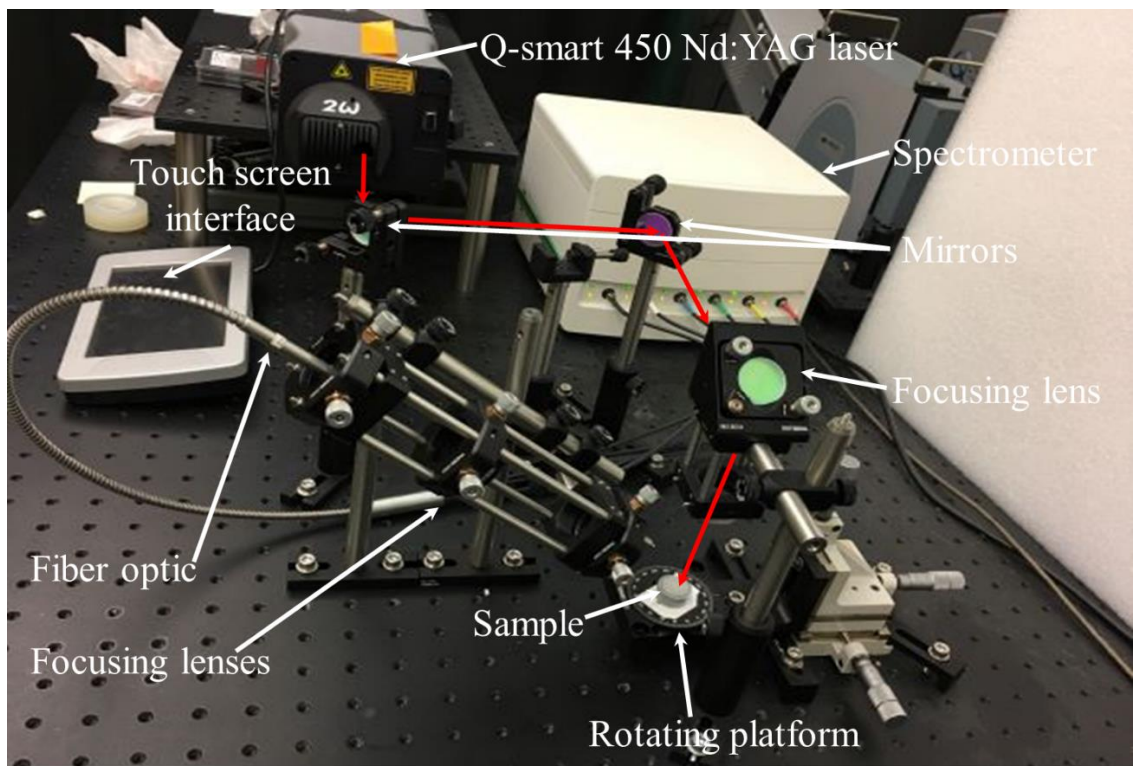
Figure 4. 6 Picture of LIBS experimental setup used in this work.

4.3 Calibration curves

A calibration curve method is a regression model used for the quantitative estimation of unknown samples. This method represents the relationship between the instrument response and the concentration of a substance. In this study, the response is either peak intensity or peak area.

Here, the response versus the sample concentration will display a linear relationship that can be described by the following equation [90]:

$$y = b_0 + b_1 x \tag{4.1}$$

where y is the spectral response, x is the concentration of a sample. Here, b_0 and b_1 are the slope and the y-intercept of the linear regression line, respectively, which can be determined by:

$$b_1 = \frac{\sum[(x_i - \bar{x})(y_i - \bar{y})]}{\sum(x_i - \bar{x})^2} \tag{4.2}$$

and

$$b_0 = \bar{y} - b_1 \bar{x} \tag{4.3}$$

where x_i is the concentration at a given point, y_i is the response at a given point, $\bar{x}$ is the mean of all the concentration values, and $\bar{y}$ is the mean of the detector responses. The correlation coefficient (R^2) represents the statistical measure used to evaluate the goodness of fit of a regression model which can be calculated by [91, 92]:

$$R = \frac{\sum[(x_i - \bar{x})(y_i - \bar{y})]}{\sqrt{\sum(x_i - \bar{x})^2 \sum(y_i - \bar{y})^2}} \ . \tag{4.4}$$

Another important parameter with the calibration curve method is the standard deviation. This is a measure used to determine the quantity of variation of a set of data values. The standard deviation ($S_{y/x}$) were calculated by:

$$S_{y/x} = \sqrt{\frac{\sum(y_i - \hat{y}_i)}{n_r - 2}} \tag{4.5}$$

where $\hat{y}_i$ is the predicted values for the best fit in the linear regression and n_r is the number of samples. Similarly, the root mean squared error (RMSE) is the standard deviation of the residuals. The formula for calculating RMSE is the same that used for the standard deviation except the equation denominator will be $n_r - 1$. The 95% confidence level has been used to determine the uncertainties or standard deviations for the slope and y-intercept. The formula given below shows the upper and lower confidence intervals (y_{CI}) for the regression line [90, 91]:

$$y_{CI} = \hat{y}_i \pm t_{95\%} S_{y/x} \sqrt{\frac{1}{n_r} + \frac{(x_i - \bar{x})^2}{\sum(x_i - \bar{x})^2}} \tag{4.6}$$

4.4 Limit of detection and cross validation

One of the key figures of worthiness evaluated in validation studies or the performance of an analytical technique is the limit of detection (LOD). This value represents the minimum amount or concentration of a substance that can be reliably detected under optimal conditions. The LOD is given by [46, 91]:

$$LOD = \frac{3\sigma_b}{b_1} \tag{4.7}$$

where σ_b is the standard deviation of the blank value or around expected value (the lowest concentration was used), b_1 is the slope of the calibration curve, and the factor 3 corresponds to a relative result uncertainty of approximately 33%. The root mean squared error of calibration (RMSEC) was calculated in order to measure goodness of fit between experimental data and the calibration model. On contrary, in order to assess of how well a calibration curve predicts the values of the unknown samples, cross validation technique would be used. Here, leave one out cross validation (LOOCV) method was used in this study. In this method, one data point is left out

59

to use as a test set while the remaining data points are used as training set to build the model (calibration curve) and then one evaluates the error of the model on the single-point that was being held out. This process is repeated for each data point from the training set for estimating the generalization error, which becomes the average results. This value can be used to measure on how well the model predicts the new data. Root mean square error of cross validation (RMSECV) was also used in this study to evaluate the calibration curve using the following formula [91, 93]:

$$\text{RMSECV} = \sqrt{\frac{\sum(x_{i,\text{LIBS}} - x_{i,\text{XRF}})^2}{n_s}} \tag{4.7}$$

where $x_{i,\text{LIBS}}$ is the concentration of the data point that was independently predicted by using LOOCV, $x_{i,\text{XRF}}$ is the actual concentration for that point obtained from XRF, and n_s is the number of cross validation points used. It is noteworthy that RMSEC has the same formula as the RMSECV except that the $x_{i,\text{XRF}}$ point was the concentration of the data point as predicted from the calibration curve.

4.5 Multivariate Calibration Methods

Since LIBS spectra have large and highly complex data sets that might be ignored by the calibration curve method, therefore, a multivariate analysis (MVA) was proposed and carried out. MVA is mathematical and statistical models that can be used for observation and analysis of multiple measurements. The entire spectra were used for analysis of the LIBS data with MVA, while one wavelength was selected for analysis with the calibration curve method. There are several tools used in multivariate analysis such as principal component analysis (PCA), partial least squares (PLS), discriminant functional analysis (DFA), artificial neural net-works (ANNs),

60

and linear discriminant analysis (LDA) [91]. Here, only two approaches were chosen to extract the information from the LIBS spectra; these are: (1) PCA as a descriptive model and (2) PLS as a predictive model.

PCA is a statistical technique that can be used to detect sample patterns, groupings, similarities, or differences, as well as to visualize interrelations between different variables [49]. In this method, the original variables (spectra) have been converted into a smaller number of uncorrelated underlying variables called principal components (PCs) using an orthogonal transformation. On the other hand, PLS is another statistical model used for building a calibration to predict unknown samples. The procedures of the algorithm for PCA and PLS were discussed below [91, 94-100].

PCA uses only a matrix X (n × m) of independent variables (spectra) to build and train a model that will be used to predict the concentration of n unknown samples. PLS, as an extension of PCA, uses two matrices X and Y (n × 1)—dependent variable (concentrations)—to also build and train that model. Here, both the X and Y data were decomposed into a score matrix and a loading matrix:

$$X = TP^T + E \tag{4.8}$$

and

$$Y = UQ^T + F \tag{4.9}$$

where T (m × *l*) is the X score matrix, U (n × *l*) is the Y score matrix, P (m × *l*) and Q (p × *l*) are the loading matrices of X and Y, respectively, E and F are matrices of residuals, n is the number of samples/repetitions (e.g., unknown samples) and m is the number of spectral data points. The predicted concentration $\widehat{Y}$ can be given by:

$$\widehat{Y} = TBQ^T = XB_{PLS} \tag{4.10}$$

with

$$B_{PLS} = P^{T+}BQ^T \tag{4.11}$$

where B is a diagonal matrix with the regression coefficients, B_{PLS} is a matrix that contains the regression weights, and P^{T+} is the Moore-Penrose pseudo-inverse of P^T. The algorithm for PLS regression is as follows:

(1) X and Y are mean-centered and normalized and stored in matrices X_0 and Y_0;

(2) The matrix of covariance (R_1) between X_0 and Y_0 is determined by:

$$R_1 = X_0^T Y_0 \tag{4.12}$$

(3) The next step is to produce singular orthogonal matrices W_1 and C_1 with a third matrix Δ_1 of corresponding values, the singular value decomposition (SVD) was achieved by

$$R_1 = W_1 \Delta_1 C_1^T \tag{4.13}$$

(4) The first latent variable of X is calculated by:

$$t_1 = X_0 w_1 \tag{4.14}$$

where t_1 is normalized such that $t_1^T t_1 = 1$.

(5) After that, the loadings of X_0 on t_1 and then the least squares estimate of X from the first latent variable are calculated by:

$$p_1 = X_0^T t_1 \tag{4.15}$$

$$\widehat{X}_1 = t_1^T p_1 \tag{4.16}$$

For Y matrix, the first latent variable is calculated as:

$$u_1 = Y_0 c_1 \tag{4.17}$$

(6) The PLS method predicts $\widehat{Y}_1$ by regression on u is generated:

62

$$\widehat{Y}_1 = u_1 c_1^T = t_1 b_1 C_1^T \tag{4.18}$$

with

$$b_1 = t_1^T u_1 \tag{4.19}$$

where b_1 is the slope of the regression of $\widehat{Y}_1$ on t_1.

(7) Finally, the second factor is calculated in the same way by replacing the original X_0 and original Y_0 with the X- and Y-residuals (deflated X_1 and Y_1) from the first factor as following:

$$X_1 = X_0 + \widehat{X}_1 \tag{4.20}$$

and

$$Y_1 = Y_0 + \widehat{Y}_1 \tag{4.21}$$

The procedure of extracting a score vector and deflating the data matrices is repeated until X is totally decomposed resulting in a diagonal matrix B_{PLS} with the regression coefficients. To detect the relationship between samples through PCA, the principal components calculated using Equation 4.14 were plotted versus each other. The optimal number of principal components to explain samples can be found by plotting the percent of variance explained in *X* as a function of the number of components. In PLS method, Equation 4.10 can be used to predict the concentration from the X matrix.

To assess of how well PLS model predicts the values of the unknown samples, cross validation technique was applied. For example, for a calibration curve method, LOOCV was applied again in this section, as well as, RMSECV was calculated. The number of latent variables (LV) in the PLS model was very important because by selecting more LV would lead to over-fit the model while on the other hand selecting few LV could generate an under-fitted model [101].

63

Therefore, the best number of latent variables (LV) was selected based on the lowest RMSECV value obtained by applying the test data set.

4.6 Results and Discussion

4.6.1 Optimal conditions for LIBS analysis

To improve the detection limit of Ce and Cs elements in LIBS, several experimental parameters that might affect the system were studied. That is, laser energy, gate delay (time between the firing of the laser pulse and the opening of the camera shutter), and gate width (time for which the shutter is open) were being explored [52, 102-108]. These parameters were optimized before using LIBS on actual cement samples. Several experiments were conducted to obtain the optimal conditions of laser energy, gate delay, and gate width for the analysis of RSC samples. The optimization study was achieved using the signal-to-background ratio (SBR) for the Ce as a function of laser energy, while intensity as a function of gate delay and gate width. Three repetitions of 100 shots were done, then averaged in order to provide a representative spectrum for different explored conditions. Figure 4.7 shows the SBR of three Ce lines as a function of the laser pulse energy. The results reveal a high SBR for Ce lines at laser pulse energy of 30 ± 3 mJ. On the other hand, the intensity of same three Ce lines as function of the gate delay is shown in Figure 4.8. Here, the result indicates that the intensity increases up to about 6 µs and then drops off. Figure 4.9 shows the comparison between the different gate width values. The intensities of the three Ce lines decrease as the gate width increases. It was concluded that the optimum conditions for recording the Ce signal were laser pulse energy of 30 mJ at the gate delay and gate width of 6 µs and 1.05 µs, respectively.

64
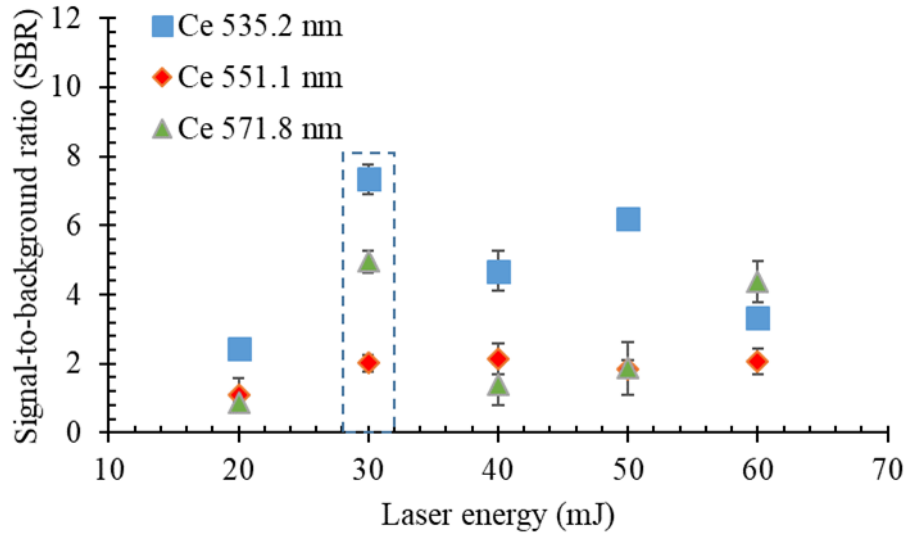
Figure 4. 7 SBR of the three Ce lines as a function of the laser pulse energy.
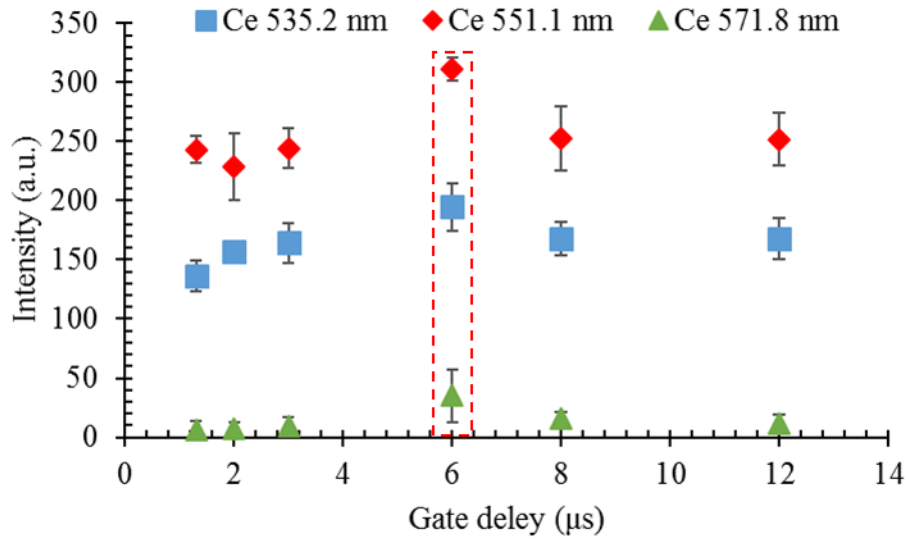
Figure 4. 8 SBR of the three Ce lines as a function of the gate delay.

65
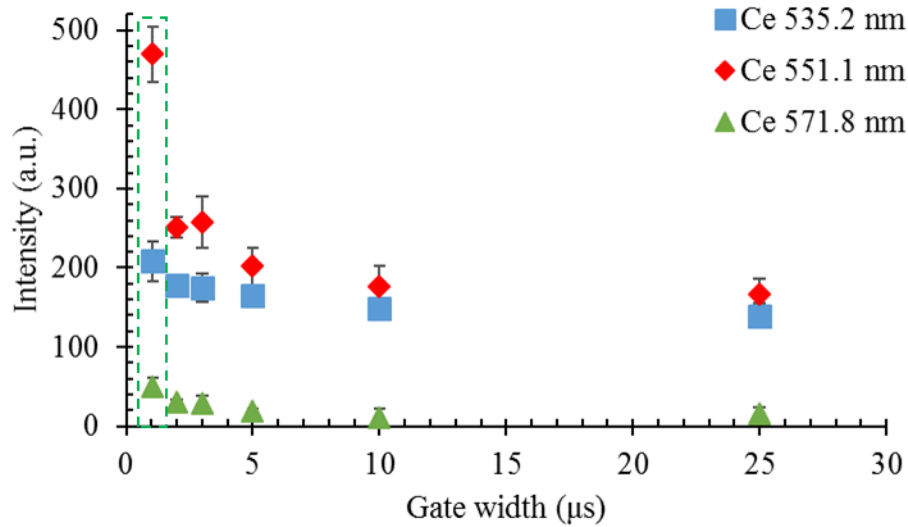
Figure 4. 9 SBR of the three Ce lines as a function of the gate width.

4.6.2 Comparison between prepared concentration and measured concentration from XRF and LIBS

The XRF results for the Ce and Cs concentrations for the 20 samples with DIW and 20 samples with ASW are shown in Table 4.3 and 4.4. Each sample was measure three times in the XRF analysis and the average was taken. The measured concentrations of Ce and Cs elements were compared with the prepared concentrations. The percent differences on average for samples with DIW were $5.7 \pm 2.4\%$ for Ce and $5.8 \pm 2.7\%$ for Cs while samples mixed with ASW appeared to be $4.2 \pm 1.6\%$ for Ce and $5.5 \pm 2.3\%$ for Cs. The difference between prepared and measured results, may be due to, the fact that some contents of cement and Ce and Cs were sticking to the impeller during mixing (considered as lost contents). The main drawback of the LIBS technique that can affect measurement accuracy is laser-shot-to-shot variation. However, the effect of plasma fluctuation over the measurement can be eliminated by normalization the data sets. Therefore, the peak intensity of the Ce line was divided by the Si average peak intensity which is the major element in the cement and assumed to have constant concentration throughout. Therefore, it could

66

be used as internal standards to give an adequate approximation. The strongest Si lines in the spectrum were the 589.8 nm and 518.2 nm peaks. The Si 589.8 nm line was showed self-absorption, so it was inappropriate for normalization. As a result, the Si 518.2 nm line was used to normalize the spectrum.

Table 4. 3 Ce and Cs concentrations of all 20 samples with DIW as prepared and measured using XRF with calculated % differences between the prepared and measured concentrations.

	Prepared		XRF		Prepared versus XRF	
Sample	**Cs (wt%)**	**Ce (wt%)**	**Cs (wt%)**	**Ce (wt%)**	**Cs % difference**	**Ce % difference**
1	0.5	0.5	0.464	0.466	7.47	7.04
2	0.5	1	0.478	0.986	4.45	1.41
3	0.5	2	0.452	1.830	10.08	8.88
4	0.5	4	0.468	3.786	6.61	5.5
5	0.5	8	0.450	7.118	10.53	11.67
6	1	0.5	0.972	0.474	2.84	5.34
7	1	1	0.972	0.966	2.84	3.45
8	1	2	0.972	1.886	2.84	5.86
9	1	4	0.98	3.816	2.02	4.71
10	1	8	0.966	7.642	3.46	4.58
11	2	0.5	1.782	0.476	11.53	4.92
12	2	1	1.838	0.976	8.44	2.43
13	2	2	1.918	1.88	4.18	6.19
14	2	4	1.892	3.83	5.55	4.34
15	2	8	1.892	7.576	5.55	5.44
16	4	0.5	3.8	0.47	5.13	6.19
17	4	1	3.828	0.948	4.4	5.34
18	4	2	3.738	1.796	6.78	10.75
19	4	4	3.788	3.786	5.44	5.5
20	4	8	3.742	7.614	6.66	4.94

67

Table 4. 4 Ce and Cs concentrations of all 20 samples with ASW as prepared and measured using XRF with calculated % differences between the prepared and measured concentrations.

Sample	Prepared		XRF		Prepared versus XRF	
	Cs (wt%)	Ce (wt%)	Cs (wt%)	Ce (wt%)	Cs % difference	Ce % difference
1	0.5	0.5	0.462	0.486	7.9	2.84
2	0.5	1	0.468	0.968	6.61	3.25
3	0.5	2	0.452	1.848	10.08	7.9
4	0.5	4	0.456	3.794	9.21	5.29
5	0.5	8	0.47	7.708	6.19	3.72
6	1	0.5	0.962	0.48	3.87	4.08
7	1	1	0.96	0.966	4.08	3.46
8	1	2	0.968	1.892	3.25	5.55
9	1	4	0.974	3.812	2.63	4.81
10	1	8	0.974	7.802	2.63	2.51
11	2	0.5	1.908	0.486	4.71	2.84
12	2	1	1.86	0.978	7.25	2.22
13	2	2	1.814	1.868	9.75	6.83
14	2	4	1.884	3.748	5.97	6.5
15	2	8	1.908	7.708	4.71	3.72
16	4	0.5	3.792	0.47	5.34	6.19
17	4	1	3.858	0.976	3.61	2.43
18	4	2	3.868	1.926	3.36	3.77
19	4	4	3.828	3.87	4.4	3.3
20	4	8	3.828	7.702	4.4	3.8

Figures 4.10a and 4.10b show the %RSD values (1–20%) and intensity variation of the repetitions of the samples selected (4, 9, 14, and 19) before normalization. Also, Figures 4.10c and 4.10d show the %RSD values and intensity variation of the repetitions after normalization. The %RSD values averaged after the normalization were averaged between 0.7% and 10% with a maximum reaching up to 20%. The difference in the spectra after normalization can be attributed

to homogeneity effects, fluctuation in the laser energy, and local concentration effects as a result of possible fractional crystallization [109].
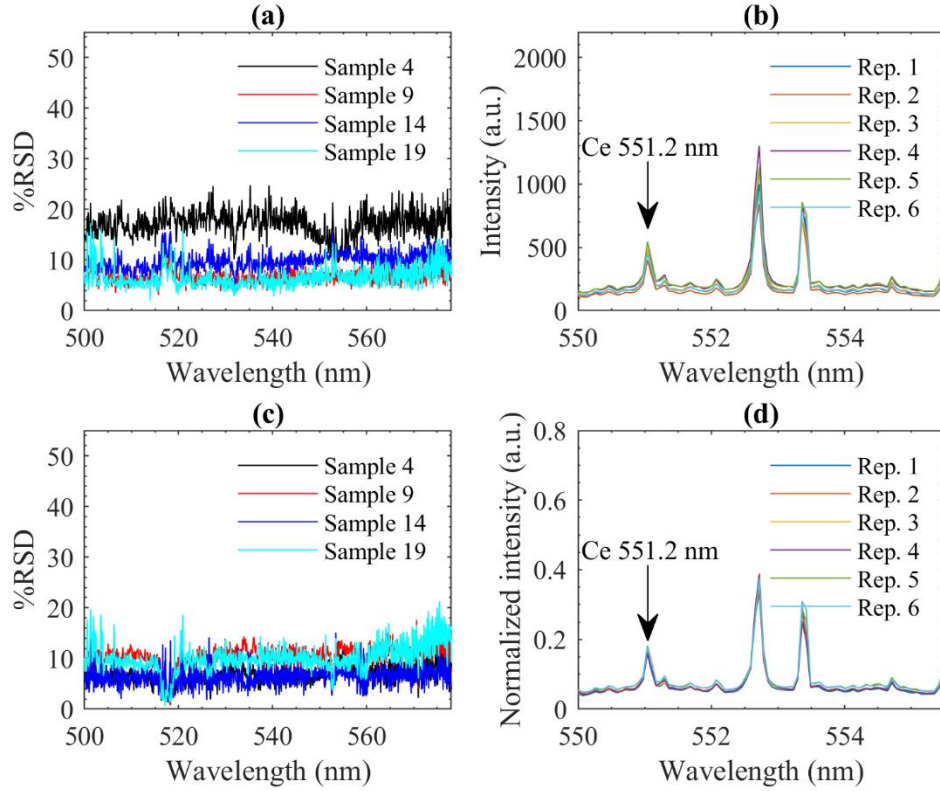
Figure 4. 10 (a) The %RSD values from 550 nm to 575 nm before normalization, (b) an example (sample 14) of the intensity difference previous to normalization, (c) the %RSD values after normalization, and (d) the intensity difference of sample 14 after normalization.

Figure 4.11 displays the LIBS spectrum obtained from sample 20 (high Ce and high Cs) in the spectral region of 300 to 950 nm. All atomic spectral lines were determined using the National Institute of Standards and Technology (NIST) database in the Applied Spectra data analysis software (Aurora). The largest visible peaks are due to (Si and K) and are present in all samples. The next largest peaks are attributed to (Na and Mg) and can also be found in all samples. There are many other peaks that are common to all samples and are most likely the components of the cement. Several peaks can be attributed to the following elements: Ca, and Fe. Also, there are

69

many visible peaks for Ce and Cs in areas of interest. Table 4.5 shows the Ce and Cs lines that have been selected for LIBS analysis. These lines were chosen based on the low spectral interferences with other peaks. Three parameters (the relative intensity (RI), signal-to-background (S/B) ratio, and the signal-to-noise (S/N) ratio) were also evaluated to select the best lines for each element. These quantities are calculated using equations below [91]. The best three lines for Ce and Cs were (535.2, 551.1, and 571.8) and (697.1, 851.9, and 894.4), respectively.

$$SBR = \frac{\text{Peak intensity}}{\text{Background intensity near the peak}} \qquad (4.22)$$

$$SNR = \frac{\text{Peak area}}{\text{RMS noise} \times \text{Peak width}} \qquad (4.23)$$
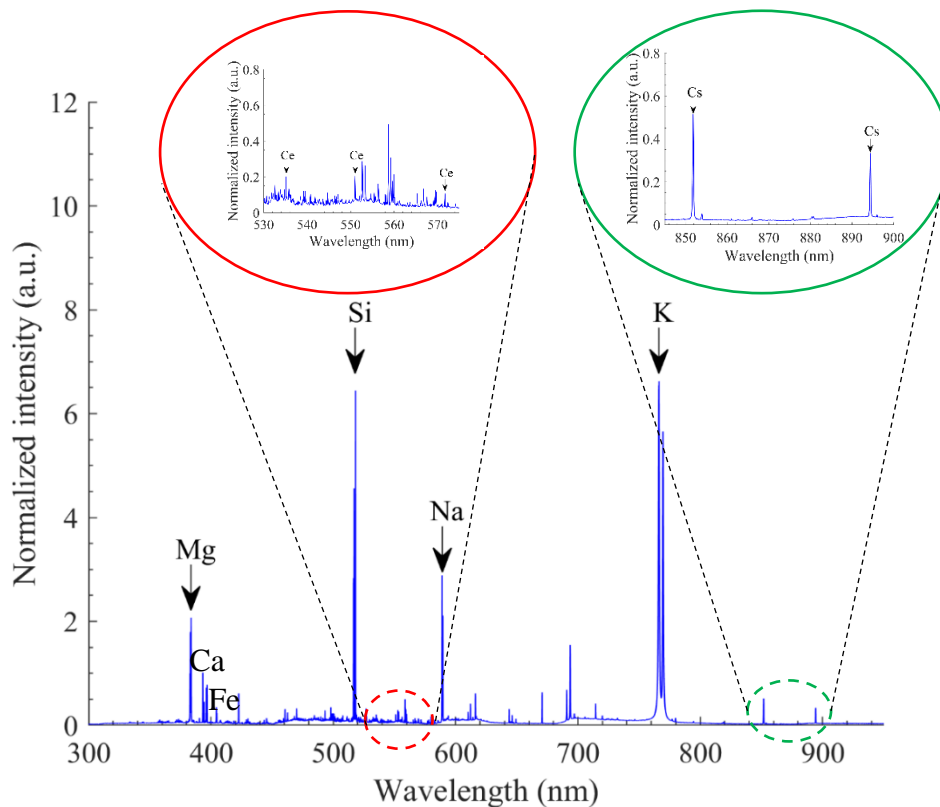
Figure 4. 11 The average normalized spectra from the six repetitions obtained from sample 20 with high concentrations of Ce and Cs.

Table 4. 5 Elemental lines for Ce and Cs selected for LIBS analysis based on evaluate three parameters which are RI, S/B, and S/N. Note: Blue = selected line

Ce Lines (nm)	RI	SBR	SNR	Cs Lines (nm)	RI	SBR	SNR
507.8	0.76	2.12	1.29	672.2	0.08	1.67	0.97
535.2	0.85	2.81	1.31	697.1	0.36	2.66	1.06
540.8	0.54	2.44	1.04	851.9	1.00	17.78	1.20
551.1	1	2.79	1.34	894.4	0.68	10.88	1.35
556.4	0.76	2.33	1.39	917.2	0.09	1.81	0.93
565.4	0.52	3.21	1.17				
566.8	0.6	2.83	1.41				
571.8	0.5	3.32	1.52				
577.2	0.4	2.85	1.26				

4.6.3 Calibration curves for selected Ce and Cs lines

The selected peaks were used to build calibration curves using both the peak areas and the peak intensities methods. The peak intensity is the maximum intensity while the peak area is the area under the curve minus the background as shown in Figure 4.12. To evaluate these spectral values, a graphical user interface (GUI) function was written in MATLAB. Figures 4.13 and 4.14 show the calibration curves formed from the Ce 571.8 nm line in samples mixed with DIW and that mixed with ASW using the peak intensities and peak areas, respectively. Results reveal that the data set in the peak area curve is more linear with respect to the Ce concentration than that made using the peak intensity curve. Tables 4.6 and 4.7 show the regression coefficients and the figures of merit for all of the Ce curves generated from using samples mixed with DIW and that mixed with ASW, respectively. The calibration curves are linear with regression coefficients between 0. 927 and 0.980 for Ce in samples with DIW while 0.897 and 0.982 in samples with ASW. The lowest and highest values of LOD were obtained between 0.088 wt% and 0.126 wt% for Ce in DIW system and 0.091 wt% and 0.111 wt% for Ce in ASW.

71
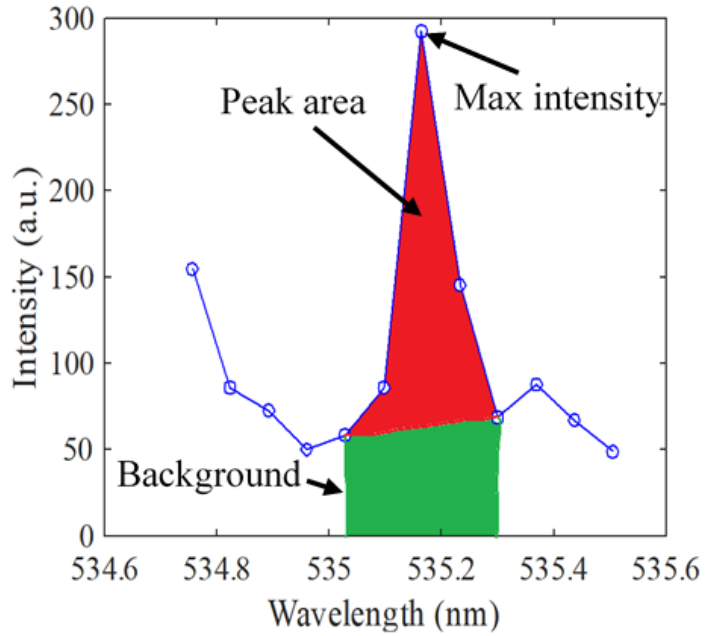
Figure 4. 12 Peak area and max peak intensity analysis.
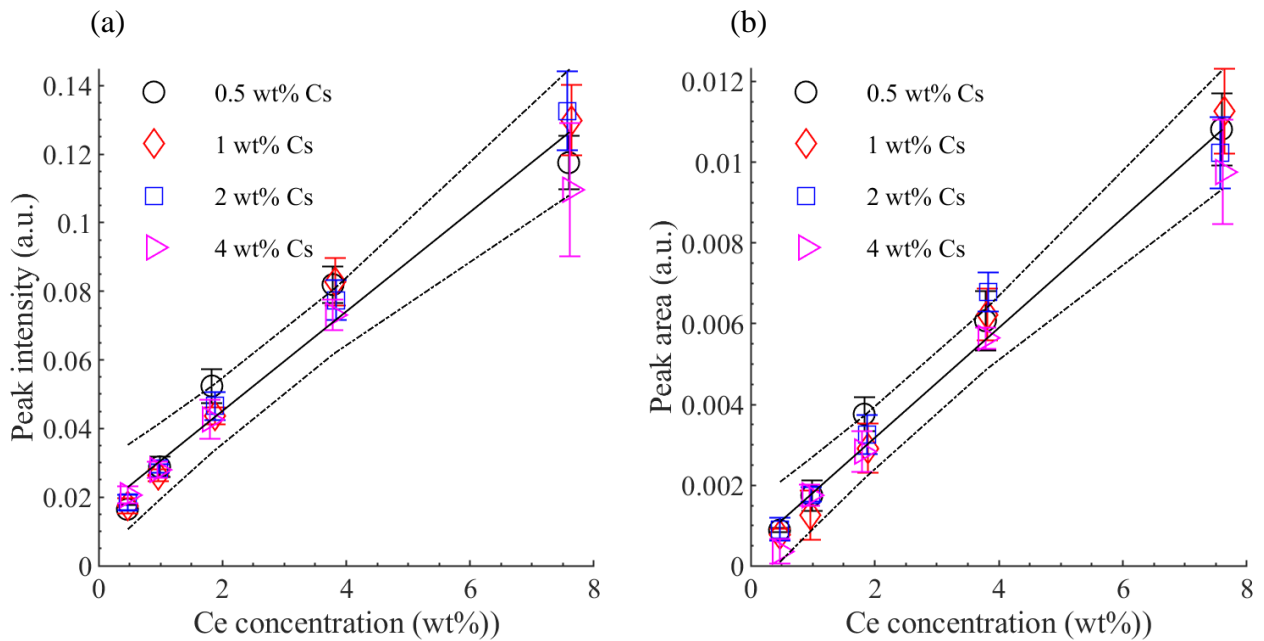
Figure 4. 13 Univariate calibration curves made from the Ce 571.8 nm line in samples mixed with DIW using (a) the peak intensity and (b) the peak area.

72
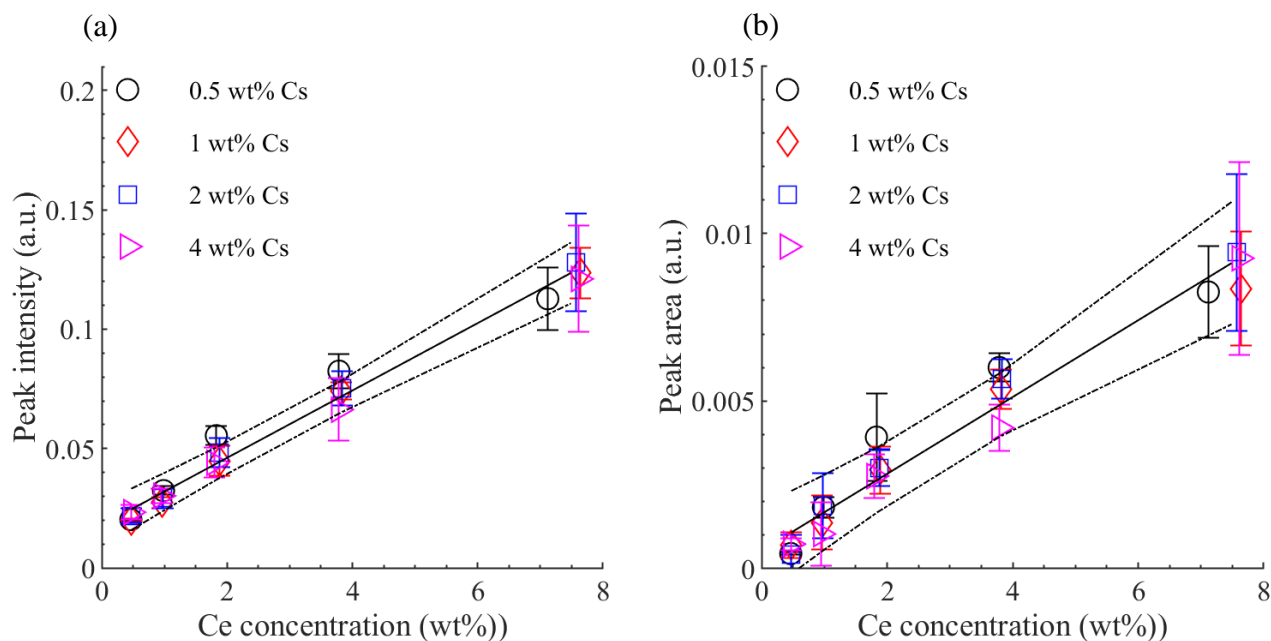
Figure 4. 14 Univariate calibration curves made from the Ce 571.8 nm line in samples mixed with ASW using (a) the peak intensity and (b) the peak area.

Table 4. 6 Regression coefficients and figures of merits for the univariate calibration curves for the Ce in samples mixed with DIW.

	Ce 535.2 nm		Ce 551.1 nm		Ce 571.8 nm	
	Area	Intensity	Area	Intensity	Area	Intensity
m	0.0018	0.0252	0.0018	0.0189	0.0014	0.0145
b	0.0003	0.0284	0.0021	0.0739	0.0004	0.0160
RMSE	0.0011	0.0109	0.0014	0.0137	0.0005	0.0072
R²	0.954	0.975	0.927	0.934	0.980	0.968
LOD (wt %)	0.126	0.195	0.154	0.207	0.088	0.177
RMSEC (wt %)	0.573	0.4115	0.730	0.690	0.371	0.469
RMSECV (wt %)	0.639	0.464	0.812	0.791	0.419	0.536

73

Table 4. 7 Regression coefficients and figures of merits for the univariate calibration curves for the Ce in samples mixed with ASW.

	Ce 535.2 nm		Ce 551.1 nm		Ce 571.8 nm	
	Area	Intensity	Area	Intensity	Area	Intensity
m	0.0014	0.0224	0.0016	0.0131	0.0141	0.0011
b	0.0002	0.0316	0.0029	0.0733	0.0179	0.0005
RMSE	0.0013	0.0097	0.0007	0.0061	0.0050	0.0006
R^2	0.897	0.975	0.977	0.971	0.982	0.960
LOD (wt %)	0.349	0.153	0.388	0.338	0.091	0.111
RMSEC (wt %)	0.868	0.409	0.389	0.444	0.338	0.517
RMSECV (wt %)	0.999	0.461	0.446	0.505	0.370	0.569

The total deviation of the response values (peak intensity and peak area) from the fit to the response values was investigated by calculating the statistical measure of the RMSE for Ce lines. The RMSE values for Ce lines in samples with DIW and with ASW were in a range of 0.0005 – 0.0137 and 0.0006 – 0.0097, respectively. The RMSEC was calculated for estimating the goodness of fit between actual concentration and the calibration model. The RMSEC for Ce lines in samples with DIW and with ASW were in a region of (0.371 wt% – 0.730 wt%) and (0.338 wt% – 0.868 wt%), respectively. The results of the cross-validation were reported as the RMSECV, which were in a range of 0.419 wt% - 0.812 wt% and 0.370 wt% - 0.999 wt% for Ce lines in samples with DIW and with ASW, respectively. As a result, between the three selected Ce lines in samples with DIW and with ASW, the 571.8 nm calibration curve made using the peak area had the lowest LOD, RMSE, RMSEC, and RMSECV, and the highest R^2. Therefore, it was recommended for Ce measurements in cement waste matrix. Figures 4.15 and 4.16 show the predicted LIBS sample concentrations created using the peak intensity and peak areas of the Ce 571.8 nm line versus the

74

measured XRF concentrations from both samples with DIW and with ASW. It was observed that Ce spiked with cement samples with DIW displayed good correlation between predicted and measured values with R^2 of 0.975 using peak area and 0.959 using peak intensity. Likewise, Ce spiked with cement samples with ASW revealed more scatter in the data with an overall good agreement between predicted and measured values with R^2 of 0.970 using peak area and 0.962 using peak intensity.

The calibration curves created from the Cs 697.1 nm line, in samples mixed with DIW, using the peak intensities and peak areas are shown in Figure 4.17. It can be seen that the data in the peak area curve have a strong linear trend with respect to the Cs concentration than that made using the peak intensity curve. The regression coefficients and the figures of merit for all of the Cs curves generated from using samples mixed with DIW are summarized in Table 4.8. It was observed that between the three selected Cs lines in samples with DIW, the 697.1 nm calibration curve created using the peak area had the lowest LOD (0.068 wt%), RMSE (0.0017), RMSEC (0.218 wt%), and RMSECV (0.246 wt%), and the highest R^2 (0.971).

Figure 4.18 shows the calibration curves created from the Cs 851.9 nm line, in samples mixed with ASW, using the peak intensities and peak areas. Similarly, the data in the peak area curve has a better linear trend with respect to the Cs concentration than that made using the peak intensity curve. The regression coefficients and the figures of merit for all of the Cs curves formed from using samples mixed with ASW were listed in Table 4.9. It can be seen that the Cs 851.9 nm calibration curve created using the peak area was the best among the three selected Cs lines, displaying the lowest LOD (0.042 wt%), RMSEC (0.222 wt%), and RMSECV (0.249 wt%), and the highest R^2 (0.970). Therefore, the 697.1 nm and 851.9 nm calibration curves were

recommended for Cs measurements in cement waste matrix with DIW and with ASW, respectively.
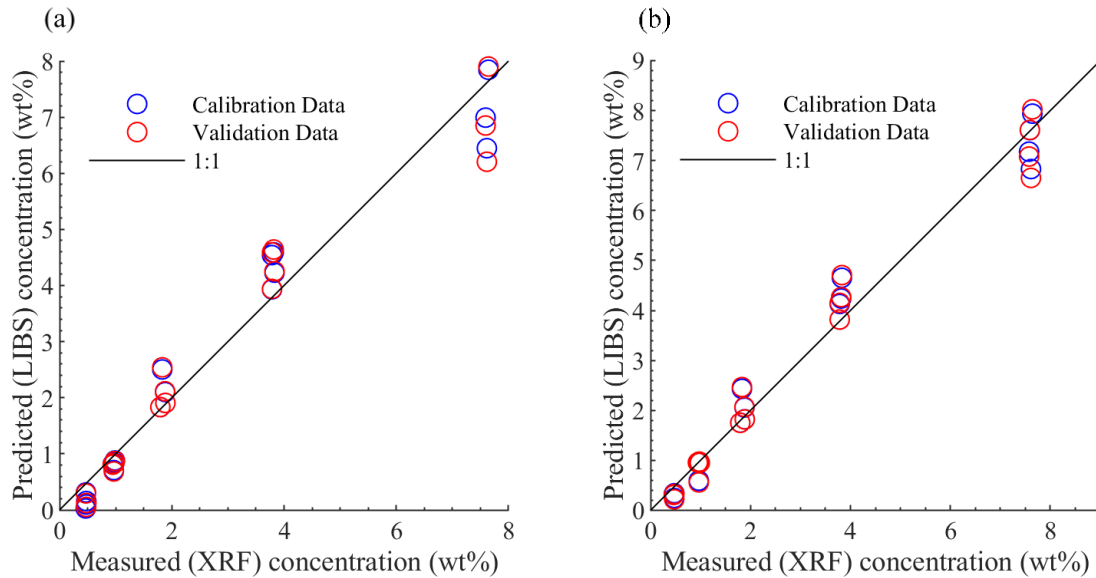
Figure 4. 15 (a) Predicted Ce concentration in samples mixed with DIW from the peak intensities of the Ce 571.8 nm line and (b) the predicted Ce concentration in samples mixed with DIW from the peak areas of the Ce 571.8 nm line.
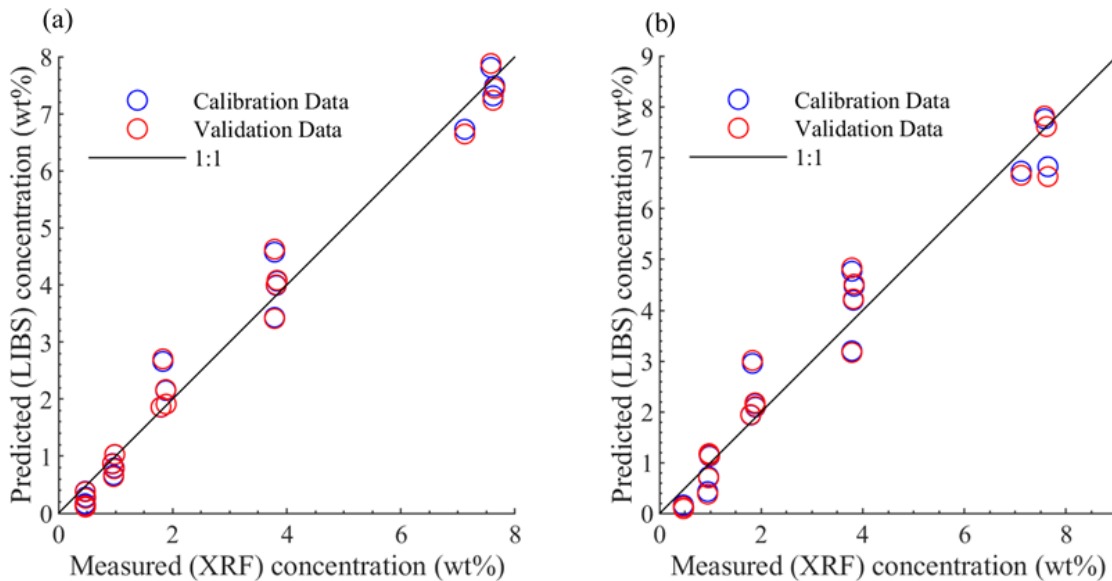
Figure 4. 16 (a) Predicted Ce concentration in samples mixed with ASW from the peak intensities of the Ce 571.8 nm line and (b) the predicted Ce concentration in samples mixed with ASW from the peak areas of the Ce 571.8 nm line.

76
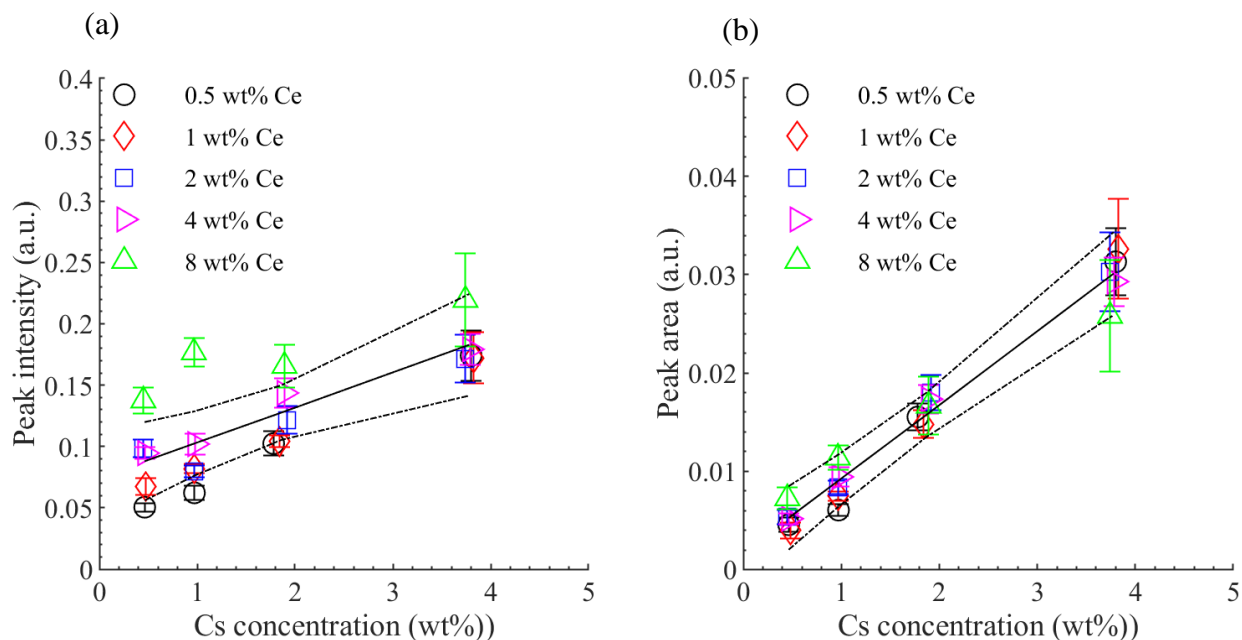
Figure 4. 17 Univariate calibration curves made from the Cs 697.1 nm line in samples mixed with DIW using (a) the peak intensity and (b) the peak area.

Table 4. 8 Regression coefficients and figures of merits for the univariate calibration curves for the Cs in samples mixed with DIW.

	Cs 697.1 nm		Cs 851.9 nm		Cs 894.4 nm	
	Area	Intensity	Area	Intensity	Area	Intensity
m	0.0075	0.0287	0.0210	0.0630	0.0118	0.0473
b	0.0018	0.0685	0.0453	0.2234	0.0231	0.1386
RMSE	0.0017	0.0119	0.0090	0.034	0.0042	0.0223
R^2	0.971	0.912	0.910	0.860	0.933	0.890
LOD (wt %)	0.068	0.184	0.510	0.666	0.360	0.542
RMSEC (wt %)	0.218	0.392	0.402	0.518	0.338	0.448
RMSECV (wt %)	0.246	0.429	0.440	0.566	0.377	0.489

77
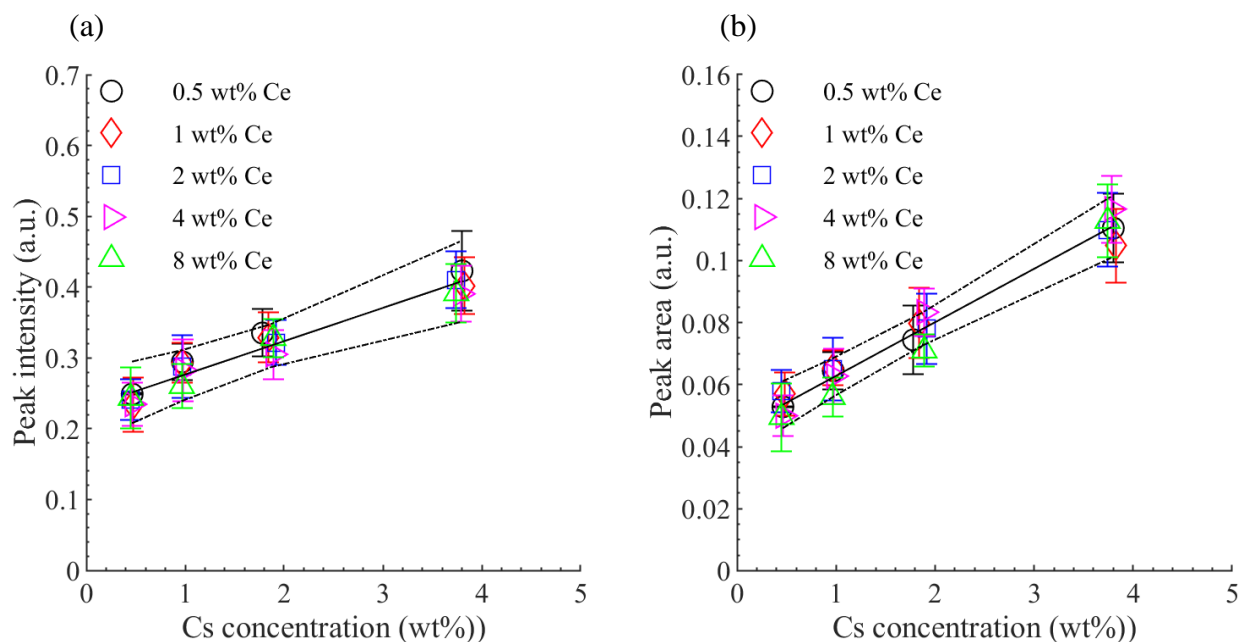
Figure 4. 18 Univariate calibration curves made from the Cs 851.9 nm line in samples mixed with DIW using (a) the peak intensity and (b) the peak area.

Table 4. 9 Regression coefficients and figures of merits for the univariate calibration curves for the Cs in samples mixed with ASW.

	Cs 697.1 nm		Cs 851.9 nm		Cs 894.4 nm	
	Area	Intensity	Area	Intensity	Area	Intensity
m	0.0077	0.0247	0.0172	0.0470	0.0104	0.0374
b	0.0012	0.0644	0.0455	0.2296	0.0232	0.1428
RMSE	0.0023	0.0089	0.0040	0.0141	0.0035	0.0178
R^2	0.952	0.932	0.970	0.952	0.938	0.886
LOD (wt %)	0.412	0.288	0.042	0.074	0.290	0.465
RMSEC (wt %)	0.284	0.343	0.222	0.285	0.324	0.454
RMSECV (wt %)	0.332	0.379	0.249	0.316	0.366	0.510

78

Figure 4.19 and 4.20 show the predicted LIBS sample concentrations created using the peak intensity and peak areas of the Cs 697.1 nm line and the Cs 851.9 nm line versus the measured XRF concentrations from both samples with DIW and with ASW, respectively. It can be seen that the data sets created using the peak intensity were poorly predicted with R^2 of 0.897. However, the predicted Cs concentrations from samples with DIW using the peak areas and those from samples with ASW using the peak intensity and peak areas show an overall good correlation between predicted and measured values with R^2 of 0.964, 0.918, and 0.936, respectively.
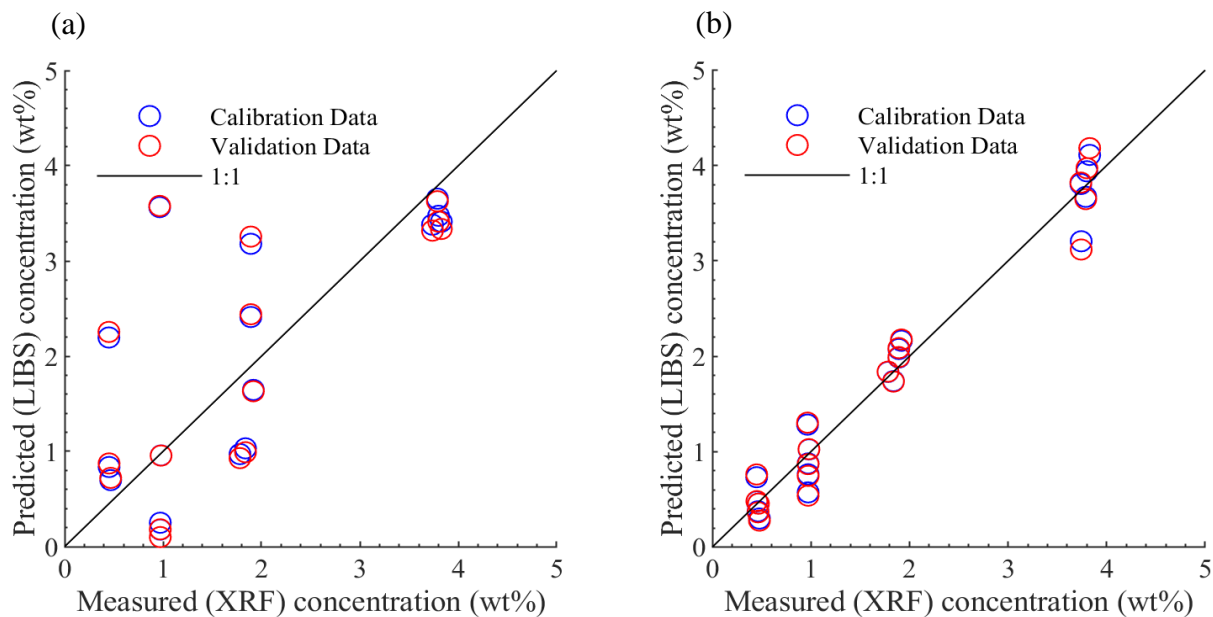
Figure 4. 19 (a) Predicted Cs concentration in samples mixed with DIW from the peak intensities of the Cs 697.1 nm line and (b) the predicted Cs concentration in samples mixed with DIW from the peak areas of the Cs 697.1 nm line.
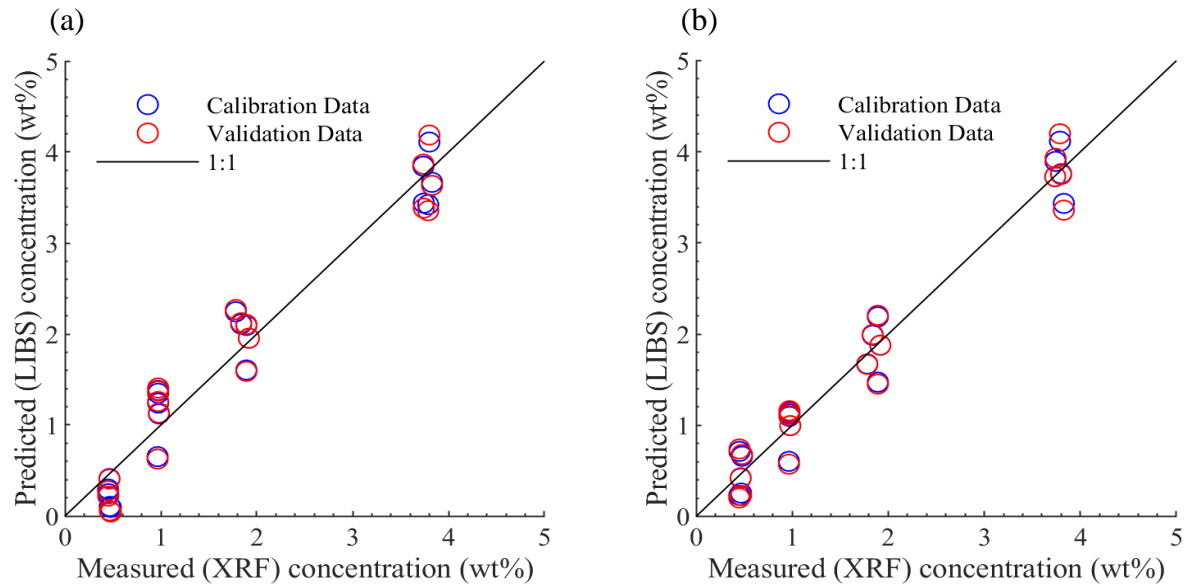
Figure 4. 20 (a) Predicted Cs concentration in samples mixed with ASW from the peak intensities of the Cs 851.9 nm line and (b) the predicted Cs concentration in samples mixed with ASW from the peak areas of the Cs 851.9 nm line.

4.6.4 PCA and PLS for Ce and Cs content with LIBS

Multivariate analysis was done on the whole spectra using PCA and PLS. The commercial software MATLAB was created for the PCA and PLS modeling. The result from a PCA analysis is typically displayed in a score plot. The score plot involves the projection of the data onto the PCs in two dimensions. There is one score value for each sample (row) in the data set; so, there are N score values for the first component, another N for the second component, and so on. Figures 4.21 and 4.22 for Ce-cement samples mixed with DIW and those with ASW, respectively, show the cumulative explained variance as a function of the number of components which describe how explained variance of an individual variable evolves with the number of components in the model. According to those Figures, two components would be enough to obtain the model with the good results. The score plots for Ce-cement samples mixed with DIW and those with ASW shown in Figures 4.23 and 4.24, respectively, use the first two PCs on the entire spectra. The first two

80

principal components for Ce samples mixed with DIW accounted for 59.5% (PC1) and 26% (PC2) while for those with ASW accounted for 72.0% (PC1) and 19.4% (PC2) of the total spectral variation. The results of PCA show five clusters for all spectra. This indicates that there is difference between these samples of the data in terms of chemical concentration or elemental composition. This strongly suggests that Ce is detected in these data sets. Also, it shows that the majority of the sample sets are most likely homogeneous.
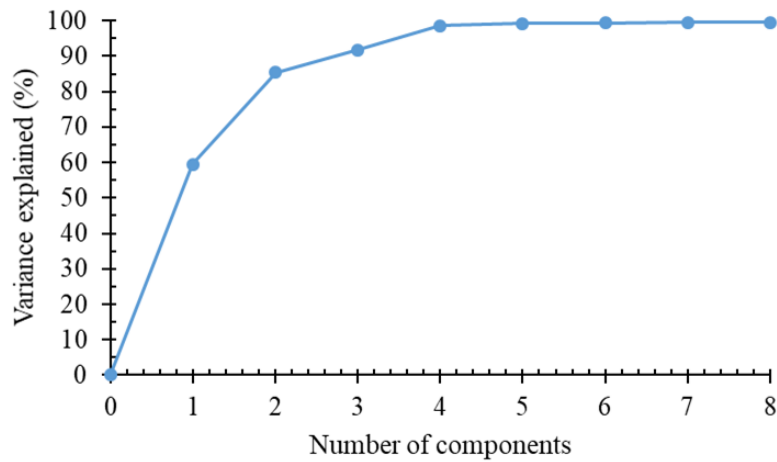
Figure 4. 21 Explained variance plot in PCA model for different Ce contents in samples mixed with DIW.
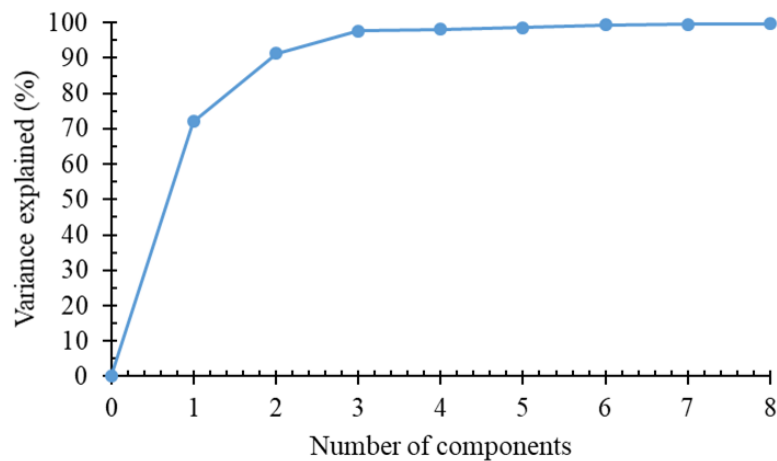
Figure 4. 22 Explained variance plot in PCA model for different Ce contents in samples mixed with ASW.

81
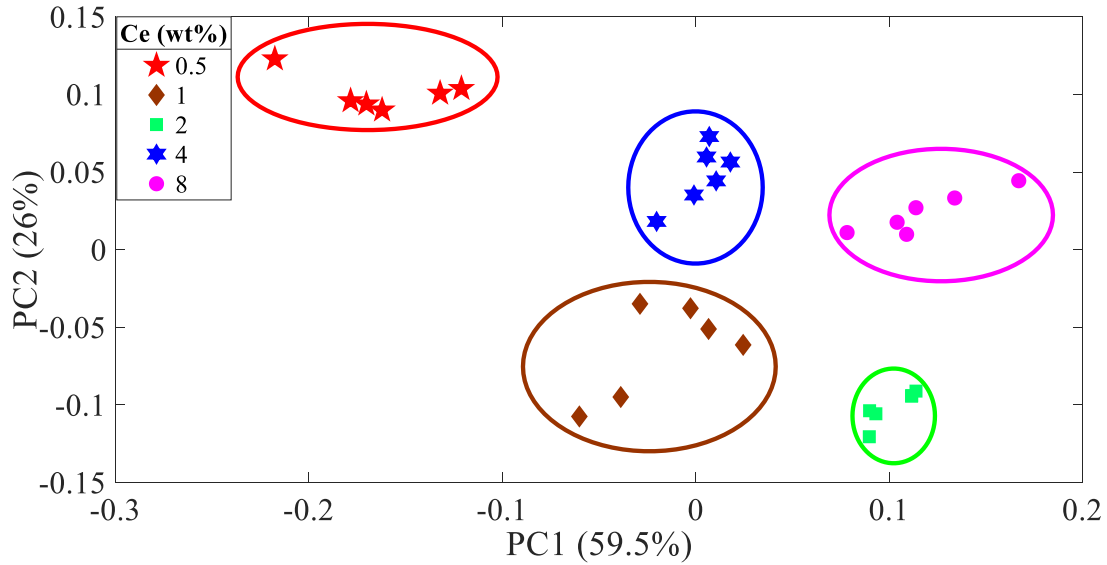
Figure 4. 23 PCA score plot for different Ce contents in samples mixed with DIW.
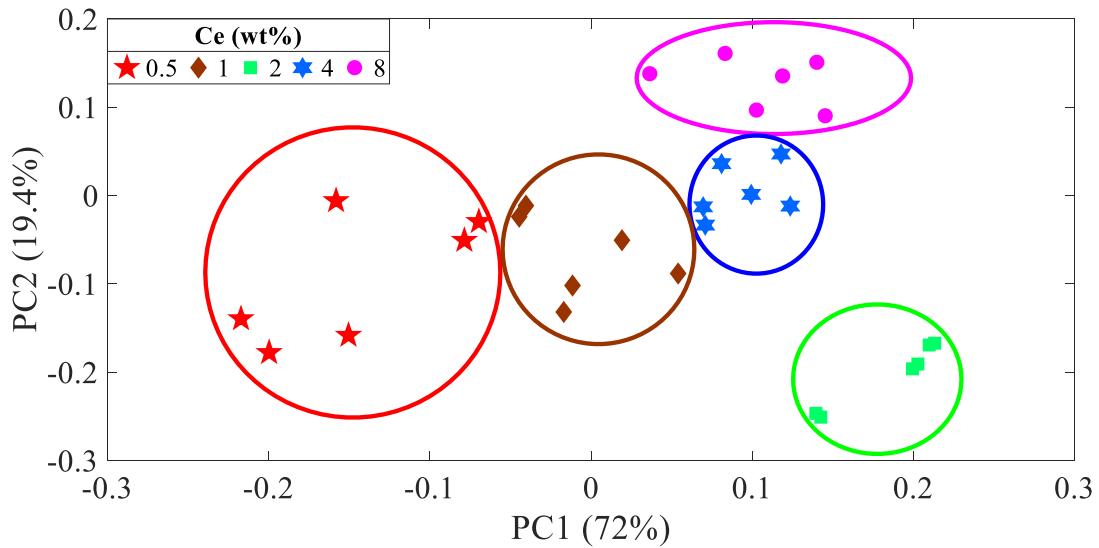
Figure 4. 24 PCA score plot for different Ce contents in samples mixed with ASW.

Same results were obtained when the Cs spiked with samples mixed with either DIW or ASW were analyzed (see Figures 4.25 to 4.28). The first two principal components for Cs samples mixed with DIW accounted for 64.5% (PC1) and 12.0% (PC2) while for those with ASW accounted for 75.7% (PC1) and 13.7% (PC2) of the total spectral variation. The results of PCA

show four clusters for all spectra. The reason of the separation between these four clusters is most

likely due to the addition of Cs with different concentration with constant Ce concentration. So, it

is probable that the added Ce and Cs has been immobilized within the cement.
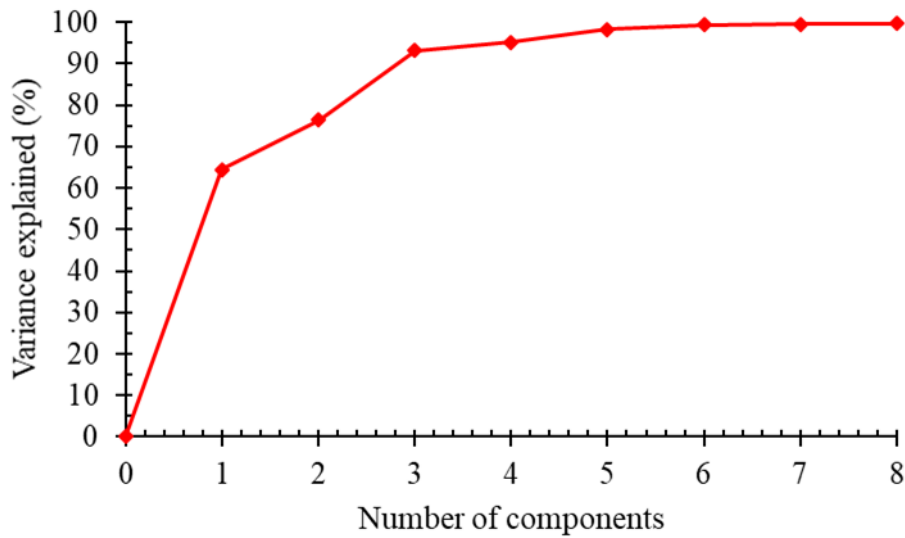
Figure 4. 25 Explained variance plot in PCA model for different Cs contents in samples mixed with DIW.
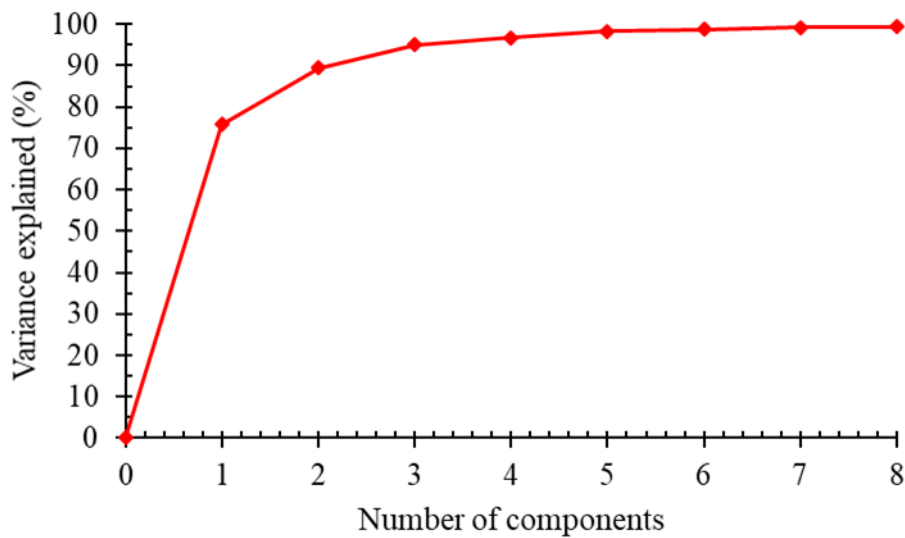
Figure 4. 26 Explained variance plot in PCA model for different Cs contents in samples mixed with ASW.

83
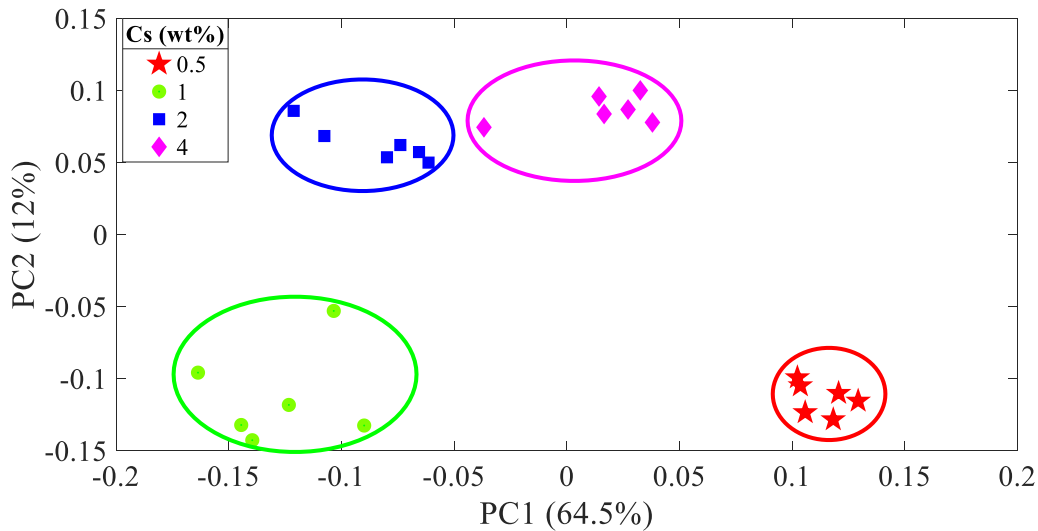
Figure 4. 27 PCA score plot for different Cs contents in samples mixed with DIW.
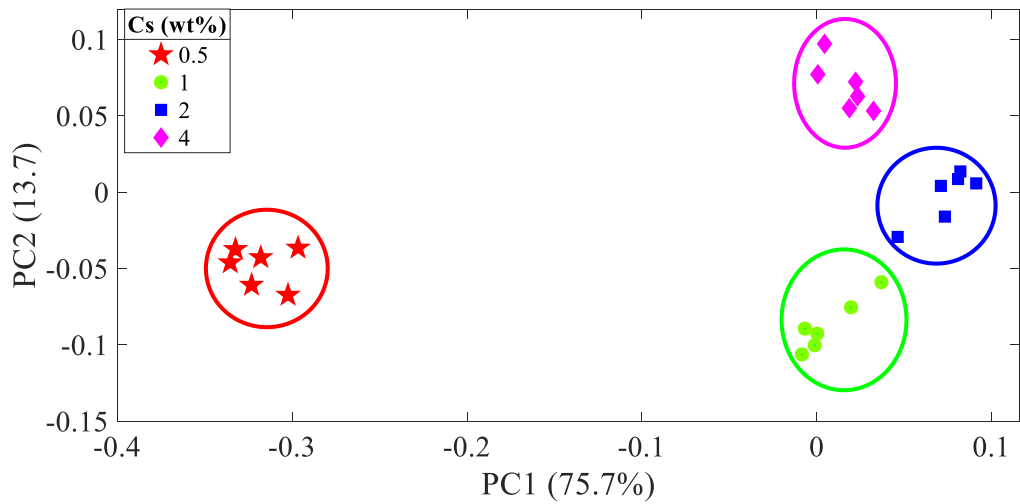
Figure 4. 28 PCA score plot for different Cs contents in samples mixed with ASW.

Next multivariate analysis used to generate a multivariate calibration model for the samples was PLS. The whole spectrum was used in modeling after taking the average spectrum for each sample. The RMSECV was calculated using a LOOCV, the same cross validation that was applied for the calibration curves. Figures 4.29a and 4.30a describe the relationship of the RMSECV and the RMSEC for the Ce model in samples mixed with DIW and those with ASW, respectively, as a function of the latent variables. Those figures show that seven and eight factors are best to obtain a calibration model with the optimum predictability. The PLS calibration curves for Ce in samples

84

mixed with DIW and those with ASW are shown in Figures 4.29b and 4.30b, respectively. It can be seen that there is a variation in the data at a high concentration for Ce in samples mixed with DIW, while more variation for Ce in samples mixed with ASW. Table 4.10 shows the quality parameters determined for PLS models. The RMSECV for samples mixed with DIW and that with ASW were 0.59 wt% Ce and 0.57 wt% Ce, which are larger than the calibration curve case. Additionally, PLS models also had good correlation coefficients of 0.95. Different results were obtained when the Cs spiked with samples mixed with either DIW or ASW were analyzed (see Figures 4.31 and 4.32). Ten and eight factors were need to obtain a best calibration model, with R^2 of 0.93 and 0.89, and RMSECV of 0.34 and 0.43 wt%, for samples mixed with DIW and that with ASW, respectively. Overall, the results are good when compared with the Cs univariate calibration curves.
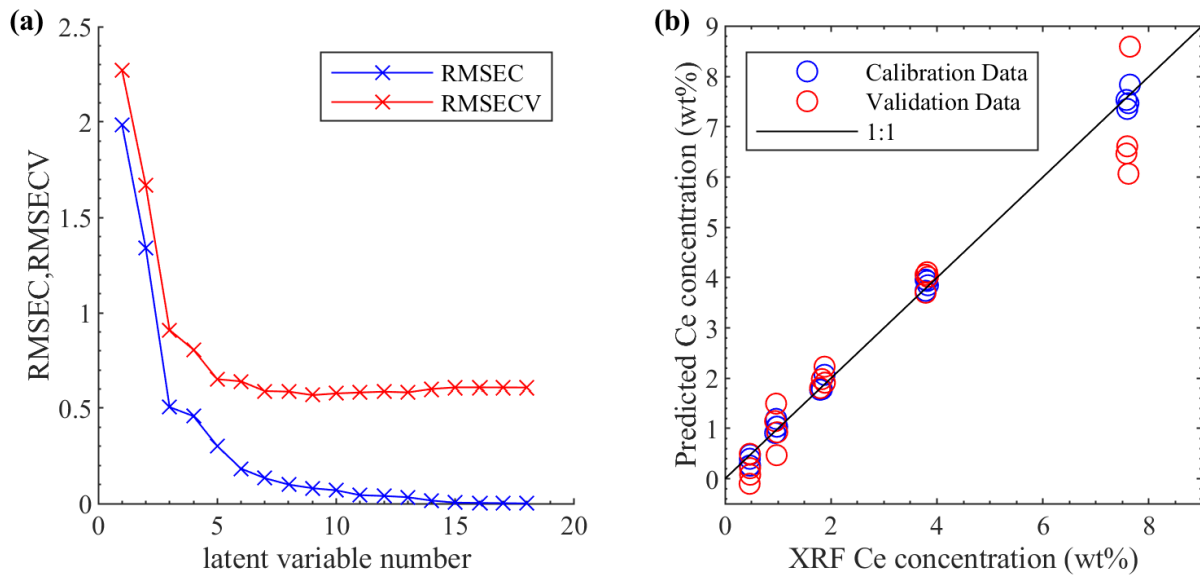
Figure 4. 29 (a) The PLS regression results for Ce in samples mixed with DIW using leave-one-sample-out cross-validation; (b) Predicted Ce from PLS versus measured XRF concentration.
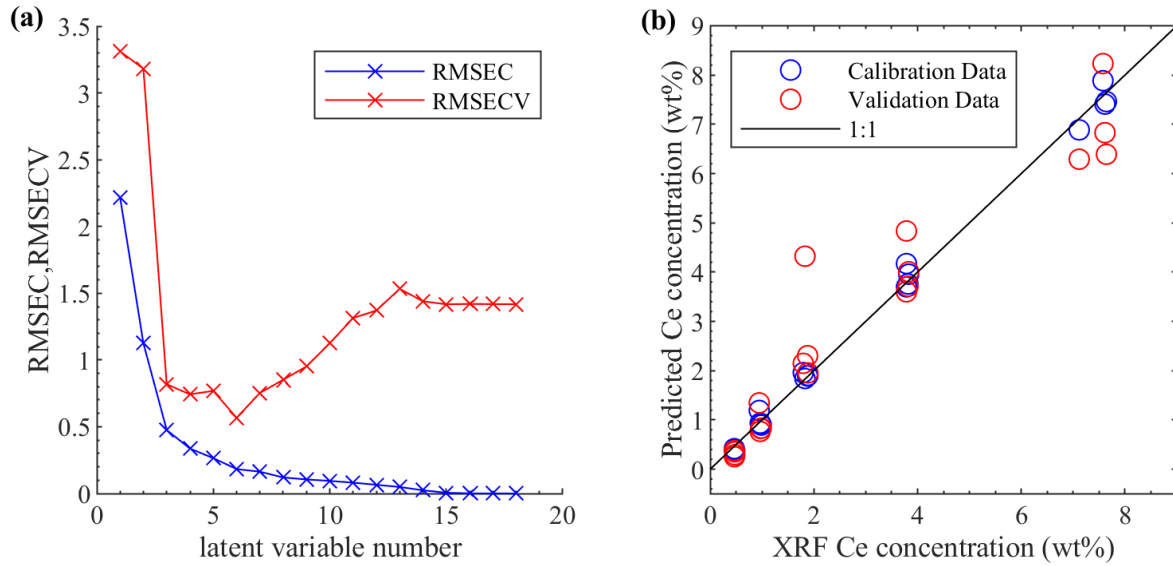
Figure 4. 30 (a) The PLS regression results for Ce in samples mixed with ASW using leave-one-sample-out cross-validation; (b) Predicted Ce from PLS versus measured XRF concentration.
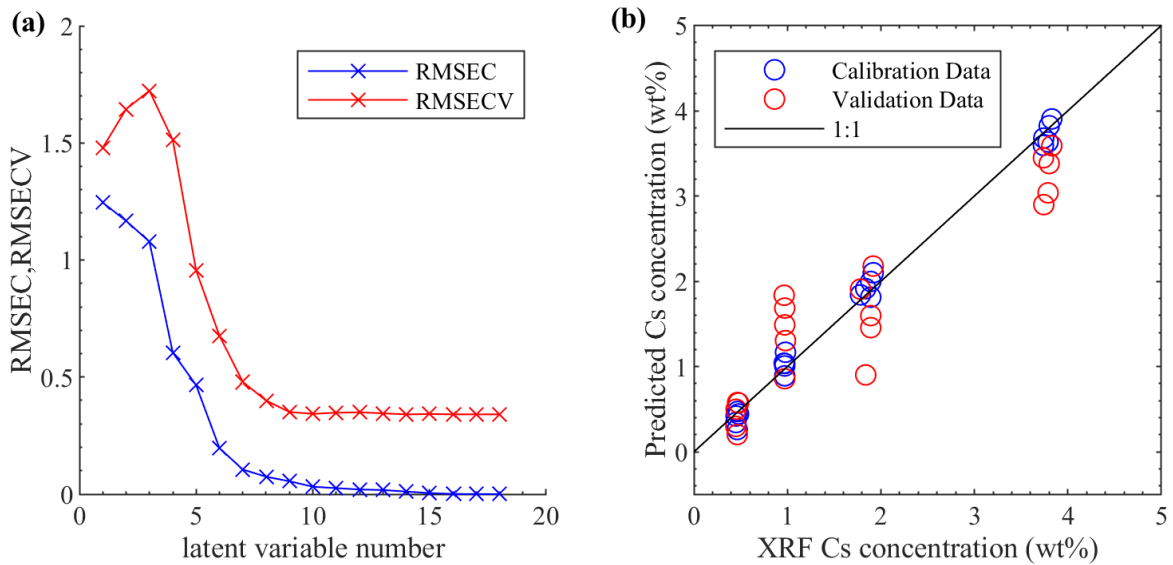
Figure 4. 31 (a) The PLS regression results for Cs in samples mixed with DIW using leave-one-sample-out cross-validation; (b) Predicted Cs from PLS versus measured XRF concentration.
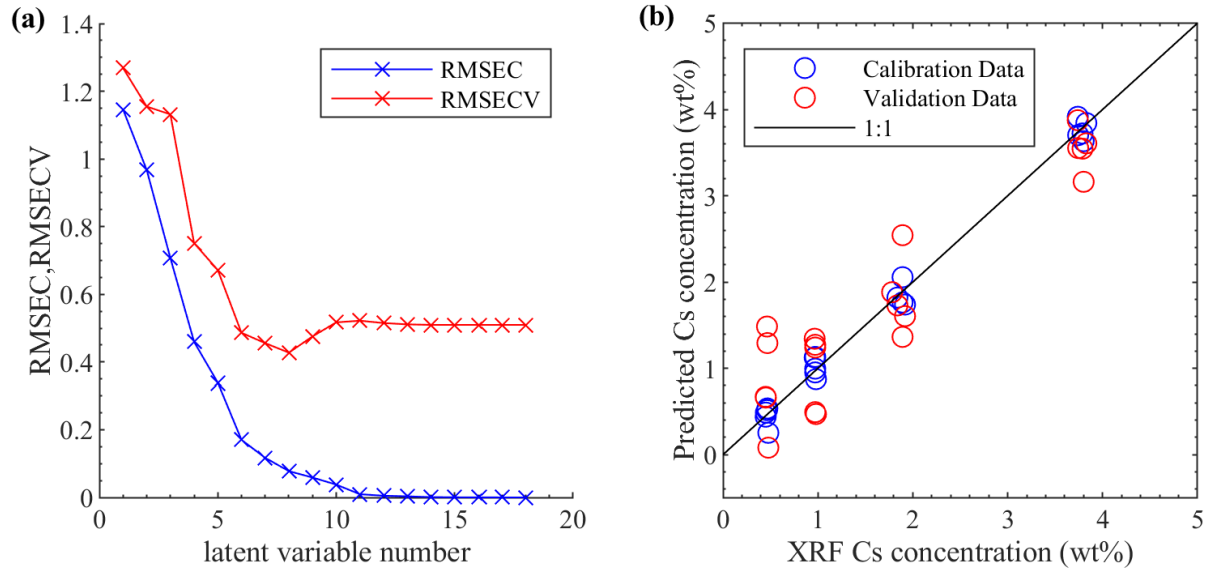
Figure 4. 32 (a) The PLS regression results for Cs in samples mixed with ASW using leave-one-sample-out cross-validation; (b) Predicted CS from PLS versus measured XRF concentration.

Table 4. 10 Quality parameters determined for PLS models.

Models	R^2	RMSECV (wt%)	LVs
PLS for Ce in samples with DIW	0.95	0.59	7
PLS for Ce in samples with ASW	0.95	0.57	6
PLS for Cs in samples with DIW	0.93	0.34	10
PLS for Cs in samples with ASW	0.89	0.43	8

4.7 Conclusion

LIBS along with PCA and PLS were used, in combination, to determine compositional analysis for certain non-radioactive materials of Ce (a surrogate for U and Pu) and Cs (a fission product) that immobilized within RSC matrix mixed with DIW. Since the aim of the whole study was to use this RSC as an emergency agent of immobilization near ocean water, ASW was also used to make the waste cement matrix. Total of 20 samples was prepared for each group of DIW

87

and ASW. These samples were tested using XRF to obtain the Ce and Cs concentrations. The average spectrum for each sample with 100 shots was done and then normalized. The Si 518.2 nm line was used to normalize the spectrum which reduced the %RSD values down to about 0.7% to 10%. The best calibration curve for Ce in samples with DIW and that with ASW was created using the peak areas of the Ce 571.8 nm line which had the LOD of 0.088 wt% and 0.091 wt%, with corresponding RMSECV of 0.419 wt% and 0.370 wt%, respectively. For Cs in samples mixed with DIW was Cs 697.1 nm line which had the LOD of 0.068 wt% and the RMSECV of 0.246 wt%. Similarly, for Cs in samples mixed with ASW using the Cs 851.9 nm line had the LOD of 0.042 wt% and the RMSECV of 0.249 wt%.

From analysis of the spectra and through PCA, the two principal components were able to explain 85.5% (PC1: 59.5% and PC2: 26%) for Ce-cement samples mixed with DIW and 91.4% (PC1: 72.0% and PC2: 19.4%) for Ce-cement samples mixed with ASW of the variations among total LIBS spectral information. These samples can be seen to be separated into five main groups in the score plot. For Cs, it was possible to explain 76.5% (PC1: 64.5% and PC2: 12.0%) for Cs-cement samples mixed with DIW and 89.4% (PC1: 75.7% and PC2: 13.7%) for Cs-cement samples mixed with ASW of the variations among total LIBS spectral information; these samples can be seen to be separated into four main groups in the score plot. When compared univariate calibration curves with the PLS calibration approach, the former showed better results. Overall, this study revealed a great promise of using LIBS in this application.

Chapter 5

Assessment of Leaching Characteristics for Understanding Immobilization of Surrogate Materials

5.1 Introduction

Various solidification techniques have been used to immobilize radioactive wastes resulting from the back-end of nuclear fuel cycle, operation, and possible impacts of major nuclear accidents. These processes can prevent or reduce radionuclide releases or migrations into the environment. That is, it would protect human health and minimize their impacts into the surrounding environment. Since radioactive waste forms will ultimately be in contact with groundwater, these radionuclides have a tendency to migrate from the waste forms into the surrounding soil/structure by a leaching mechanism. Therefore, the main aim for this chapter is to evaluate the leachability of cerium (^{140}Ce) and cesium (^{133}Cs) immobilized in a RSC matrix using the ANSI/ANS 16.1 leach test method [56, 110]. It should be noted that Ce has four naturally occurring stable isotopes: ^{136}Ce (0.186%), ^{138}Ce (0.251%), ^{140}Ce (88.449%), and ^{142}Ce (11.114%); for our convience of discussion, we will refer to it as ^{140}Ce. Dynamic and static tests were conducted to assess the leachability of Ce and Cs from the concrete samples, as well as, to compare to study the effect of the solution concentration gradient on the leaching rates.

5.2 Experimental program

RSC from CeraTech, Inc. was still being used for this study. All chemical compositions are listed in Table 3.1 (see Chapter 3). Samples were prepared by mixing the RSC with two medium types, DIW and ASW, at liquid to cement ratio of 0.2. About 1.2 mL of $CeCl_3$ and 1.2 mL CsCl solutions with each type of mediums were spiked into the cement. The details of the

89

sample preparation were previously described in chapter 3. For evaluating the leachability of Ce and Cs immobilized in a RSC, the experimental program was developed and summarized in Table 5.1. All RSC samples were cured at ambient laboratory temperature (21.7 ± 0.5 °C) in a humid atmosphere for 28 days before used for leach test.

Table 5. 1 The experimental program and characteristics of RSC samples used in dynamic and static leach tests.

	Sample No.	Cement (g)	Ce (wt %)	Cs (wt %)	Solution	Diameter (cm)	Height (cm)
Dynamic leach test	1	6	0.5	0.5	DIW	1.65	1.65
	2	6	0.5	1	DIW	1.65	1.65
	3	6	1	0.5	DIW	1.65	1.65
	4	6	0.5	0.5	ASW	1.65	1.65
	5	6	0.5	1	ASW	1.65	1.65
	6	6	1	0.5	ASW	1.65	1.65
Static leach test	7	6	0.5	1	DIW	1.65	1.65
	8	6	0.5	1	ASW	1.65	1.65

5.3 Static and dynamic leaching tests

Samples of RSC spiked with CeCl$_3$ and CsCl were suspended in the center of a closed cylindrical glass containers, as shown in Figure 5.1. The leachant solution was DIW with a pH of 7.08 and the conductivity of 14.10 µS/cm. The dynamic leach test was conducted according to the ANSI/ANS-16.1-2003 standard method [110]. The ANSI/ANS-16.1-2003 test consists of (1) immersing the RSC samples with constant dimensions in distilled water or DIW that will always be keeping at a constant leachate volume to solid-geometric surface-area ratio and (2) changing the leachate completely at constant intervals of time up to 90 days. The volume and the total

exposed surface area were calculated from the diameter and the height of the cylindrical samples. The cylindrical RSC samples were cylinders with a diameter and height of 1.65 cm. The leachate volume (129 mL) to total exposed sample surface area ratio was calculated to be 10 ± 0.2 cm. The cylindrical glass containers were maintained closed with screw caps to avoid vaporization. The leachate in this study was replaced by fresh DIW with the following intervals: 2 hours, 7 hours, 24 hours, 2 days, 3 days, 4 days, 5 days, 14 days, 28 days, 43 days, and 90 days.

For the static leach test, similar procedure as in the dynamic leach test was applied except the leachate solution was not replaced and 1 mL was withdrawn from the leachate solution at each time intervals parallel to the sampling in the dynamic test. The leachates were thereafter diluted with HNO_3 and analyzed for the concentrations of Ce and Cs using an Agilent 7900 inductively coupled plasma-mass spectrometry (ICP-MS), as shown in Figure 5.2.

The leachability of the Ce and Cs radionuclides from the RSC surrogate forms can be expressed by using a cumulative fraction leached CFL method [56] and also the incremental leaching rate (ILR)—it has dimensions of length over time [111], which can be calculated by using the following expressions:

$$ \text{CFL} = \left(\frac{\sum A_n}{A_o} \right) \tag{5.1} $$

$$ \text{ILR} = \left(\frac{\sum A_n}{A_o} \right) \frac{V}{S} \frac{1}{\sum t_n} \tag{5.2} $$

where A_o is the initial radioactivity present in the sample (μg), $\sum A_n$ is the cumulative radioactivity leached during leaching interval n (μg), S is the total surface area of the sample (cm^2), V is the volume of the sample (cm^3), and $\sum t_n$ is the cumulative period of leaching (s). According to ANSI/

91

ANS-16.1 standard mothed, it is assumed that the leaching behavior of species will be approximated as a semi-infinite medium if less than 20% of a leachable species is leached from uniform, regularly shaped solid. The effective diffusion coefficient (D_{ei}) for the leaching interval, $t_n - t_{n-1}$, often expressed in cm^2/s, for a species of interest can be calculated by using this common expression [110,112-114]:

$$D_{ei} = \pi \left[\frac{\left(\frac{A_n}{A_o} \right)}{\Delta t_n} \right]^2 \left(\frac{V}{S} \right)^2 T_m \tag{5.3}$$

and the leaching time (T_m) representing the mean timeof the interval in second; that is,

$$T_m = \left[\frac{1}{2} \left(\sqrt{t_n} - \sqrt{t_{n-1}} \right) \right]^2 \tag{5.4}$$

where Δt_n is the duration of the nth leaching interval $t_n - t_{n-1}$. However, if more than 20% of leachable species has been leached, D_{ei} can be calculated from the experimental data as follows:

$$D_{ei} = \frac{G.d_s^2}{t} \tag{5.5}$$

where G is the dimensionless time factor for the cylindrical sample that can be obtained from Table A.1 in ANSI/ANS-16.1-2003 [110], d_s the diameter of the cylinder sample (cm), and t is the total elapsed time from leaching initiation in second. The average effective diffusion coefficients ($<D_{ei}>$) were calculated from the values calculated for each leaching interval. The dimensionless leachability index (L_i) for each leached species i can be calculated from $<D_{ei}>$ values using this following expression:

$$L_i = \frac{1}{n} \sum_{1}^{n} \left[\log \left(\frac{\beta}{< D_{ei} >} \right) \right] \tag{5.6}$$

92

Where β is a constant (1 cm^2/s). According to the Nuclear Regulatory Commission (NRC) Standard, the leachability index that is evaluated based on ANSI/ANS 16.1 standard method should be greater than 6.0 to meet the requirement during encapsulation process for radioactive waste conditioning [115].

Figure 5. 1 Suspended RCS waste form during leaching test.
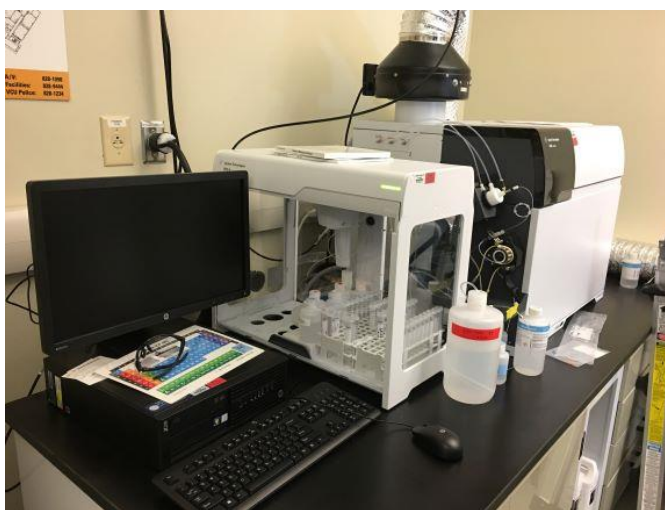
Figure 5. 2 Agilent 7900 ICP-MS instrument installed in the Radiochemistry Laboratory.

5.4 Measurement using inductively coupled plasma mass spectrometry (ICP-MS)

The leachate solution of the RSC samples was analyzed using ICP-MS technique to measure Ce and Cs concentrations. This technique turns the atoms of the elements in the sample into ions by a high-temperature ICP source and these ions are then separated and detected by the mass spectrometer. The argon plasma used in this method is formed as follows: a spark is applied to the argon flowing through the ICP torch in which the argon atoms will lose some of their electrons, thus argon ions are then formed that will collide with other argon atoms, forming an argon plasma with temperatures reach nearly 10000 °C. The leachate solution is introduced into the ICP plasma from a nebulizer as an aerosol. The elements in the aerosol are turned into gaseous atoms and then ionized towards the end of the plasma. These ions are then transferred into the mass spectrometer through the interface cones, in which they are separated by their mass-to-charge ratio. The ions afterward depart separately and enter into direct contact with a dynode of an electron multiplier, which detects electrons liberated by the effect of ions [36, 116].

Here, 5 ml and 1 ml from the dynamic and the static leach tests, respectively, were collected in a centrifuge tube. These samples are then filtered and acidified with the nitric acid (2% HNO_3), in which 5 ml was added to both leach test to ensure stability and comparability with calibration standards. Thirteen standard samples were prepared using multi-element blends: CCS1 and CCS4 (Inorganic Ventures). The diluted samples were analyzed using ICP-MS to calculate the concentration of Ce and Cs leached.

94

5.5 Theoretical methods

The migration of radionuclides of particular concern is carried out by leaching process that involves the following three stages: dissolution to the interstitial water, diffusion through interstitial water to the surface of the immobilized waste matrix, and consequent liberation to the saturated environment. A mathematical model with experimental data can be used to evaluate the leaching factors by fitting the experimental CFL, the leaching rate of radionuclides that transfer from immobilized waste matrix to the surrounding water, to the three following models. These are: first-order reaction model (FRM), diffusion model (DM), and first-order reaction/diffusion model (FRDM) [60, 117-120].

5.5.1 Method I: First-order reaction model (FRM)

The aim of using this model is to assess the leaching parameters of immobilized radionuclides in the RSC matrix. It is assumed that the surface exchange rate can be given by the first-order rate equation if the leaching process is governed by the exchange kinetics between the total surface area of the waste form and the leachate. Therefore, the leaching rate is proportional to the quantity of the initial amount of soluble radionuclides in the waste form; that is [119],

$$\frac{dM}{dt} = -kM \tag{5.7}$$

where M is the initial amount of soluble radionuclides in the waste form (mg/g) and k is a rate constant (s^{-1}). CFL of leaching radionuclides is obtained by:

$$CFL = M_o \left(1 - e^{-kt}\right) \tag{5.8}$$

95

5.5.2 Method II: Diffusion model (DM)

This model is applied to evaluate the leaching process if the migration of radionuclides in the waste matrix is controlled by diffusion. The one-dimensional flux of the diffusing radionuclides through the waste form can be estimated based on the solution of Fick's second law under the condition of semi-infinite medium and Fick's first law [60, 119]; that is,

$$J(t) = -D_{ec}\frac{\partial A}{\partial x}\Big|_{x=0} = -A_o\sqrt{\frac{D_{ec}}{\pi t}} \tag{5.9}$$

where $J(t)$ is the flux of diffusing radionuclide (mol cm^{-2} s^{-1}) and D_{ec} is effective diffusivity coefficient (cm^2/s) for the cumulative leach interval. The amount of a radionuclide in the leaching solution $A_n(t)$ during leaching interval n is given by:

$$A_n(t) = \int_0^t J(t)dt = 2A_o\sqrt{\frac{D_{ec}t}{\pi}} \tag{5.10}$$

CFL under this condition can be calculated by

$$CFL = \frac{\sum A_n}{A_o} = 2\left(\frac{S}{V}\right)\sqrt{\frac{D_{ec}t}{\pi}} \tag{5.11}$$

5.5.3 Method III: First-order reaction/diffusion model (FRDM)

This model is assumed that the leaching behavior of radionuclides from the waste form might be dominated by both the exchange kinetics and diffusion modes. Therefore, CFL can be determined by the combined solution to the FRM and DM models as the following:

$$CFL = M_o(1 - e^{-kt}) + 2\left(\frac{S}{V}\right)\sqrt{\frac{D_{ec}t}{\pi}} \tag{5.12}$$

96

5.6 Results and discussion

5.6.1 Leaching characteristics of ^{140}Ce

Figures 5.3a and 5.3b are shown the incremental leaching rates, for both dynamic and static leach tests, provided from ^{140}Ce immobilized in RSC matrices with DIW and ASW. It can be seen that the incremental leaching rates of ^{140}Ce decrease with time in both leach tests with the tw medium types. The results reveal that values of the incremental leaching rates of ^{140}Ce from RSC matrices with DIW and ASW by using dynamic leach test measured after 90 days were in the region of $2.8 \times 10^{-9} - 1.4 \times 10^{-5}$ cm/d and $5.8 \times 10^{-9} - 6.7 \times 10^{-6}$ cm/d, respectively. While in the static leach test, the values of the incremental leaching rates of ^{140}Ce from RSC matrices with DIW and ASW were in the region of $6.4 \times 10^{-10} - 1.3 \times 10^{-6}$ cm/d and $1.8 \times 10^{-11} - 2.9 \times 10^{-6}$ cm/d, respectively. The difference in the leaching rates of the RSC matrices may be caused by an increase of RSC porosity waste form resulted from an addition of different salt contents. Also, under the static condition, where the leachate solution was not replaced, the leachate solution might be reached to equilibrium with the waste form because the quantity of leach radionuclides approaches to the saturation limit. Figures 5.3a and 5.3b also show that the Sample 8 with static leach test has the lowest incremental leaching rate among the four samples. It should be noted that Samples 1, 3, 4, and 6 exhibit similar behavior to Samples 2 and 5 for the dynamic testing case.

CFL of ^{140}Ce from RSC matrices with (DIW and ASW) under both dynamic and static leach conditions were shown in Figures 5.4a and 5.4b. It was observed that the CFL of ^{140}Ce from RSC matrices with DIW and ASW under dynamic condition after 90 days were 3.6×10^{-5} and 2.1×10^{-5}, respectively. Also, under the static condition, CFL of ^{140}Ce from RSC matrices with DIW and ASW after 90 days were 6.5×10^{-6} and 5×10^{-6}, respectively. The results also showed that 0.004% and 0.002% of initial ^{140}Ce were released from the RSC matrices with DIW and ASW,

97

respectively, after 90 days under the dynamic leach test. Under the static condition, 0.0007% and 0.0005% of initial ^{140}Ce were released from the RSC matrices with DIW and ASW, respectively, after 90 days. Sample 8, under static leach test, shows lower CFL values in comparison to other four samples. The leaching behavior of ^{140}Ce from RSC matrices approximated that of a semi-infinite medium because the leaching of ^{140}Ce was less than 20% (based on ANSI/ANS-16.1-2003). However, the mechanism of leaching process of ^{140}Ce from RSC matrices can be identified by the slope of linear regression of the logarithm of CFL versus the logarithm of time [56, 121]. Thus, the mechanism of leaching process is controlled by either wash-off, diffusion, or the dissolution mechanism if the slope values are 0.35, 0.35 - 0.65, or > 0.65, respectively [56, 122]. The slope values for Ce release from all samples are listed in Table 5.2; the values were less than 0.35—that is, the surface wash off is the controlling mechanism.
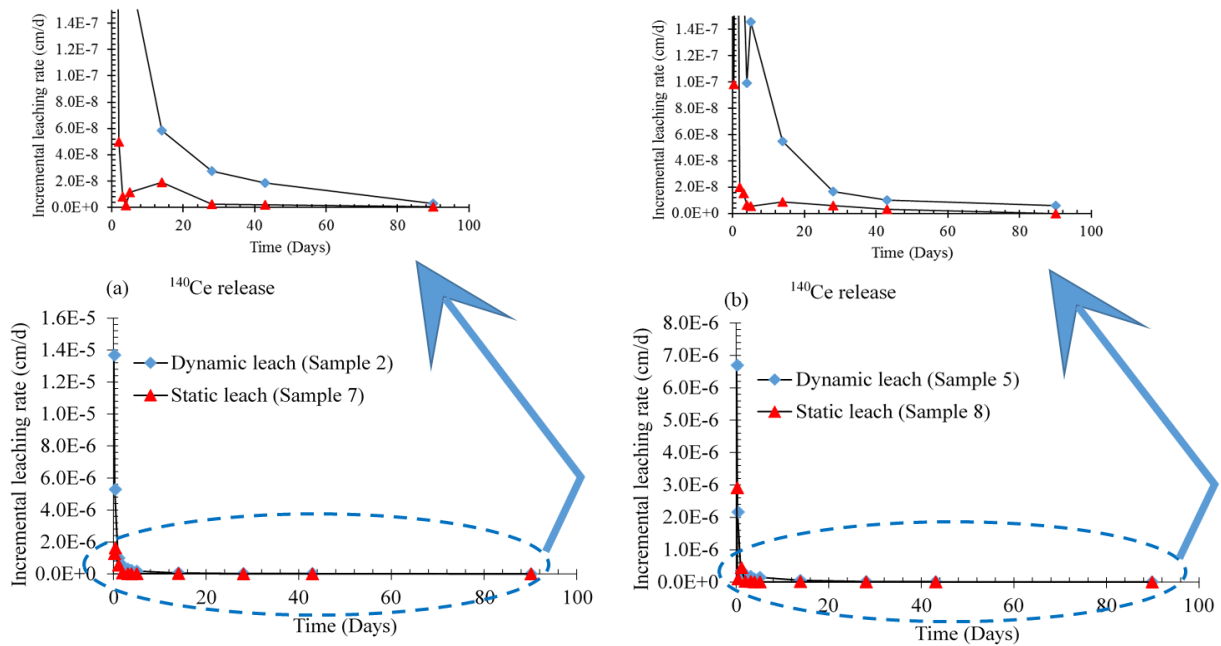
Figure 5. 3 ILR of Ce from RSC matrix under dynamic and static leach conditions (a) samples with 0.5 wt% Ce, 1.0 wt% Cs and DIW (b) samples with 0.5 wt% Ce, 1.0 wt% Cs and ASW.
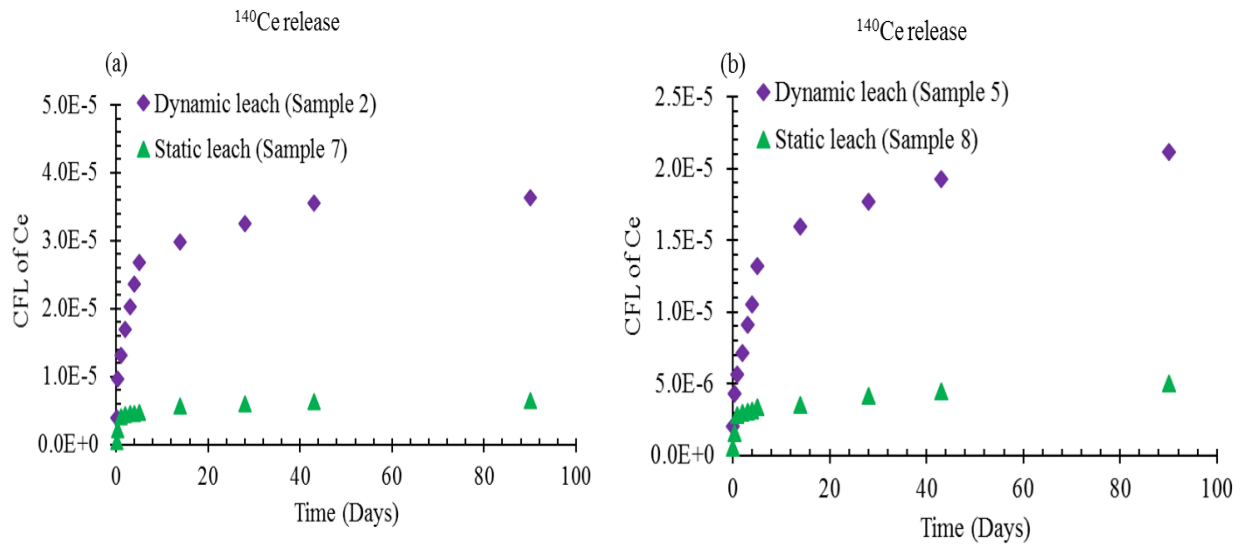
Figure 5. 4 CFL of Ce from RSC matrix under dynamic and static leach conditions (a) samples with 0.5 wt% Ce, 1.0 wt% Cs and DIW (b) samples with 0.5 wt% Ce, 1.0 wt% Cs and ASW.

Table 5. 2 The slope of linear regression for plot of log(CFL) versus the log(t) and R^2 (correlation coefficient) for the Ce and Cs released under dynamic and static leach tests.

Sample No.	Ce		Cs	
	Slope	$\mathbf{R^2}$	**Slope**	$\mathbf{R^2}$
1	0.31	0.92	0.62	0.90
2	0.30	0.91	0.62	0.89
3	0.29	0.94	0.60	0.88
4	0.33	0.94	0.53	0.91
5	0.33	0.96	0.46	0.89
6	0.32	0.94	0.43	0.89
7	0.32	0.7	0.55	0.94
8	0.25	0.88	0.46	0.92

99

5.6.2 Leaching characteristics of ^{133}Cs

The incremental leaching rates of ^{133}Cs from RSC matrices with (DIW and ASW) under both dynamic and static leach conditions were shown in Figures 5.5a and 5.5b, respectively. Other dynamic leaching samples behave similarly to Samples 2 and 5. The results showed that incremental leaching rates of ^{133}Cs decrease with time in both leach tests with the DIW and ASW. ILR values of ^{133}Cs from RSC matrices with DIW and ASW under dynamic condition after 90 days were in range of $1.1 \times 10^{-6} - 1.7 \times 10^{-4}$ cm/d and $7.8 \times 10^{-7} - 4.3 \times 10^{-4}$ cm/d, respectively. Under the static condition, ILR values of ^{133}Cs from RSC matrices with DIW and ASW after 90 days were in the scope of $5.1 \times 10^{-8} - 4.7 \times 10^{-5}$ cm/d and $3.5 \times 10^{-9} - 1 \times 10^{-4}$ cm/d, respectively. Results show that Sample 8 has the lowest incremental leaching rate among the four samples.
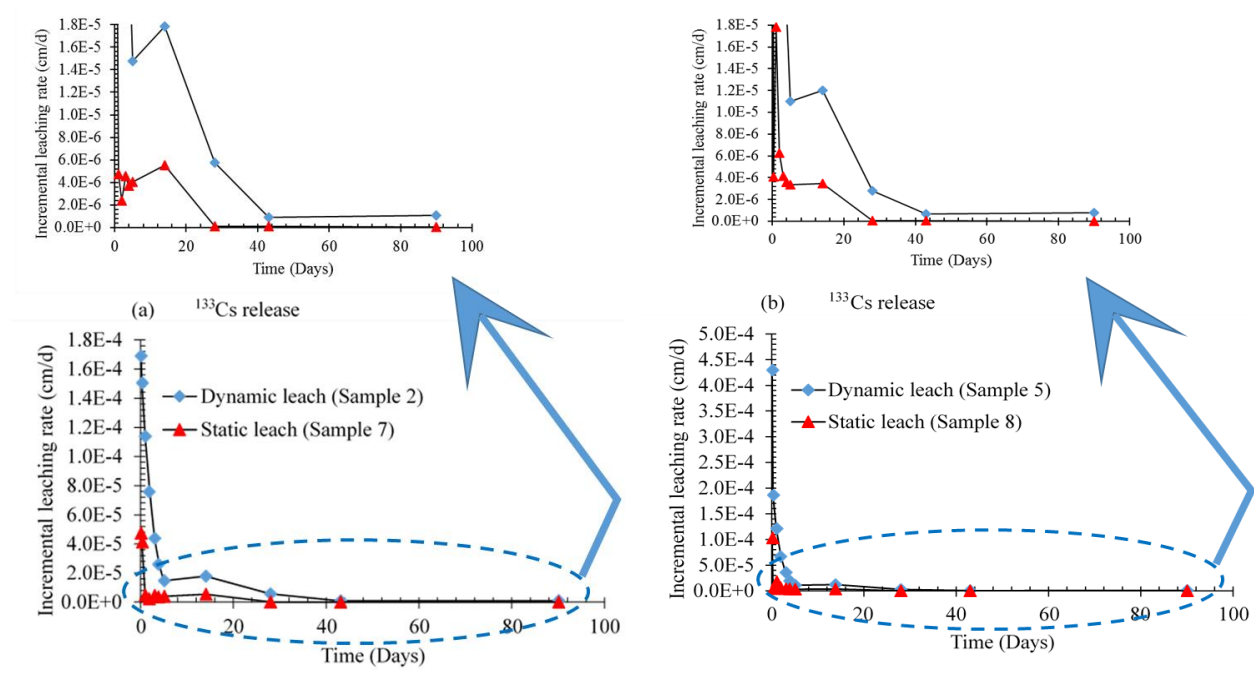
Figure 5. 5 ILR of Cs from RSC matrix under dynamic and static leach conditions (a) samples with 0.5 wt% Ce, 1.0 wt% Cs and DIW (b) samples with 0.5 wt% Ce, 1.0 wt% Cs and ASW.

100

Figures 5.6a and 5.6b are shown the CFL of ^{133}Cs from RSC matrices with (DIW and ASW) under both dynamic and static leach experiments. It can be seen that the CFL of ^{133}Cs from RSC matrices with DIW and ASW under dynamic condition after 90 days were 4.3×10^{-3} and 3.4×10^{-3}, respectively. CFL of ^{133}Cs from RSC matrices with DIW and ASW under the static condition after 90 days were 6×10^{-4} and 5.8×10^{-4}, respectively. It was also observed that the ratios of ^{133}Cs released to the initial amount of ^{133}Cs from RSC matrices with DIW and ASW after 90 days under the dynamic leach condition were 0.429 % and 0.338 %, respectively. The ratios of ^{133}Cs released, under the static leach condition, from the RSC matrices with DIW and ASW after 90 days were 0.060 % and 0.049 %, respectively. The controlling mechanism is the diffusion (see the slope values from Table 2).
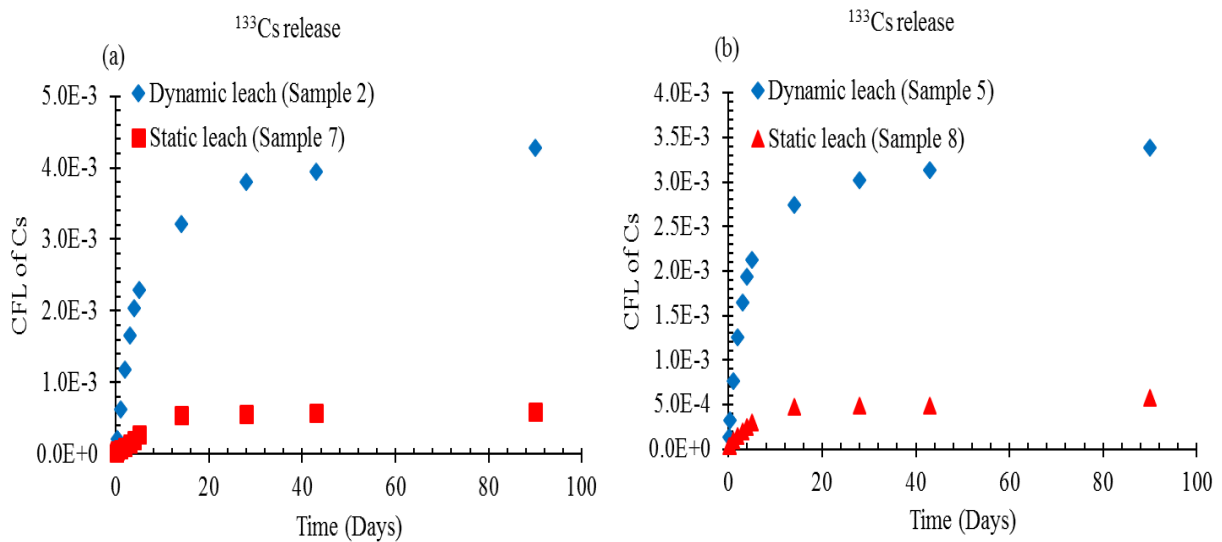
Figure 5. 6 CFL of Ce from RSC matrix under dynamic and static leach conditions (a) samples with 0.5 wt% Ce, 1.0 wt% Cs and DIW (b) samples with 0.5 wt% Ce, 1.0 wt% Cs and ASW.

The average effective diffusivity $<D_{ei}>$ and the leachability indices (L) of ^{133}Cs and ^{140}Ce from RSC matrices with (DIW and ASW) for 90 days under both dynamic and static leach conditions were compared with other leaching studies that also used the ANSI/ANS-16.1 standard

method, as shown in Table 5.3. Here, $<D_{ei}>$ and L for ^{133}Cs in this study were calculated to be

$5.7 \times 10^{-13} - 1.1 \times 10^{-14}$ cm^2/s and 12.7 – 14.7, respectively. For ^{140}Ce, $<D_{ei}>$ and L were ranged

from $8.2 \times 10^{-17} - 1.9 \times 10^{-18}$ cm^2/s and 16.7 – 18.7, respectively. It can be also seen that the mean

leachability indices (L) for ^{133}Cs and ^{140}Ce were higher than 6 and also greater than the other

studies in the Table 5.3. Therefore, this matrix can be catalogued as efficient materials for

immobilizing Ce and Cs from nuclear wastes.

Table 5. 3 The comparison between results (D_{ei} and L_i) from this study and other leaching studies.

Binder	Type of Waste	Leaching Time (Day)	Volume/ Surface Area (cm)	$<D_{ei}>$ (cm^2/s)	L_i	Ref.
Backfilling pozzolanic cement mortar	Cs within simulated BWR	90	–	1.7 x 10^{-7}	6.8	[123]
Ceramicrete	10 wt% CsCl 15 wt% CsCl	90	20	-	11.5 11.7	[124]
Ordinary Portland Cement (Type-I/II)	^{137}Cs	90	10	1.2 x 10^{-9} – 3.3 x 10^{-9}	8.55 – 9.02	[125]
fly ash belite cement (FABC-2 W) Gismondine-type Na-P1 zeolite	CsCl solution	90	10	2.2 x 10^{-7} 2.8 x 10^{-9}	6.7 8.6	[126]
Cement with differen wt% of Biocha	Cs-134 solution	90	10	1.9 x 10^{-12} – 2.7 x 10^{-12}	12.0 –12.4	[56]
RSC	CsCl solution CeCl$_3$ solution	90	10	5.7 x 10^{-13} – 1.1 x 10^{-14} 8.2 x 10^{-17} – 1.9 x 10^{-18}	12.7 – 14.7 16.7 – 18.7	This Study

102

5.6.3 Leaching parameters and mechanism

The experimental CFL data of ^{140}Ce and ^{133}Cs from RSC matrices with (DIW and ASW) under both dynamic and static leach experiments were fitted to the non-linear form of FRM, DIM, and FRDM to assess the mechanisms that stimulate the leaching process of the studied waste matrices as shown in Figures 5.7a – 5.7d and 5.8a – 5.8d. The leaching parameters obtained from these models fitting of the experimental data of ^{140}Ce and ^{133}Cs are shown in Tables 5.4 and 5.5. It can be seen that the patterns of the experimental data for ^{140}Ce leaching from RSC matrices with (DIW and ASW) under both dynamic and static leach conditions were similar to that of the FRM. Therefore, they could be represented by this model, although the release of ^{140}Ce from the RSC matrices was underestimated. On the other hand, the DM is different from that of the experimental data for ^{140}Ce. For ^{133}Cs leaching from RSC matrices with (DIW and ASW) under both dynamic and static leach conditions, the patterns were similar to that of the FRM and different from that of the DM. However, it was observed that the leaching phenomena of ^{140}Ce and ^{133}Cs cannot be fully represented with a single model; therefore, it could be represented by a combination of FRM and DIM, namely (FRDM). Both results simply indicate that kinetics controls interchangeably with diffusion mechanism at an earlier leaching time interval (< 8 days) and progressively dominated leaching process after 8 hrs. The values of root mean square error (RMSE) and the correlation coefficient (R^2) for how well the experimental CFL points fit to the regression curve, are also shown in Tables 5.4 and 5.5. According to the R^2 and RMSE values for the ^{140}Ce and ^{133}Cs leaching, it was observed that the data could be represented by FRDM. By comparison, the leaching parameters obtained from the FRDM fitting of the experimental data of ^{133}Cs with the literature [60] was found that the values of k and D_{ec} are in the range of 7 x 10^{-3} – 0.28 and 4.6 x 10^{-6} – 1.2 x 10^{-4}, respectively, while from this study are in the range of 0.11 – 0.30 and 0.31 x 10^{-}

103

$^8 - 15.30 \times 10^{-8}$, respectively. On the other hand, the values of D_{ec} obtaind from the experimental data of ^{140}Ce and ^{133}Cs were compared with that created from FRDM as shown in Table 5.6. The difference between values is due to the fitting of experimental data to FRDM is depend on the change of three parameters (k, M, and D_{ec}), therefore the value of D_{ec} will be affected by those two parameters (k and M).

Figure 5. 7 Non-linear fit of the Ce CFL to the FRM, DM, and FRDM models; (a and b) under dynamic leach condition; (c and d) under static leach condition.
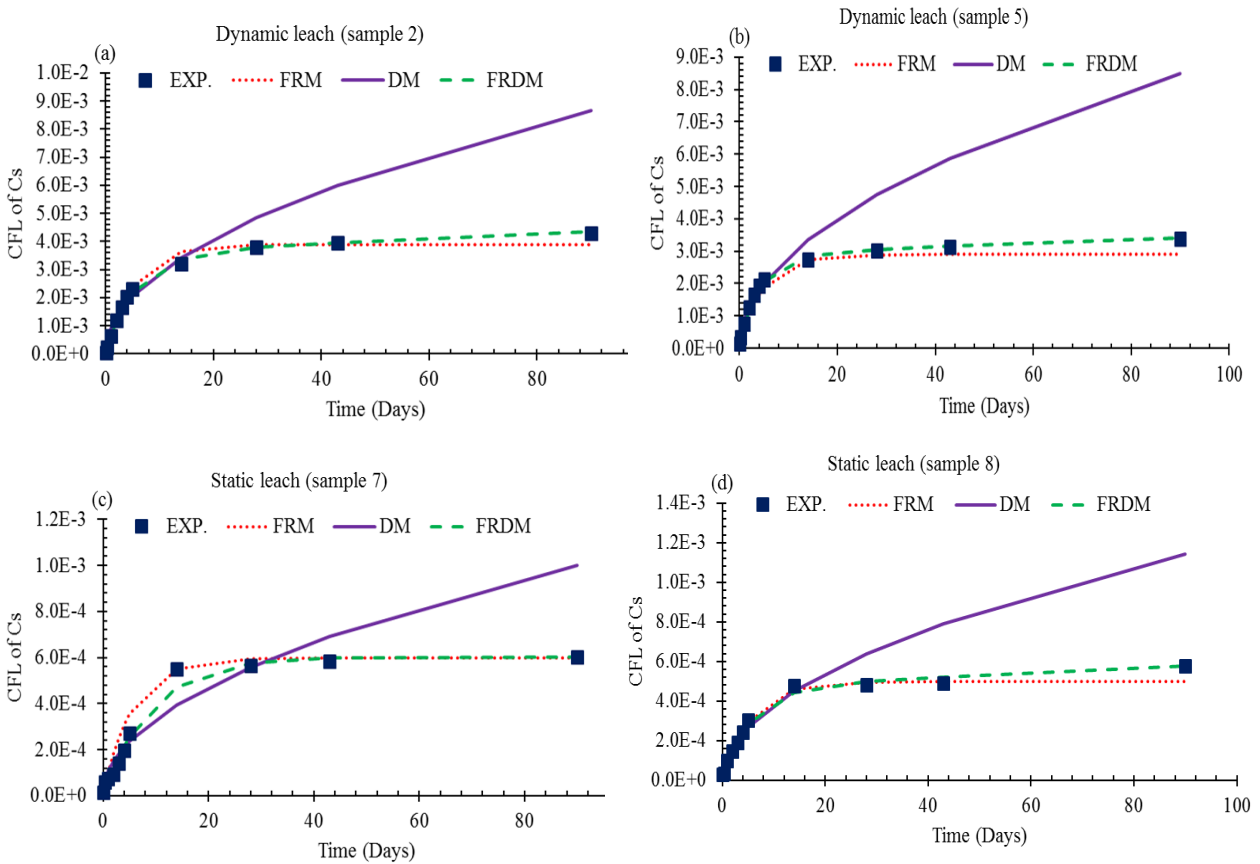
Figure 5. 8 Non-linear fit of the Cs CFL to the FRM, DM, and FRDM models; (a and b) under dynamic leach condition; (c and d) under static leach condition.

Table 5. 4 Results of the different models fitting of the experimental ^{140}Ce leaching data.

model	Sample No.	1	2	3	4	5	6	7	8
FRM	**k (s^{-1})**	0.20	0.23	0.21	0.19	0.19	0.23	0.29	0.30
	M *10^5	3.38	3.65	2.44	4.31	1.94	2.89	0.66	0.46
	RMSE *10^6	3.88	3.83	2.58	4.10	1.7	2.81	1.10	0.78
	R^2	0.97	0.97	0.97	0.96	0.97	0.96	0.86	0.84
DM	**D$_{ec}$ (cm^2/s) *10^{10}**	11.10	11.77	5.86	13.00	3.24	7.29	0.74	0.29
	RMSE*10^6	0.28	0.27	0.19	0.25	0.13	0.20	8.02	3.91
	R^2	0.75	0.76	0.79	0.86	0.86	0.84	0.60	0.74
FRDM	**k (s^{-1})**	0.28	0.27	0.27	0.18	0.19	0.23	0.9	0.87
	M*10^5	3.38	3.50	2.31	4.35	1.94	2.70	0.50	0.31
	D$_{ec}$ (cm^2/s) *10^{13}	1.77	2.07	2.07	2.67	2.67	13.5	2.97	3.87
	RMSE*10^6	2.85	3.30	2.06	4.36	1.77	2.67	0.49	0.38
	R^2	0.98	0.98	0.98	0.97	0.98	0.97	0.94	0.95

105

Table 5. 5 Results of the different models fitting of the experimental [133]Cs leaching data.

model	Sample No.	1	2	3	4	5	6	7	8
FRM	k (s^{-1})	0.20	0.19	0.17	0.20	0.21	0.20	0.18	0.18
	M *10^3	3.20	3.90	3.60	2.91	2.90	3.90	0.60	0.50
	RMSE *10^4	1.54	1.79	1.82	0.85	2.47	3.29	0.62	0.27
	R^2	0.99	0.99	0.99	0.99	0.99	0.99	0.95	0.98
DM	D_{ec} (cm^2/s) *10^6	6.24	7.44	7.44	6.39	7.14	11.90	0.01	0.13
	RMSE*10^4	15.32	15.05	16.31	17.74	18.37	23.64	1.36	2.00
	R^2	0.82	0.84	0.80	0.81	0.80	0.80	0.82	0.84
FRDM	k (s^{-1})	0.19	0.19	0.22	0.22	0.26	0.30	0.11	0.19
	M*10^3	2.90	3.10	3.10	2.40	2.60	3.20	0.50	0.40
	D_{ec} (cm^2/s) *10^8	4.83	15.30	6.28	6.28	6.28	13.80	0.16	0.31
	RMSE*10^4	0.79	0.78	0.78	0.39	0.71	1.12	0.38	0.19
	R^2	1	1	1	1	1	1	0.97	0.99

Table 5. 6 The comparison between results (D_{ec}) from experimental and FRDM for the Ce and Cs released under dynamic and static leach tests.

	Ce		Cs	
Sample No.	D_{ec} (cm^2/s) (Experimental)	D_{ec} (cm^2/s) (FRDM)	D_{ec} (cm^2/s) (Experimental)	D_{ec} (cm^2/s) (FRDM)
1	1.26E-14	1.77E-13	1.28E-10	4.83E-08
2	1.39E-14	2.07E-13	1.82E-10	15.30E-08
3	6.50E-15	2.07E-13	1.60E-10	6.28E-08
4	2.14E-14	2.67E-13	9.89E-11	6.28E-08
5	4.39E-15	2.67E-13	1.16E-10	6.28E-08
6	1.00E-14	13.5E-13	1.96E-10	13.80E-08
7	4.56E-16	2.97E-13	3.80E-12	0.16E-08
8	2.46E-16	3.87E-13	3.16E-12	0.31E-08

106

5.7 Conclusions

The leaching behavior of ^{140}Ce and ^{133}Cs from RSC matrices with (DIW and ASW) under both dynamic and static leach conditions were evaluated. The CFL of the studied radionuclides were significantly reduced for all samples under static conditions where the leachate solution was not replaced, the leachate solution might be reached to equilibrium with the waste form because the quantity of leach radionuclides approaches to the saturation limit. The leaching of ^{140}Ce and ^{133}Cs from RSC matrices with (DIW and ASW) under both dynamic and static leach conditions was found less than 20% and suggests that the leaching behavior of ^{140}Ce and ^{133}Cs approximates that of a semi-infinite medium. It was found that, by fitting the experimental data to FRM and DM models, the leaching phenomena of ^{140}Ce and ^{133}Cs cannot be fully represented with a single model, therefore, it could be represented by a combination of FRM and DIM, namely (FRDM). In all the cases, the average leachability index (L) for ^{140}Ce and ^{133}Cs, are greater than the recommended minimum of 6 that allowed their acceptance for disposal. It could be stated that RSC with DIW and ASW are a promising and economical matrix for immobilizing non-radioactive Ce and Cs and that could be applied to actual radioactive materials.

Chapter 6
Summary

6.1 Summary

6.1.1 Chapter 1: Purpose, Motivation, Approach

- Cementitious materials are one of the most materials widely used for immobilization radioactive materials due to its availability and low cost used.

- The goal of this study is to perform a technical assessment of RSC, as an alternative agent for immobilization of fission products or radioactive materials.

- For this purpose, different Ce and Cs concentrations used as a surrogate material for (U and Pu) and fission products, respectively, in cement mixtures with deionized water (DIW) and artificial seawater (ASW).

- The setting time and mechanical properties of the wasteform were evaluated and different techniques such as XRF, XRD, and SEM equipped with EDX to obtain the compositional analysis, identification of phases of this matrix, and microstructure and elements mapping, respectively.

- LIBS analysis with univariate and multivariate (PCA and PLS) methods were explored to detect the surrogate elements for nuclear materials captured in ceramic materials.

- Finally, the dynamic and static leaching tests were achieved to evaluate the leachability of Ce and Cs from RSC matrix using the method suggested by ANSI/ANS 16.1.

6.1.2 Chapter 2: Literature Review

- Ordinary Portland cement (OPC) is one of the most commonly cement used for immobilization of radioactive wastes and there are 5 types of this cement which are type I

108

(Normal), type II (Moderate Sulfate Resistance), type III (High Early Strength), type IV (Low Heat of Hydration), and type V (High Sulfate Resistance), in which each type of this cement has different mineral Composition (wt %) with different characteristics and uses.

- There exists an opportunity to improve the mechanical and durability properties of OPC by mixing with other inorganic materials, namely supplementary cementitious materials, including blast furnace slag and pulverized fuel ash.

- LIBS has been used determining the elemental composition of different materials due to its significant advantages compared with other elemental composition techniques.

- The optimal conditions for LIBS were laser energy ranged between 8.3 – 50 mJ, gate delay ranged between 1 – 5 μs, and the gate width of 5 μs.

- Univariate calibration method and chemometric methods PCA and PLS were employed for analysis LIBS data. The results from these literatures showed that the detection limit of elements in the solid samples were ranged between 4.2 – 480 ppm.

- Different leaching tests have been used in order to evaluate radioactive waste forms selected if they have complied with the regulatory requirements. Under dynamic leaching test, the leachate solution was replaced after the leaching, whereas under the static condition, the leachate solution will not be replaced.

- The ANSI/ANS 16.1-2003 and IAEA methods have been applied for the leach experiment, in which the leachate solution in ANSI/ANS 16.1-2003 method was replaced after the leaching periods of 2 h, 7 h, 24 h, 14 days, 28 days, 43 days and 90 days, while in IAEA method, the leachate solution was replaced after the leaching periods of every day for 7 days, and then every week for 1 month and every month, until 125th day.

- The leachability indices (L) must exceed the required value of 6, as recommended by the US Nuclear Regulatory Commission (NRC) Standard for waste acceptance criteria.

6.1.3 Chapter 3: Experimental Development with Ce as a Surrogate Material for U (Preliminary studies)

- Two different sample groups were generated: The first group was a mixture of the cement powder with DIW with different concentrations of Ce (0, 2, 5, 7.5, and 10 wt%) while the second group included the cement powder, ASW, and the same set of Ce concentrations.

- The setting time and mechanical properties of RSC matrix have been evaluated. The microstructure and composition of the waste form were characterized by using techniques such as XRF, XRD, and SEM/EDX.

- The final setting times (FST) of RSC increased as (w/c) ratio increased. The best and lower FST for RSC was (12.5 min ± 2 min) at 0.2 w/c ratio. The FST of RSC binder at 0.2 w/c ratio with different ratios of Ce (2, 5, 7.5, and 10 wt%) with DIW and ASW, respectively, were decreased with increasing Ce content.

- The porosity of the final waste forms increased with the increase of $CeCl_3$ for both solutions (DIW and ASW) because an addition of these salts reduced the amount of free water joined in the reaction. The density of RSC with DIW and ASW was increased progressively with the addition of $CeCl_3$.

- The compressive strength of RSC samples with DIW and ASW were reduced remarkably with an increase of Ce content. The recommended compressive strength for the final solid waste form was higher than the required value of 3.4 MPa according to the NRC.

- The main oxides phases identified at the composites with DIW and ASW were struvite-K ($KMgPO_4.6H_2O$), quartz (SiO_2), and periclase (MgO). In addition, there were two new peaks showing around ($2\theta = 28.207^o$) for $Ce_{4.667}(SiO_4)_3O$ phase and around ($2\theta = 58.601^o$) for $CeAl_{11}O_{18}$ phase growing up as Ce concentration increased.

- The distribution of Ce measured by using XRF on samples of RSC and different Ce concentrations was approximately uniform with the depth, despite some contents of cement and Ce were sticking to the impeller during mixing (considered as lost contents).

- pH values were significantly reduced with the increase of Ce content in both DIW and ASW. However, the pH values of RSC are still within the basicity range. This would corrode the waste metals—thus, cracking of the waste form and releasing of hydrogen gas.

- The electrical conductivity values of RSC and various Ce contents with DIW and those with ASW were increased considerably with the increase of Ce content.

- SEM micrograph of the RSC sample without Ce showed that there is no continuous structure and the microstructure seems to be porous. The shape of the struvite-K particles was laminar flat plates, while different sizes of spherical particles correspond to fly ash (FA) particles. The results from the EDX spectrums showed that the composition of RSC was consisted of majority of silicon (Si), aluminum (Al) minerals, struvite-K crystals, unreacted MgO and trace amounts of phosphate (P) and potassium (K).

- SEM micrograph of the RSC sample with 10 wt% Ce showed that the struvite-K particles were joined together to form a large undefined shape or an approximately cubic. The EDX analysis showed that the major elements were P, K, Mg, and O. Also, the microstructure shows that there are some FA particles with chemical elements (Si, Al, and Fe), while

111

unreacted MgO was not shown. EDX results also displayed the existence of Ce spread on the pore wall with the following elements: Si, Al, Mg, K, P, Fe and O.

6.1.4 Chapter 4: Measurement of a Surrogate Material (Ce and Cs) in Cement Matrix

- The main goal of this chapter is to explore the LIBS measuring technique of non-radioactive materials in the rapid setting cement (RSC). Cerium chloride ($CeCl_3$) and cesium chloride (CsCl) were varied in two matrices of Ce (0.5 – 8 wt%) and Cs (0.5 – 4 wt%) with DIW and ASW mixed with cement mixtures.

- XRF and LIBS techniques have been applied to detect the surrogate elements for nuclear materials captured in ceramic materials.

- Univariate and multivariate analyses (PCA and PLS) were employed for analysis of data LIBS. The following results were observed. Optimal conditions for LIBS analysis in order to improve the detection limit of Ce and Cs elements in LIBS were laser pulse energy of 30 mJ at gate delay of 6 µs and gate width of 1.05 µs.

- The measured concentrations of Ce and Cs elements by XRF were compared with the prepared concentrations. The % differences on average for samples with DIW were $5.7 \pm 2.4\%$ for Ce and $5.8 \pm 2.7\%$ for Cs. Samples mixed with ASW were $4.2 \pm 1.6\%$ for Ce and $5.5 \pm 2.3\%$ for Cs. This difference between prepared and measured results, may be due to, the fact that some contents of cement and Ce and Cs were sticking to the impeller during mixing (considered as lost contents).

- The %RSD values averaged after the normalization were averaged between 0.7% and 10% with a maximum reaching up to 20%.

112

- The main visible peaks in spectrum LIBS were due to Si, K, Na, Mg Ca, and Fe and were present in all samples. The best three lines selected based on (RI, (S/B) ratio, and (S/N) ratio) for Ce and Cs were (535.2, 551.1, and 571.8) and (697.1, 851.9, and 894.4), respectively.

- Between the three selected Ce lines in samples with DIW and with ASW, the 571.8 nm calibration curve made using the peak area had the lowest LOD (0.088 and 0.091 wt%), RMSE (0.0005 and 0.0006), RMSEC (0.371 and 0.338 wt%), and RMSECV (0.419 and 0.370 wt%), and the highest R^2 (0.980 and 0.982).

- It was observed that between the three selected Cs lines in samples with DIW, the 697.1 nm calibration curve created using the peak area had the lowest LOD (0.068 wt%), RMSE (0.0017), RMSEC (0.218 wt%), and RMSECV (0.246 wt%), and the highest R^2 (0.971).

- The Cs 851.9 nm calibration curve created using the peak area in samples with ASW was the best among the three selected Cs lines, it had the lowest LOD (0.042 wt%), RMSEC (0.222 wt%), and RMSECV (0.249 wt%), and the highest R^2 (0.970).

- The first two principal components for Ce samples mixed with DIW accounted for 59.5% (PC1) and 26% (PC2) while for those with ASW accounted for 72.0% (PC1) and 19.4% (PC2) of the total spectral variation. The results of PCA showed five clusters for all spectra.

- The first two principal components for Cs samples mixed with DIW accounted for 64.5% (PC1) and 12.0% (PC2) while for those with ASW accounted for 75.7% (PC1) and 13.7% (PC2) of the total spectral variation. The results of PCA showed four clusters for all spectra.

- Seven and eight factors were best to obtain a calibration PLS model for Ce with the optimum predictability. The RMSECV for samples mixed with DIW and that with ASW

113

were 0.59 and 0.57 wt% Ce, which were larger than the calibration curve case. Additionally, PLS models also had good correlation coefficients (0.95).

- Ten and eight factors were need to obtain a best calibration PLS model for Cs, with R^2 of 0.93 and 0.89, and RMSECV of 0.34 and 0.43 wt%, for samples mixed with DIW and that with ASW, respectively.

6.1.5 Chapter 5: Assessment of the Leaching Characteristics of Immobilization a Surrogate Material

- The dynamic and static tests were conducted to assess the leachability of Ce and Cs from the concrete samples.
  - The dynamic leach test was conducted according to the ANSI/ANS-16.1-2003 standard method, in which the leachate solution in this test was replaced by fresh DIW during 2, 7, and 24 hours and 2, 3, 4, 5, 14, 28, 43, and 90 days.
  - The static leach test had the same procedure, except the leachate solution was not replaced.
- The leachates were thereafter diluted with HNO_3 and analyzed for the concentrations of Ce and Cs using by an Agilent 7900 inductively coupled plasma-mass spectrometry (ICP-MS).
- Three mathematical models (FRM, DM, and FRDM) with experimental data can be used to evaluate the leaching factors by fitting the experimental Cumulative fraction leached (CFL) to CFL from these models.
- The incremental leaching rates of ^{140}Ce from RSC matrices with DIW and ASW by using dynamic leach test measured after 90 days were in the region of $2.8 \times 10^{-9} – 1.4 \times 10^{-5}$ cm/d and $5.8 \times 10^{-9} – 6.7 \times 10^{-6}$ cm/d, respectively. While, in the static leach test, the values of

114

the incremental leaching rates of ^{140}Ce from RSC matrices with DIW and ASW were in the scope of 6.4 x 10^{-10} – 1.3 x 10^{-6} cm/d and 1.8 x 10^{-11} – 2.9 x 10^{-6} cm/d, respectively.

- The CFL of ^{140}Ce from RSC matrices with DIW and ASW under dynamic condition after 90 days were 3.6 x 10^{-5} and 2.1 x 10^{-5}, respectively. On the other hand, under the static condition, the CFL of ^{140}Ce from RSC matrices with DIW and ASW after 90 days were 6.5 x 10^{-6} and 5 x 10^{-6}, respectively.

- The incremental leaching rates of ^{133}Cs from RSC matrices with DIW and ASW under dynamic condition after 90 days were in range of 1.1 x 10^{-6} – 1.7 x 10^{-4} cm/d and 7.8 x 10^{-7} – 4.3 x 10^{-4} cm/d, respectively. On the other hand, under the static condition, the incremental leaching rates of ^{133}Cs from RSC matrices with DIW and ASW after 90 days were in the scope of 5.1 x 10^{-8} – 4.7 x 10^{-5} cm/d and 3.5 x 10^{-9} – 1 x 10^{-4} cm/d, respectively.

- The CFL of ^{133}Cs from RSC matrices with DIW and ASW under dynamic condition after 90 days were 4.3 x 10^{-3} and 3.4 x 10^{-3}, respectively. Whereas, the CFL of ^{133}Cs from RSC matrices with DIW and ASW under the static condition after 90 days were 6 x 10^{-4} and 5.8 x 10^{-4}, respectively.

- The mean leachability indices (L) for ^{133}Cs and ^{140}Ce were higher than 6; that allowed their acceptance for disposal according to NRC.

- By fitting the experimental data to FRM and DM models, the leaching phenomena of ^{140}Ce and ^{133}Cs cannot be fully represented with a single model, therefore, it could be represented by a combination of FRM and DIM, namely (FRDM).

- By comparison, the average value of D_{ei} from this study with other studies in Table 5.3 was found that D_{ei} from current study was much smaller.

115

- The leaching parameters obtained from the FRDM fitting of the experimental data of ^{133}Cs with the literature [60] was found that the values of k and D_{ec} are in the range of 7 x 10^{-3} – 0.28 and 4.6 x 10^{-6} – 1.2 x 10^{-4}, respectively, while from this study are in the range of 0.11 – 0.30 and 0.31 x 10^{-8} – 15.30 x 10^{-8}, respectively. On the other hand, the values of D_{ec} obtaind from the experimental data of ^{140}Ce and ^{133}Cs were compared with that created from FRDM as shown in Table 5.6. The difference between values is due to the fitting of experimental data to FRDM is depend on the change of three parameters (k, M, and D_{ec}), therefore the value of D_{ec} will be affected by those two parameters (k and M).

Chapter 7
Future Work

Overall, RSC is an ideal material for radioactive materials immobilization; however, there is still a scope for further research in several areas such as

1. Using gadolinium (Gd) as a surrogate for Pu and strontium (Sr) as a surrogate for fission products.

2. Further study on feasibility of RSC with multi-elements is necessary to advance knowledge of competitive kinetic and diffusional aspects within the system among those elements.

3. Further work needs to be done on the LIBS technique by applying to a broader range of different radioactive surrogates (^{59}Co, ^{88}Sr, ^{130}Ba, and ^{193}Ir) with various concentrations and exploring other multivariate methods such as discriminant functional analysis (DFA), linear discriminant analysis (LDA), and artificial neural networks (ANNs).

4. It will be valuable to assess the leachability of cerium and cesium from RSC in different types of leachate solutions such as groundwater, rainwater, tap water, and sea water. Also, the effect of temperature on the leachability needs to be studied.

5. Many other tests could be used to characterize or evaluate RSC before and after adding radioactive materials such as partical size distribution, penetration resistance, tensile strength, and bending test.

6. Further work needs to be done on RSC properties without adding Ce or Cs. RSC samples could be placed in solution of DIW or ASW with Ce and Cs for 90 days as shown in figure 7.1. These samples will be cut in half and then composition analysis will be done by using

LIBS to see if the Ce and Cs have diffused inside the RSC samples. Fourthermore, mechanical and physical properties of RSC could be evaluated after 90 days.
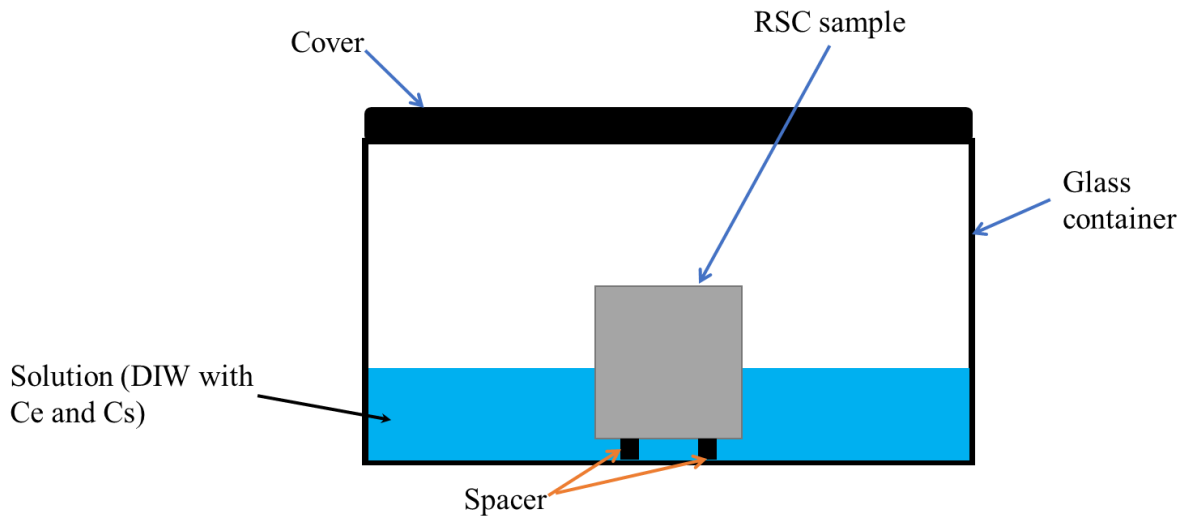
Figure 7. 1 The scheme of RSC sample soaked in solution of DIW with Ce and Cs.

- The X-ray diffraction patterns revealed two newly identified phases, namely $CeAl_{11}O_{18}$ and $Ce_{4.667}$ $(SiO_4)_3O$. Therefore, it is suggested to perform solubility limit of these compounds and obtain diffusion and kinetics studies on these compounds.
- pH values were significantly reduced with an increase of Ce content in both DIW and ASW. However, the pH values of RSC are still within the basicity range. Therefore, it is suggested that pH of RSC can be controlling by adding sodium hydroxide solution in order to keep it within the basicity range.

118

Chapter 8

References

1. H. M. Saleh, H.A. Shatta, "Immobilization of Simulated Borate Radioactive Waste Solution in Cement-Poly (Methylmethacrylate) Composite: Mechanical and Chemical Characterizations," *Journal of Nuclear Chemistry*, **2013**, (2013), Article ID 749505, http://dx.doi.org/10.1155/2013/749505.

2. R.J.M. Konings, T. Wiss, and O. Beneš, "Predicting Material Release During a Nuclear Reactor," *Nature Materials*, **14**, 247-252 (2015).

3. W.E. Lee, M. I Ojovan, and C. M Jantze (Eds.), *Radioactive Waste Management and Contaminated Site Clean-Up: Processes, Technologies and International Experience*, 1st ed., Woodhead, Cambridge (2013).

4. J. N. Meegoda, A. S. Ezeldin, H. Y. Fan, and H. I. Inyang, "Waste Immobilization Technologies," *Practice Periodical of Hazardous, Toxic, and Radioactive Waste Management*, **7**, 46-58 (2003).

5. M.I. Ojovan and W.E. Lee, *An Introduction to Nuclear Waste Immobilization*, 1st ed., Elsevier Science, Amsterdam, (2005).

6. R.D. Spence and C. Shi, (Eds.), *Stabilization and Solidification of Hazardous, Radioactive and Mixed Wastes*, 1st ed., Taylor and Francis Group, Florida, P.52 (2005).

7. Z. Drace and M.I. Ojovan, "The Behaviours of Cementitious Materials in Long Term Storage and Disposal: An Overview of Results of the IAEA Coordinated Research Programme," *Materials Research Society symposia proceedings*, **1193**, 663- 672 (2009).

8. M. L. Rouzic, T. Chaussadent, G. Platret, and L. Stefan, "Mechanisms of K-Struvite Formation in Magnesium Phosphate Cements," *Cement and Concrete Research*, **91**, 117-122 (2017).

9. L. J. Gardner, S. A. Bernal, S. A. Walling, C. L. Corkhill, J. L. Provis, and N. C. Hyatt, "Characterisation of Magnesium Potassium Phosphate Cements Blended with Fly Ash and Ground Granulated Blast Furnace Slag," *Cement and Concrete Research*, **74**, 78-87 (2015).

10. A.S. Wagh, *Chemically Bonded Phosphate Ceramics Twenty-First Century Materials with Diverse Applications*, 1st ed., Elsevier Science, New York (2004).

11. M. Anderson and M. Riley, "PaveMend[TM] as a Solution for Rapid Runway Repair," *Proceeding 27th International Air Transportation Conference 2002*, Orlando, Florida, June 30-July 3 (2002).

12. Q. Yang, B. Zhu, and X. Wu, "Characteristics and Durability Test of Magnesium Phosphate Cement-Based Material for Rapid Repair of Concrete," *Materials and Structures*, **33**, 229-234 (2000).

13. S.X. Li and M.F. Simpson, "Anodic process of electrorefining spent driver fuel in molten LiCl–KCl–UCl3/Cd system," *Mineral and Metallurgical Processing*, **22**, 192-198 (2005).

14. R.O.A. Rahman, R. Z. Rakhimov, N. R. Rakhimova, and M. I. Ojovan, *Cementitious Materials for Nuclear Waste Immobilization*, 1st ed., John Wiley and Sons, Ltd, Chichester (2014).

15. N. Mobasher, "Ba(OH)2-Na2SO4-BFS Cement Composites for the Encapsulation of Sulphate Bearing Nuclear Waste," Ph.D. Thesis, University of Sheffield, (2015).

16. A. Rahman, *Decommissioning and Radioactive Waste Management*, 1st ed., Taylor and Francis Group, New York and London (2008).

17. R.O.A. Rahman, H.A. Ibrahium, and Y.-T. Hung, "Liquid Radioactive Wastes Treatment: A Review," *Water*, **3**, 551-565 (2011).

18. International Atomic Energy Agency. Standardization of Radioactive Waste Categories; TRS No. 101; IAEA, Vienna, Austria, (1970).

19. International Atomic Energy Agency. Review of the Factors Affecting the Selection and Implementation of Waste Management Technologies; IAEA-TECDOC-1096, IAEA, Vienna, Austria, (1999).

20. J. Zheng, K. Tagami, Y. Watanabe, S. Uchida, T. Aono, N. Ishii, S. Yoshida, Y. Kubota, S. Fuma, and S. Ihara, "Isotopic Evidence of Plutonium Release into The Environment from the Fukushima DNPP Accident," *Scientific Reports*, **2**, (2012).

21. S. Uchida, M. Naitoh, H. Suzuki, H. Okada, and S. Konishi, "Evaluation of Accumulated Fission Products in the Contaminated Water at the Fukushima Daiichi Nuclear Power Plant," *Nuclear Technology*, **188**, 252-265 (2014).

22. T. Kobayashi, M. Ohshiro, K. Nakamoto, and S. Uchida, "Decontamination of Extra-Diluted Radioactive Cesium in Fukushima Water Using Zeolite–Polymer Composite Fibers," *Industrial & Engineering Chemistry Research*, **55**, 6996-7002 (2016).

23. International Atomic Energy Agency. Categorizing Operational Radioactive Wastes; IAEA TECDOC-1538, IAEA, Vienna, Austria, (2007).

24. T. Ohnishi, "The Disaster at Japan's Fukushima-Daiichi Nuclear Power Plant After the March 11, 2011 Earthquake and Tsunami, and the Resulting Spread of Radioisotope Contamination," *Radiation Research*, **177**, 1−14 (2012).

25. Computational Efficient Upscaling Methodology for Predicting Thermal Conductivity of Nuclear Waste forms, PNNL-20736, (2011).

26. International Atomic Energy Agency. The Behaviours of Cementitious Materials in Long Term Storage and Disposal: An Overview of Results of the IAEA Coordinated Research Project; IAEA-TECDOC series No. 1701, IAEA, Vienna, Austria, (2013).

27. International Atomic Energy Agency. Interim Storage of Radioactive Waste Packages; TRS No. 390, IAEA, Vienna, Austria, (1998).

28. J. H. Sharp, J. Hill, N. B. Milestone, and E. W. Miller, "Cementitious Systems for Encapsulation of Intermediate Level Waste," *9th ASME International Conference on Radioactive Waste Management and Environmental Remediation*, Oxford, England, Sept. 21–25 (2003).

29. J.M. Illston and P.L.J. Domone (Eds.), *Construction materials – their nature and behavior*, 3rd ed., Spon Press, London (2001).

30. W.S. Adaska, S.W. Tresouthick, P.B. West, *Solidification and Stabilization of Wastes Using Portland Cement Portland Cement Association*, 2nd ed., Portland Cement Association, Skokie (1998).

31. N. B. Singh, C. Shivani, and R. Sarita, "Chemistry of Portland Cement," J*ournal of the Indian Chemical Society*, **80**, 319-325 (2003).

32. H. F. W. Taylor, *Cement Chemistry*, 2nd ed., Thomas Telford, London (1997).

33. V.N. Dwivedi, S.S. Das, N.B. Singh, S. Rai, and N.S. Gajbhiye, "Portland Cement Hydration in the Presence of Admixtures: Black Gram Pulse and Superplasticizer," *Materials Research*, **11**, 427-431 (2008).

34. L. Black, C. Breen, J. Yarwood, C.-S. Deng, J. Phipps, and G. Maitland, "Hydration of Tricalcium Aluminate (C3A) in the Presence and Absence of Gypsum-Studied by Raman Spectroscopy and X-ray Diffraction," *Journal of Materials Chemistry*, **16**, 263-1272 (2006).

35. P.A. Bingham, R.J. Hand, M.C. Stennett, N.C. Hyatt, M.T. Harrison, "The Use of Surrogates in Waste Immobilization Studies: A Case Study of Plutonium," *Materials Research Society symposia proceedings*, **1107**, 421-428 (2008).

36. W. Gashier, "Accelerated Leaching Methods for Cementitious Nuclear Wasteforms and the Impact of Superplasticisers on the Leaching Behaviour," Ph.D. Thesis, University of Sheffield, (2016).

37. N. M. Sami, "Immobilization of Radioactive Waste in Different Fly Ash Zeolite Cement Blends" Ph.D. Thesis, Ain Shams University, (2013).

38. Y. K. Ibrahim, "Mechanical Properties of Concrete Incorporated BFS as Partial Replacement of Cement," *Diyala Journal of Engineering Sciences*, **09**, 28-38 (2016).

39. M. Balonis, "The Influence of Inorganic Chemical Accelerators and Corrosion Inhibitors on the Mineralogy of Hydrated Portland Cement Systems," Ph.D. Thesis, University of Aberdeen, (2010).

40. K.E. Kurtis, Y. Xi, M.A. Glinicki, J.L. Provis, E.R. Giannini, and T. Fu, "Can we design concrete to survive nuclear environments," *Concrete International*, **39**, 29-35 (2017).

41. H. -S. Kim, J. -W. Park, Y. -J. An, J. -S. Bae, and C. Han, "Activation of Ground Granulated Blast Furnace Slag Cement by Calcined Alunite," *Materials transactions*, **52**, 210-218 (2011).

42. L. Dodds, "Microstructure Characterisation of Ordinary Portland Cement Composites for the Immobilisation of Nuclear Waste Master," MPhil thesis, University of Manchester, (2012).

43. ASATM C 618-03, "Standard Specification for Coal Fly Ash and Raw or Calcined Natural Pozzolan for Use as a Mineral Admixture in Concrete," *Annual Book of ASTM Standards*, Vol. 04.01, American Society for Testing and Materials, Philadelphia, USA, (2003).

44. J. Hill and J. H. Sharp, "The Mineralogy and Microstructure of Three Composite Cements with High Replacement Levels," Cement and Concrete Composites, 24, 191-199 (2002).

45. C. V. McIsaac, "Leachability of Chelated ion-Exchange Resins Solidified in Cement or Cement and Fly Ash," *Waste Management*, **13**, 41-54 (1993).

46. D.A Cremers and L.J. Radziemski, *Handbook of Laser-Induced Breakdown Spectroscopy*, 1st ed., John Wiley & Sons Ltd., Chichester, West Sussex, England (2006).

47. A. Sarkar, R. K. Mishra, C. P. Kaushik, P. K. Wattal, D. Alamelu, and S. K. Aggarwal, "Analysis of Barium Borosilicate Glass Matrix for Uranium Determination by Using ns-IR-LIBS in air and Ar Atmosphere," *Radiochimica Acta*, **102**, 805-812 (2014).

48. F. Weritz, S. Ryahi, D. Schaurich, A. Taffe, and G. Wilsch, "Quantitative Determination of Sulfur Content in Concrete with Laser-Induced Breakdown Spectroscopy," *Spectrochimica Acta Part B: Atomic Spectroscopy*, **60**, 1121-1131 (2005).

49. M.Z. Martin, S. Allman, D.J. Brice, R.C. Martin, and N.O. Andre, "Exploring Laser-Induced Breakdown Spectroscopy for Nuclear Analysis and in-situ Applications," *Spectrochimica Acta Part B: Atomic Spectroscopy*, **74**, 177-183 (2012).

50. X. S. Wang, A. Li, N. Wazir, S. Q. Huang, S. Guo, L. Liang, M. Zhang, B. S. Zou, Y. Hao, F. He, Y. Bai, W. Sun, M. Hu, and R. Liu, "Accuracy Enhancement of Laser Induced Breakdown Spectra by Safely Low-Power Discharge," *Optics Express*, **26**, 13973–13984 (2018).

51. T. A. Labutin, A. M. Popov, S. N. Raikov, S. M. Zaytsev, N. A. Labutina, and N. B. Zorov, "Determination of Chlorine in Concrete by Laser-Induced Breakdown Spectroscopy in air," *Journal of Applied Spectroscopy*, **80**, 315-318 (2013).

52. M. A. Gondal, Z. H. Yamani, T. Hussain, and O. S.B. Al-Amoudi, "Determination of Chloride Content in Different Types of Cement Using Laser-Induced Breakdown Spectroscopy," *Spectroscopy Letters*, **42**, 171-177 (2009).

53. H. B. Zheng, F. Y. Yueh, T. Miller, J. P. Singh, K. E. Zeigler, and J. C. Marra, "Analysis of Plutonium Oxide Surrogate Residue Using Laser-Induced Breakdown Spectroscopy," *Spectrochimica Acta Part B: Atomic Spectroscopy*, **63**, 968–974 (2008).

54. E.C. Jung, D.H. Lee, J.-I. Yun, J.G. Kim, J.W. Yeon, and K. Song, "Quantitative Determination of Uranium and Europium in Glass Matrix by Laser-Induced Breakdown Spectroscopy," *Spectrochimica Acta Part B: Atomic Spectroscopy*, **66**, 761-764 (2011).

55. M. M. Tripathi, K. E. Eseller, F. -Yu. Yueh, and J. P. Singh, "Multivariate Calibration of Spectra Obtained by Laser Induced Breakdown Spectroscopy of Plutonium Oxide Surrogate Residues," *Spectrochimica Acta Part B: Atomic Spectroscopy*, **64**, 1212–1218 (2009).

56. Z. Laili, M. S. Yasir, and M. A. W. Yusof, "Leaching Behaviour of Cs-134 Immobilised in Cement-Biochar Matrix," *Jurnal Teknologi*, **78**, 59–67 (2016).

57. I. Plecas, "Leaching Study on the Process of Solidification of Radionuclide ^{60}Co in Concrete," *Polish Journal of Environmental Studies*, **14**, 699-701 (2005).

58. I. B. Plecas, R. S. Pavlovic, and S. D. Pavlovic, "Leaching of ^{60}Co and ^{137}Cs from Spent ion Exchange Resins in Cement–Bentonite Clay Matrix," *Bulletin of Materials Science*, **26**, 99–701(2003).

59. M.I. El-Dessouky, E.H. El-Masry, A.M. El-Kamash, and M.F. El-Shahat, "Leaching Study in Immobilization of Cesium and Cobalt Radionuclides in Fly Ash- Zeolite Cement," *Arab Journal of Nuclear Science and Applications*, **46**, 52 -62 (2013).

125

60. R.O. A. Rahman and A.A. Zaki, "Assessment of the Leaching Characteristics of Incineration Ashes in Cement Matrix," *Chemical Engineering Journal*, **155**, 698–708 (2009).

61. M. W. A. Raouf, A. I. Husain, and B. El-Gammal, "Immobilization of Radioactive and Hazardous Wastes in a Newly Developed Sulfur Polymer Cement (SPC) Matrix," *Proceedings of the 8. Arab International Conference on Polymer Science and Technology (ESPST)*, Sharm Elshiekh, Egypt, Nov. 27-30 (2005).

62. S.B. Eskander, S.M.A. Aziz, H. El-Didamony, and M. I. Sayed, "Immobilization of Low and Intermediate Level of Organic Radioactive Wastes in Cement Matrices," *Journal of Hazardous Materials*, **190**, 969-979 (2011).

63. Z.D. McClure and C. P. Cintron, "Processing and Characterization of Sol-Gel Cerium Oxide Microspheres," No. PNNL-25863, Pacific Northwest National Lab (2016).

64. J.E. Shoenberger, W. D. Hodo, C. A. Weiss, P. G. Malone, and T. S. Poole, "Expedient Repair Materials for Roadway Pavements," ERDC/GSL 05-07., Geotechnical and Structures Laboratory U.S. Army Engineer Research and Development Center (2005).

65. F. Millero, *Chemical Oceanography*, 4th ed., CRC Press Taylor & Francis Group, Boca Raton, New York (2013).

66. D.R. Kester, I. W. Duedall, D. N. Connors, and R. M. Pytkowicz, "Preparation of Artificial Seawater," *Limnology and oceanography*, **12**, 176-179 (1967).

67. L. J. Liu, J. -H. Li, X. Wang, T. -T. Qian, and X. -H. Li, "Tailoring the Strength and Porosity of Rapid-Hardening Magnesia Phosphate Paste via the Pre-Foaming Method," *Scientific Reports*, **5**, (2015).

68. F. Montes, S. Valavala, and L. Haselbach, "A New Test Method for Porosity Measurements of Portland Cement Pervious Concrete," *Journal of ASTM International*, **2**, 1-13 (2005).

69. J.A. Grubb, H. S. Limaye, and A. M. Kakade, "Testing pH of Concrete – Need for a Standard Procedure," *Concrete International*, **29**, 78-83 (2007).

70. D.V. Ribeiro and M.R. Morelli, "Influence of the Addition of Grinding Dust to a Magnesium Phosphate Cement Matrix," *Construction and Building Materials*, **23**, 3094-3102 (2009).

71. M.S.Sayed and N. Hafez, "Physico-Chemical Studies Involving Incorporation of Radioactive and Industrial Waste in Cement-Epoxy Resin Matrix," *International Conference on Hazardous Waste*, Cairo, Egypt, December 12-16 (1998).

72. J. Hu, Z. Ge, and K. Wang "Influence of Cement Fineness and Water-to-Cement Ratio on Mortar Early-age Heat of Hydration and Set Times," *Construction and Building Materials*, **50**, 657-663 (2014).

73. E.A. Kishar, D. A. Ahmed, M. R. Mohammed, and R. Noury, "Effect of Calcium Chloride on the Hydration Characteristics of Ground Clay Bricks Cement Pastes," *Beni-Suef University Journal of Basic and Applied Sciences*, **2**, 20-30 (2013).

74. A. -J. Wang, Z. -L. Yuan, J. Zhang, L. -T. Liu, J. -M. Li, Z. Liu, "Effect of Raw Material Ratios on the Compressive Strength of Magnesium Potassium Phosphate Chemically Bonded Ceramics," *Materials Science and Engineering: C*, **33**, 5058-5063 (2013).

75. A. Covill, N. C. Hyatt, J. Hill, and N. C. Collier, "Development of Magnesium Phosphate Cements for Encapsulation of Radioactive Waste," *Advances in Applied Ceramics*, **110**, 151-156 (2011).

76. C. McCague, L. Wang, and Y. Bai, "Magnesium Phosphate Cement as a Potential Alternative for Encapsulation of Nuclear Wastes Containing Aluminium," *Proceeding 31st Cement and Concrete Science Conference 2011*, London, UK, September 12-13 (2011).

77. T.C. Madhavi and S. Annamalai, "Electrical Conductivity of Concrete," *ARPN Journal of Engineering and Applied Sciences*, **11**, 5979-5982 (2006).

78. S. Awasthi, R. Kumar, A. Devanathan, R. Acharya, and A.K. Rai, "Multivariate Methods for Analysis of Environmental Reference Materials Using Laser-Induced Breakdown Spectroscopy," *Analytical Chemistry Research*, **12**, 10-16 (2017).

79. N.S. Rajurkar and M.M. Damame, "Elemental Analysis of Some Herbal Plants Using in the Treatment of Cardiovascular Diseases by NAA and AAS," *Journal of Radioanalytical and Nuclear Chemistry*, **219**, 77-80 (1997).

80. C.G. Ryan, "Quantitative Trace Element Imaging Using PIXE and the Nuclear Microscope," *International Journal of Imaging Systems and Technology*, **11**, 219-230 (2000).

81. J. Wang, T. Nakazato, K. Sakanishi, O. Yamada, H. Tao, and I. Saito, "Microwave Digestion with HNO3/H2O2 Mixture at High Temperatures for Determination of Trace Elements in Coal by ICP-OES and ICP-MS," *Analytica Chimica Acta*, **514**, 115-124 (2004).

82. N. Civici, S. Gjongecaj, F. Stamati, T. Dilo, E. Pavlidou, E.K. Polychroniadis, and Z. Smit, "Compositional Study of IIIrd Century BC Silver Coins from Kreshpan Hoard (Albania) Using EDXRF Spectrometry," *Nuclear Instruments and Methods in Physics Research Section B*, **258**, 414-420 (2007).

83. M. A. Tunes, C. G. Schon, and N. U. Wetter, "Viability Study of Using the Laser-Induced Breakdown Spectroscopy Technique for Radioactive Waste Detection at IPEN-CNEN/SP," *Proceeding 2013 International Nuclear Atlantic Conference – INAC 2013*, Recife, PE, Brazil, November 24-29 (2013).

84. S. Y. Oh, F. Y. Yueh, and J. P. Singh, "Laser-Induced Breakdown Spectroscopy: Application to Nuclear Waste Management – 9166," *Proceeding of the WM2009 conference*, Phoenix, Arizona, March 1-5 (2009).

85. A. Sarkar, R. K. Mishra, C. P. Kaushik, P. K. Wattal, D. Alamelu, and S K Aggarwal, "Analysis of Barium Borosilicate Glass Matrix for Uranium Determination by Using ns-IR-LIBS in air and Ar Atmosphere," *Radiochimica Acta*, **102**, 805-812 (2014).

86. Z. Wang, L. Li, L. West, Z. Li, and W. Ni, "A Spectrum Standardization for Laser-Induced Breakdown Spectroscopy Measurements," *Spectrochimica Acta Part B: Atomic Spectroscopy*, **68**, 58-64 (2011).

87. S. Awasthi, R. Kumar, A. Devanathan, R. Acharya, A. K. Rai, "Multivariate Methods for Analysis of Environmental Reference Materials Using Laser-Induced Breakdown Spectroscopy," *Analytical Chemistry Research*, **12**,10-16 (2017).

88. J. E. B. II, S. M. Clegg, D. K. Veirs, M. Browne, L. Lopez, and L. Le, "Application of Laser Induced Breakdown Spectroscopy (LIBS) Instrumentation for International Safeguards," *Proceeding of the INMM 51st Annual Meeting*, Baltimore, Maryland, July 10-15 (2010).

89. International Atomic Energy Agency. Safeguards Techniques and Equipment; 2011 Edition, International Nuclear Verification Series No.1 (Rev.2), IAEA, Vienna, Austria (2011).

90. P. R. Bevington and D. K. Robinson, Data Reduction and Error Analysis for the Physical Sciences, 3rd ed., McGraw-Hill, New York (2003).

91. A. N. Williams, "Measurement of Rare Earth and Uranium Elements Using Laser-induced Breakdown Spectroscopy (LIBS) in an Aerosol System for Nuclear Safeguards Applications," Ph.D. Thesis, Mechanical and Nuclear Engineering Department, Virginia Commonwealth University (2016).

92. W. Navidi, *Statistics for Engineers and Scientist*, 2nd ed., McGraw-Hill, New York (2008).

93. Q. Shi, G. Niu, Q. Lin, T. Xu, F. Li, and Y. Duan, "Quantitative Analysis of Sedimentary Rocks Using Laser-Induced Breakdown Spectroscopy: Comparison of Support Vector Regression and Partial Least Squares Regression Chemometric Methods," *Journal of Analytical Atomic Spectrometry*, **30**, 2384-2393 (2015).

94. A. Krishnan, L. J. Williams, A. R. McIntosh, and H. Abdi, "Partial Least Squares (PLS) Methods for Neuroimaging: A Tutorial and Review," *Neuroimage*, **56**, 455-475 (2011).

95. B. A. Varghese, "Analysis of Aggregate Mineralogy Using LIBS," Ph.D. Thesis, Rowan University, (2017).

96. A.A. Kabir, R.D. Merrill, A.A. Shamim, R. Klemm, A.B. Labrique, P. Christian, K.P. West Jr, and M. Nasser, "Partial Least Squares (PLS) Regression in Predicting Infant's Size at Birth in Rural North Western Bangladesh," *International Conference on Statistical Data Mining for Bioinformatics Health Agriculture and Environment*, Rajshahi, Bangladesh, December 21-24 (2012).

97. P. Geladi and B. R. Kowalski, "Partial Least-Squares Regression: A Tutorial," *Analytica Chimica Acta*, **185**, 1-17 (1986).

98. S. Wold, M. Sjostrom, and L. Eriksson, "PLS-Regression: A Basic Tool for Chemometrics," *Chemometrics and Intelligent Laboratory Systems*, **58**, 109-130 (2001).

99. O. Yeniay and A. Goktas, "A Comparison of Partial Least Squares Regression with Other Prediction Methods," *Hacettape Journal of Mathematics and Statistics*, **31**, 99-111 (2002).

100. B. Reisfeld and A. N. Mayeno (Eds.), *Computational Toxicology*, Volume II, Humana Press, SpringerScience + Business Media, New York (2013).

101. J. Yang, Z. Liu, B. Liu, and Q. Zhu, "Determination of Coptis Chinensis' Quality by FT-NIR Spectroscopy," *Health*, **4**, 196-202 (2012):

102. U. Panne, C. Haisch, M. Clara, and R. Neissner, "Analysis of Glass and Melts During the Vitrification Process of Fly and Bottom Ashes by Laser-Induced Plasma Spectroscopy. Part I: Normalization and Plasma Diagnostics," *Spectrochimica Acta Part B: Atomic Spectroscopy*, **53**, 1957-1968 (1998).

103. K. Song, Y. -I. Lee, and J. Sneddon, "Applications of Laser Induced Breakdown Spectroscopy," *Applied Spectroscopy Reviews*, **32**, 183-235 (1997).

104. R. S. Adrian and J. Watson, "Laser Microspectral Analysis: A Review of Principles and Applications," *Journal of Physics D: Applied Physics*, **17**, 1915-1940 (1984).

105. H. E. Bauer, F. Leis, K. Niemax, "Laser Induced Breakdown Spectrometry with an Echelle Spectrometer and Intensified Charge Coupled Device Detection," *Spectrochimica Acta Part B: Atomic Spectroscopy*, **53**, 1815-1825 (1998).

106. M. A. Gondal, T. Hussain, Z. H. Yamani, and M. A. Baig, "Detection of Heavy Metals in Arabian Crude oil Residue Using Laser Induced Breakdown Spectroscopy," *Talanta*, **69**, 1072-1078 (2006).

107. K. Loebe, A. Uhl, and H. Lucht, "Microanalysis of Tool Steel and Glass with Laser-Induced Breakdown Spectroscopy," *Applied Optics*, **42**, 6166-6173 (2003).

108. M. A. Gondal and T. Hussain, "Determination of Poisonous Metals in Waste Water Collected from Paint Manufacturing Plant Using Laser-Induced Breakdown Spectroscopy," *Talanta*, **71**, 73-80 (2007).

109. A.N. Williams, K. Bryce, and S. Phongikaroon, ''Measurement of Cerium and Gadolinium in Solid LiCl–KCl Salt Using Laser-Induced Breakdown Spectroscopy (LIBS),'' *Applied Spectroscopy*, **71**, 2302–2312 (2017).

110. American Nuclear Society. Measurement of the Leachability of Solidified Low-Level Radioactive Wastes by Short-Term Test Procedure; ANSI/ANS-16.1-2003. Illinois, USA, (2004).

111. P. Muthiah, K. S. Seshadri, P. K. Sinha, and K. B. Lal, "A Study on Leaching Behaviour of Cement Blocks used as Matrix for Fixation of Cs Activity Along with Ferric," *Bulletin of Materials Science*, **30**, 521-526 (2007).

112. G. B.-Nes, A. katz, Y. Peled, and Y. Zeiri, "The Mechanism of Cesium Immobilization in Densified Silica-Fume Blended Cement Pastes," *Cement and Concrete Research*, **38**, 667-674 (2008).

113. S. V. Mattigod, G. A. Whyatt, R. J. Seme, P. F. Martin, K. E. Schwab, and M. I. Wood. Diffusion and Leaching of Selected Radionuclides (Iodine- 129, Technetium-99, and Uranium) Through Category 3 Waste Encasement Concrete and Soil Fill Material; TRS No. PNNL-13639, Pacific Northwest National Laboratory, Richland, Washington, (2001).

114. S. V. Mattigod, M. Lindberg, J. Westsik Jr., K. Parker, and C. Chung. Waste Acceptance Testing of Secondary Waste Forms: Cast Stone, Ceramicrete and DuraLith; TRS No. PNNL-20632, Pacific Northwest National Laboratory, Richland, Washington, (2011).

115. NRC-U.S. Nuclear Regulatory Commission. Waste Form Technical Position; Revision 1, U.S. Nuclear Regulatory Commission, Washington, (1991).

116. A. Montaser, J. A. McLean, H. Liu, and J. -M. Mermet, *An Introduction to ICP Spectrometries for Elemental Analysis, in Inductively Coupled Plasma Mass Spectrometry*, ed. A. Montaser, Wiley, New York (1998).

117. K. Suzuki and Y. Ono, "Leaching Characteristics of Stabilized/Solidified Fly Ash Generated from Ash-Melting Plant," *Chemosphere*, **71**, 922–932 (2008).

118. T. Guo, P. S. Deshpande, and K. A. Rusch, "Identification of Dynamic Leaching Kinetics of Stabilized, Water-Soluble Wastes," *Environmental Science & Technology*, **38**, 603-608 (2004).

119. R.O. A. Rahman, and M. I. Ojovan, "Leaching Tests and Modelling of Cementitious Wasteforms Corrosion," *Innovations in Corrosion and Materials Science*, **4**, 90-95 (2014).

120. I. Plećaš, and S. Dimović, "Mathematical Modelling of Transport Phenomena in Concrete Matrix," *Physics, Chemistry and Technology*, **9**, 21-27 (2011).

121. M. I. El-Dessouky, E. H. El-Masry, A. M. El-Kamash, "Leaching and Mechanical Properties of Cement-Polyacrylamide Composite Developed as Matrices for Immobilization of Cs-137 and Co-60 Radionuclides," *Nature and Science*, **10**, 172-177 (2012).

122. K. -S. Bae and J. -O. Lee, "Immobilization of Ion-Exchnage Resins with a Mixture of Cement and WEP/Zeolan 900-Na Additives and Radionuclides Leaching," *Environmental Engineering Research*, **2**, 61-71 (1997).

123. S. G. Elizalde, M. S. Hernández, and A. M. G. Bustos, "Cemented Matrices Use in the Storage of Low and Medium Radioactive Waste: Spanish Experience," *1st Spanish National Conference on Advances in Materials Recycling and Eco – Energy Madrid*, Spain, November 12-13 (2009).

124. A. S. Wagh, S.Y. Sayenko, V.A. Shkuropatenko, R.V. Tarasov, M.P. Dykiy, Y.O. Svitlychniy, V.D. Virych, and E.A. Ulybkina, "Experimental Study on Cesium Immobilization in Struvite Structures," *Journal of hazardous materials*, **302**, 241-249 (2016).

125. J. M. Lee, J. Whang, C. L. Kim, and J. W. Park, "Leachability of Radionuclides from Cement-Solidified Waste form Produced at Korean Nuclear Power Plant," *Journal of Environmental Science and Health, Part A*, **37**, 201-212 (2002).

126. S. Goñi, A. Guerrero, and M. P. Lorenzo, "Efficiency of Fly Ash Belite Cement and Zeolite Matrices for Immobilizing Cesium," *Journal of hazardous materials*, **137**, 1608-1617 (2006).

Appendix I

MATLAB Code

I.1 Import files obtain from Aurora software as TXT files.

```
%% This code will read the raw data files obtain from Aurora spectrometer

% Created by Ammon Williams [91]

% Modified by Riyadh Motny

% Files format will be a TXT

% See uploaded file for details on LIBS run

% This code will Calculate mean for 100 shots and for 6 repetitions and then standard deviations

% Saves data in two matrices, lambda and spectra


close all; clear all;

%% Import data files

delimiterIn = '\t';

headerlinesIn = 10;

raw1 = importdata ('1 rep 1.txt', delimiterIn, headerlinesIn);

raw2 = importdata ('1 rep 2.txt', delimiterIn, headerlinesIn);

raw3 = importdata ('1 rep 3.txt', delimiterIn, headerlinesIn);

raw4 = importdata ('1 rep 4.txt', delimiterIn, headerlinesIn);

raw5 = importdata ('1 rep 5.txt', delimiterIn, headerlinesIn);
```

135

```matlab
raw6 = importdata ('1 rep 6.txt', delimiterIn, headerlinesIn);


%% Defining Variables

lambda1 = raw1.data (1: end, 1);

Spectra1 = raw1.data (1: end, 2: end);

Spectra2 = raw2.data (1: end, 2: end);

Spectra3 = raw3.data (1: end, 2: end);

Spectra4 = raw4.data (1: end, 2: end);

Spectra5 = raw5.data (1: end, 2: end);

Spectra6 = raw6.data (1: end, 2: end);

%% Calculate the mean spectra from the 100 shots

spectra2 (:, 1) = mean (Spectra1, 2);

spectra2 (:, 2) = mean (Spectra2, 2);

spectra2 (:, 3) = mean (Spectra3, 2);

spectra2 (:, 4) = mean (Spectra4, 2);

spectra2 (:, 5) = mean(Spectra5,2);

spectra2 (:, 6) = mean (Spectra6, 2);

%% Calculate the mean spectra from all the repetitions

meanspectra (:, 1) = mean (Spectra2, 2);

%% Calculate the standard deviation between the repetitions

stdev (:, 1) = std (Spectra2, 1, 2);

percentRSD (:, 1) = (stdev. / meanspectra)*100;

%% Plot
```

136

```matlab
figure (1);

hold on;

plot (lambda1, spectra2, 'b');

xlabel ('Wavelength (nm)');

ylabel ( 'Intensity' );

legend('Rep1', 'Rep2', 'Rep3', 'Rep4', 'Rep5', 'Rep6');

grid on;


figure (2);

hold on;

plot (lambda1, percentRSD, 'r');

xlabel ('Wavelength(nm)');

%% Saving the Data

save DISa1Su1 lambda1 spectra2
```

I.2 Analyze Spectral Data

```matlab
%% Loads spectral data

% Created by Ammon Williams [91]

% Modified by Riyadh Motny

% Normalizes each spectrum with respect to the mean of Si emission line.

% Calculates the mean of normalized spectra between repetitions.

% Calculates the standard deviation and percent relative standard deviation.

% Go to the GUI FindXPeak to find Xstart and Xfinal of points of peaks.
```

137

% Computes peak area, peak intensity, SBR and the SNR for the peak.

% Saves the data.

```matlab
close all; clear all;
%% loads files
load Data_Import_CDIWCe1


%% normalize data with respect to Si 518.2 nm line.


reps = 6; % repetitions


% Determines start and end points of Si peak
Xstart = size (lamba_1(lamba_1 < 517.8),1); % Si 517.8 nm
Xend = size (lamba_1(lamba_1 < 518.8),1); % Si 518.8 nm


%Find the mean
NormSpectra_1 = mean (spectra_1(Xstart:Xend,:));

NormSpectra_2 = mean (spectra_2(Xstart:Xend,:));

NormSpectra_3 = mean (spectra_3(Xstart:Xend,:));

NormSpectra_4 = mean (spectra_4(Xstart:Xend,:));

NormSpectra_5 = mean (spectra_5(Xstart:Xend,:));


%Normalizes the spectra with respect to Si 518.2 nm line.
```

```
for i = 1: reps

    Nspectra_1(:,i) = spectra_1(:,i)./NormSpectra_1(1,i);

    Nspectra_2(:,i) = spectra_2(:,i)./NormSpectra_2(1,i);

    Nspectra_3(:,i) = spectra_3(:,i)./NormSpectra_3(1,i);

    Nspectra_4(:,i) = spectra_4(:,i)./NormSpectra_4(1,i);

    Nspectra_5(:,i) = spectra_5(:,i)./NormSpectra_5(1,i);

end
```

%% Calculate the Normalized mean between repetitions and combine spectra in one matrix

Nmeanspectra(:,1) = mean(Nspectra_1,2);

Nmeanspectra(:,2) = mean(Nspectra_2,2);

Nmeanspectra(:,3) = mean(Nspectra_3,2);

Nmeanspectra(:,4) = mean(Nspectra_4,2);

Nmeanspectra(:,5) = mean(Nspectra_5,2);

%% Calculate the standard deviation and percent relative standard deviation (%RSD)

Nstdev(:,1) = std(Nspectra_1,1,2);

Nstdev(:,2) = std(Nspectra_2,1,2);

Nstdev(:,3) = std(Nspectra_3,1,2);

Nstdev(:,4) = std(Nspectra_4,1,2);

Nstdev(:,5) = std(Nspectra_5,1,2);

139

```matlab
NpercentRSD(:,1) = (Nstdev(:,1)./Nmeanspectra(:,1))*100;

%% look for area and intensity peak and find SBR and SNR for the peak.

line = 571.8;

[AreaAndStd(1,:), Peakpoints] = FindXPeak(lambda_1, Nspectra_1 , line, reps);

[AreaAndStd(2,:), Peakpoints] = FindXPeak(lambda_2, Nspectra_2 , line, reps);

[AreaAndStd(3,:), Peakpoints] = FindXPeak(lambda_3, Nspectra_3 , line, reps);

[AreaAndStd(4,:), Peakpoints] = FindXPeak(lambda_4, Nspectra_4 , line, reps);

[AreaAndStd(5,:), Peakpoints] = FindXPeak(lambda_5, Nspectra_5 , line, reps);

%% Plots

figure (1);

hold on;

plot (lamba_1, Nmeanspectra);

xlabel('Wavelength (nm)' );

ylabel('Intensity (a.u.)');

legend ('0.5 wt% Ce','1 wt% Ce','2 wt% Ce','4 wt% Ce','8 wt% Ce')

grid on;

figure (2)

hold on

plot (lamba_1, NpercentRSD,'b');

xlabel('Wavelength (nm)');

ylabel('%RSD');

grid on;

%% Saves the data
```

I.3 GUI Program

```
function [AreaAndStd, Xintensity, Peakpoints] =...

    PlotPeak(lambda, spectra , line, reps)

% This function uses a GUI to identify elements given characteristic wavelengths of an element

%   Created by Ammon Williams [91]

%   Modified by Riyadh Motny

%   lambda = array containing wavelength range of spectra

%   spectra = matrix containing spectra data

%   nm = array containing characteristic wavelengths of

%        a specific element

%   reps = number of repetitions or shots

%   func = 1 or 2; 1 just plots peaks & 2 performs peak analysis % Calculate the peak areas and

intensity for each repetition

 nX = size(lambda(lambda < nm),1);

 for i = 1:reps                              % Calculate area and intensity of the X Peak

  dX = 20;

  plot(lambda(nX-dX:nX+dX,1), spectra(nX-dX:nX+dX,i),'-or', ...

lambda(nX,1), spectra(nX,i),'xb');

xlabel('Wavelength');

ylabel('Counts');

wavlgt = num2str(nm);
```

141

```
shot = num2str(i);

legend(wavlgt,shot);

grid on

[j,k] = ginput(2);

Xstart(i,1) = size(lambda(lambda < j(1,1)),1);

Xend(i,1) = size(lambda(lambda < j(2,1)),1);

Xarea = trapz(lambda(Xstart(i,1):Xend(i,1),1),...

spectra(Xstart(i,1):Xend(i,1),i));

XPeakWidth = (lambda(Xend(i,1),1)-lambda(Xstart(i,1),1));

XPeakBackground = (spectraXstart(i,1),i)+spectra(Xend(i,1),i))/2;

Xbase = XPeakWidth*XPeakBackground;

correctedXarea(i,1) = (Xarea-Xbase);

Xintensity(i,1) = max(spectra(Xstart(i,1):Xend(i,1),i));

end

AreaAndStd(1,1) = mean(correctedXarea);

AreaAndStd(1,2) = std(correctedXarea,1);

AreaAndStd(1,3) = mean(Xintensity);

AreaAndStd(1,4) = std(Xintensity,1);

Peakpoints(:,1) = Xstart;

Peakpoints(:,2) = Xend;

close all

end
```

I.4 Univariate method (Calibration Curves)

% This code is to carry out the Calibration Curve.

%   Created by Ammon Williams [91]

%   Modified by Riyadh Motny

%   loads data from previous code (Analyze Spectral Data)

% Calculates the mean, the slope (m), the y-intercept (b),and correlation coefficient (R^2) of the

line.

close all; clear all

%% Load Data

load Ce_Concentration

load Data_Values

x = wtCe; % Ce concentration from XRF

yI = AreaAndStd(:,3); % Peak intensity

AreaStdI = AreaAndStd(:,4); % std of Peak intensity

%% Calculate the regression line and the confidence and prediction intervals

x1 = x (1:5,1);

y1 = yI (1:5,1);

AreaStd1 = AreaStdI (1:5,1);

xbar = mean(x1); % mean of Ce concentrations

ybar = mean(y1); % mean of peak intensity data

SSx = sum((x1-xbar).^2);

143

```matlab
SSy = sum((y1-ybar).^2);

Sxybar = sum((x1-xbar).*(y1-ybar));

m = Sxybar/SSx; % slope of regression line

b = ybar-m1*xbar; % y-intercept of regression line

yhat = m*x1+b;

R = Sxybar/sqrt(SSx*SSy);

R2 = R^2;  % correlation coefficient

LOD = (3*AreaStd1(1,1))/m; % limit of detection

n = size(y1,1); % number of data points

Syx = sqrt((sum((y1-yhat).^2))/(n-2));

t = tinv(1-.05/2,n-2); %  students t value

for i = 1:n

    % Lower confidence interval

    CIlow(i,1) = yhat(i,1)-t*Syx*sqrt(1/n+(x1(i,1)-xbar)^2/SSx);

    % upper confidence interval

    CIhigh(i,1) = yhat(i,1)+t*Syx*sqrt(1/n+(x1(i,1)xbar)^2/SSx);


end

%% organize variables

% Peak Intensity

RegressionData(1,1) = m;

RegressionData(2,1) = b;

RegressionData(3,1) = R2;
```

144

```matlab
RegressionData(4,1) = LOD;


%% Plot

figure(1);

hold on;

errorbar(x1, y1, AreaStd1,'ro');

hold on

plot(x1,yhat,'b',x1,CIlow,'b-.',x1,CIhigh,'b-.');

axis([0 8 0 inf])

legend('Data','data','Regression fit','Confidence interval');

legend boxoff

xlabel('Concentration (wt% Ce)');

ylabel('Intensity');
```

I.5 Principal component analysis (PCA)

```matlab
% This code is to perform PCA.

% Created by Riyadh Motny

% loads data from previous code (Import files)

clear all

close all

set(0,'defaultAxesFontName', 'Times new Roman')

set(0,'defaultTextFontName', 'Times new Roman')

set(0,'defaultAxesFontSize', 16)
```

145

```matlab
set(0,'defaultTextFontSize', 16)

load Data_Values

load Ce_Concentration

X = spectra2;

Y = wtCe;

XX=X';

[n, m]=size(XX);



%-------------------------------------------------

% Calculate the mean and center the data

for i=1:m

    I_final_m(i)=sum(XX(:,i))/n;

end

for i=1:m

    I_final_adj(:,i)= XX(:,i)-I_final_m(i);

end

% Calculate the covariance and the eigenvalues

for i=1:m

    for j=1:m


        sum_ij=0;

        for R=1:n

            sum_ij=sum_ij+I_final_adj(R,i)*I_final_adj(R,j);
```

146

```matlab
        end


    con_AA(i,j)=sum_ij/(n-1);

  end

end


[v_AA e_AA]=eig(con_AA);

D=diag(e_AA);




sum_D=0;

for i=1:m

  sum_D=sum_D+e_AA(i,i);

  Lamda(i)=e_AA(i,i);

end

DD = (Lamda/sum_D);




SS=DD*10^2;



%-----------------------------------------------------------

%change the order of the eigenvalues from biggest to smallest

YY = sort(SS, 'descend');
```

147

```matlab
%-----------------------------------------------------------
 % Deriving the new data set
Data_AA_final=I_final_adj *v_AA;
%-----------------------------------------------------------
%%% Plots
figure(1)
hold on
gscatter(Data_AA_final(:,m),Data_AA_final(:,m-1));
%grid on
axis([-0.02 0.04  -0.01 0.01]);
set(gca,'XMinorTick','on','YMinorTick','on')
xlabel('PC1')
ylabel('PC2')
figure(2)
UU=[0;1;2;3;4;5;6;7;8;9];
plot(UU,100-YY(1:10),'r');
grid on
xlabel('Number of components')
ylabel('Eigenvalues')
title('scree Plot (0.5,1, 2, 4, 8) wt% Ce)')
```

I.6 Partial least squares (PLS)

```matlab
% This code is to perform PLS.

% Created by Riyadh Motny

% loads data from previous code (Import files)

clear all

close all

set(0,'defaultAxesFontName', 'Times new Roman')

set(0,'defaultTextFontName', 'Times new Roman')

set(0,'defaultAxesFontSize', 16)

set(0,'defaultTextFontSize', 16)



load Data_Values

load Ce_Concentration



X = spectra2;

Y = wtCe;



XX=X';

[n, m]=size(XX);



%----------------------------------------------------

% Calculate the B, matrix (n,k), a set of regression coefficients for each response.
```

```matlab
for h =1:18

[Xloadings,yloadings,Xscores,Yscores,betaPLS,PCTVAR] = plsregress(XX,Y,h); %Perform

PLS regression with eighteen components.

yfit_cal= [ones(size(XX,1),1) XX]*betaPLS;

N = size(Y,1);

RMSEc = sqrt((sum((yfit_cal-Y).^2))/(N));

RMSECT(h,:)= RMSEc;

end

 % Build the PLS model with seven components.

[Xloadings,yloadings,Xscores,Yscores,betaPLS,PCTVAR] = plsregress(XX,Y,7); %Perform

PLS regression again with best component numbers.


yfit_cal= [ones(size(XX,1),1) XX]*betaPLS;

N = size(Y,1);

RMSEC = sqrt((sum((yfit_cal-Y).^2))/(N));

%% Fit value by leave one sample out

for i=1:20

  x_test = XX(i,:);

  y_test = Y(i,:);

  if i==1

    x_train = XX(i+1:end,:);

    y_train = Y(i+1:end,:);

  else
```

150

```matlab
    x_train = [XX(1:i-1,:);XX(i+1:end,:)];

    y_train = [Y(1:i-1,:);Y(i+1:end,:)];


    end

    for h=1:18

[Xloadings,yloadings,Xscores,Yscores,betaPLS,PCTVAR] = plsregress(x_train,y_train,h);


yfit= [ones(size(x_test,1),1) x_test]*betaPLS;

Yfit(:,h)= yfit;

    end


B(:,i) = betaPLS;

YYfit(i,:) = Yfit;

end


%% Calculate root mean square error validation (RMSECV)

RMSECV = sqrt((sum((YYfit(:,7)-Y).^2))/(N));


for i=1:18

  RMSECVT(i,:) = sqrt((sum((YYfit(:,i)-Y).^2))/(N));

end


%% Plots
```

```matlab
figure(1)

%Plot the percent of variance explained in the response variable as a function of the number of
components.

plot(0:17,cumsum(100*PCTVAR(1,:)),'-bo');

axis([0 8 0 100])

xlabel('Number of components');

ylabel('Variance Explained (%)');


figure(2);

hold on;

plot(Y,yfit_cal,'bo');

xlabel('XRF Ce concentration (wt%))');

ylabel('Predicted Ce concentration (wt%)');

legend('Calibration Data','Location','NorthWest');

legend boxoff

set(gca,'XMinorTick','on','YMinorTick','on','fontsize',12)

figure(3);

subplot(1,2,1);

hold on;

plot(1:h,RMSECT,'-bx');

plot(1:h,RMSECVT,'-rx');

xlabel('latent variable number');

ylabel('RMSEC,RMSECV');
```

```matlab
legend('RMSEC','RMSECV','Location','northeast');

axis('square');

title('(a)');

set(get(gca,'title'),'Position',[-3 2.45]);

set(gca,'XMinorTick','on','YMinorTick','on','fontsize',8)


subplot(1,2,2);

hold on;

plot(Y,yfit_cal,'bo');

plot(Y,YYfit(:,7),'ro');

plot([0;9;],[0;9;],'k')

box on

axis([0 9 -0.5 inf])

axis('square');

xlabel('XRF Ce concentration (wt%)');

ylabel('Predicted Ce concentration (wt%)');

legend('Calibration Data','Validation Data','1:1','Location','NorthWest');

title('(b)');

set(get(gca,'title'),'Position',[-1 8.8]);

set(gca,'XMinorTick','on','YMinorTick','on','fontsize',8)

print('PLS_Ce_DIW', '-dtiff', '-r300');
```

153